

BRL CR 346

# BRL

12

AD

AD A 044998

CONTRACT REPORT NO. 346

TRANSIENT COMBUSTION IN GRANULAR  
PROPELLANT BEDS. PART I: THEORETICAL  
MODELING AND NUMERICAL SOLUTION OF  
TRANSIENT COMBUSTION PROCESSES IN  
MOBILE GRANULAR PROPELLANT BEDS

Prepared by

The Pennsylvania State University  
Department of Mechanical Engineering  
University Park, PA 16802

DDC  
FORM 1  
OCT 11 1977  
C

August 1977

Approved for public release; distribution unlimited.

USA ARMAMENT RESEARCH AND DEVELOPMENT COMMAND  
USA BALLISTIC RESEARCH LABORATORY  
FORT MONMOUTH, NEW JERSEY

AD No. 1  
DDC FILE COPY

✓

Destroy this report when it is no longer needed.  
Do not return it to the originator.

Secondary distribution of this report by originating  
or sponsoring activity is prohibited.

Additional copies of this report may be obtained  
from the National Technical Information Service,  
U.S. Department of Commerce, Springfield, Virginia  
22151.

The findings in this report are not to be construed as  
an official Department of the Army position, which  
is designated by other authorized documents.

Do not disseminate information of this report  
to unauthorized personnel.

SECURITY CLASSIFICATION OF THIS PAGE (When Data Entered)

REPORT DOCUMENTATION PAGE		READ INSTRUCTIONS BEFORE COMPLETING FORM
1. REPORT NUMBER BRL CONTRACT REPORT NO. 346	2. GOVT ACCESSION NO.	3. RECIPIENT'S CATALOG NUMBER
4. TITLE (and Subtitle) <b>Transient Combustion in Granular Propellant Beds. Part I: Theoretical Modeling and Numerical Solution of Transient Combustion Processes in Mobile Granular Propellant Beds.</b>		5. TYPE OF REPORT & PERIOD COVERED Final Report Feb. 15, 1974 - Feb. 14, 1977
7. AUTHOR(s) J. H. /Koo and K. K. /Kuo		6. PERFORMING ORG. REPORT NUMBER
8. PERFORMING ORGANIZATION NAME AND ADDRESS Department of Mechanical Engineering The Pennsylvania State University University Park, PA 16802		9. CONTRACT OR GRANT NUMBER(s) DAAG 29-74-G-0116
11. CONTROLLING OFFICE NAME AND ADDRESS U. S. Army Research Office Post Office Box 12211 Research Triangle Park, NC 27709		10. PROGRAM ELEMENT, PROJECT, TASK AREA & WORK UNIT NUMBERS
14. MONITORING AGENCY NAME & ADDRESS (if different from Controlling Office) 1. Combustion and Prop. Br. 2. Ballistics and Comb. Ballistic Research Lab. Research Branch Aberdeen Proving Ground Picatinny Arsenal Aberdeen, MD 21005 Dover, NJ 07801		12. SUBJECT DATE AUGUST 1977
16. DISTRIBUTION STATEMENT (of this report) Approved for public release; distribution unlimited.		13. NUMBER OF PAGES 182
17. DISTRIBUTION STATEMENT (of the abstract entered in Block 20, if different from Report) Final rept. 15 Feb 74 - 14 Feb 77,		15. SECURITY CLASS. (of this report) Unclassified
18. SUPPLEMENTARY NOTES		16. SECURITY CLASSIFICATION/DOWNGRADING SCHEDULE NA
19. KEY WORDS (Continue on reverse side if necessary and identify by block number) Two-Phase Reacting Flow      Mobile Bed of Gun Powders Granular Propellants      Gas Penetration Modeling of Small Arms      Acceleration Flame Gun Interior Ballistics      Transient Combustion Flame Spreading		
20. ABSTRACT (Continue on reverse side if necessary and identify by block number) Gas-permeable propellants possess great potential for producing sizable thrusts within extremely short time intervals. A research program was set up with the objectives: (1) to obtain a deeper understanding of high speed flame propagation and the gas dynamic behavior of two-phase reactive flow systems; and (2) to predict the rates of gasification during transient heterogeneous combustion of granular propellant beds.		

FORM 1 JAN 73 1473

VERSION OF 1 NOV 68 IS OBSOLETE

Unclassified

SECURITY CLASSIFICATION OF THIS PAGE (When Data Entered)

401929

LB

20. The following transient phenomena occur in a few milliseconds: penetration of hot gases into interstitial voids, convective heating of pellets to ignition, granular bed compaction and rapid pressurization in a thick-walled, steel chamber. Pressure transients and flame-front speeds are measured by high-frequency pressure transducers and ionization probes, respectively. A gaseous pyrogen ignition system utilizing a spark ignition was found most suitable for varying igniter strengths and achieving high reproducibility.

The physio-chemical phenomena described above have been formulated into a theoretical model. The method employed in this study is the gas dynamic approach which is developed by formulating the governing equations on the basis that mass, momentum and energy fluxes are balanced over control volumes occupied separately by the gas and particle-phases. The governing equations were derived in the form of coupled, non-linear, inhomogeneous partial differential equations. This system of equations is solved together with some empirical input such as heat transfer, flow resistance, intergranular stress and the burning rate law. They are found to be of hyperbolic type, since all the eigenvalues are real. The compatibility relations are used as extraneous boundary conditions together with some physical boundary conditions to solve the boundary points. A stable, fast convergent, explicit numerical scheme incorporated with predictor and corrector are used in the interior, and the method of characteristics is used on the boundaries.

The results show that the flame front accelerates significantly and the rate of pressurization increases substantially in the downstream direction. The igniter strength and the propellant gasification temperature were found to have pronounced effects on the pressurization process. The theoretical predictions are in close agreement with the experimental data.

ACCESSION for	
W. S.	Write Section <input checked="" type="checkbox"/>
W. H.	B. H. Section <input type="checkbox"/>
W. C. D.	<input type="checkbox"/>
SECTION	
RY	
DISTRIBUTION/AVAILABILITY CODES	
11	11/12 SPECIAL
A	

## TABLE OF CONTENTS

	<u>Page</u>
LIST OF FIGURES. . . . .	5
LIST OF TABLES . . . . .	7
I. INTRODUCTION . . . . .	9
1.1 Motivation and Objective. . . . .	9
1.2 Pioneering Work . . . . .	12
1.3 Basic Approach. . . . .	15
II. LITERATURE SURVEY. . . . .	19
2.1 Survey on Related Works . . . . .	19
2.2 Survey of Empirical Correlations and Their Limitations . . . . .	24
2.3 Survey on Numerical Studies . . . . .	26
III. THEORETICAL FORMULATION AND ANALYSIS OF TRANSIENT COMBUSTION PROCESSES IN GRANULAR BEDS. . . . .	28
3.1 Description of Physical Processes . . . . .	29
3.2 Basic Assumptions . . . . .	31
3.3 Theoretical Model . . . . .	32
3.4 Simplifications . . . . .	41
3.5 Governing Equations in the Left Control Volume. . . . .	43
3.6 Eigenvalue Determination of the System. . . . .	50
3.7 Initial and Boundary Conditions . . . . .	55
3.8 Empirical Correlations. . . . .	58
3.9 Ignition Criterion. . . . .	65
IV. NUMERICAL SOLUTION TECHNIQUE . . . . .	66
4.1 Selection of Numerical Methods. . . . .	67
4.2 The Finite-Difference Equations for the Interior Points . . . . .	70
4.3 Numerical Treatment of the Boundary Conditions. . . . .	74
4.4 Convergence Tests and Error Analysis. . . . .	86
4.5 Stability Criteria. . . . .	87
4.6 Artificial Viscosity. . . . .	90
4.7 Calculation Procedure and Flexibility of the Program . . . . .	91

TABLE OF CONTENTS

	<u>Page</u>
V. COMPARISON OF THEORETICAL PREDICTIONS WITH EXPERIMENTAL DATA. . . . .	94
5.1 Experimental Setup. . . . .	94
5.2 Discussion of Results . . . . .	101
VI. CONCLUSIONS. . . . .	119
VII. ACKNOWLEDGMENT . . . . .	121
REFERENCES . . . . .	122
APPENDIX 1: Conservation Equations in the Eulerian Form . . . . .	129
APPENDIX 2: Analytical Solution of the Solid- Phase Heat Equation . . . . .	131
APPENDIX 3: Characteristic Equation for the System. . . . .	139
APPENDIX 4: Determination of Eigenvalues for the Governing Equations . . . . .	157
APPENDIX 5: Finite-Difference Equation for the Gas Mass Equation . . . . .	161
APPENDIX 6: The Relationships of Intergranular Stress and the Speed of Sound in Granular Beds . . . . .	163
APPENDIX 7: Characteristics Considered for Various Cases at the Left Boundary. . . . .	167
NOMENCLATURE . . . . .	171
DISTRIBUTION LIST. . . . .	177

## LIST OF FIGURES

<u>Figure Number</u>		<u>Page</u>
1	Schematic Drawing of the Ignition and Combustion Chamber . . . . .	30
2	Control Volumes Considered in the Analysis . . . . .	33
3	Control Volume Considered in the Left Boundary . . . . .	44
4	Characteristic Directions at the Two Boundaries of the Granular Bed when the Gas at $x_1$ Flows from the Entrance Region into the Propellant Bed . . . . .	75
5	Characteristic Directions at the Two Boundaries of the Granular Bed when the Gas at $x_1$ Flows from the Propellant Bed into the Entrance Region . . . . .	75
6	Flow Chart for Left Boundary Condition - Case 1 . . . . .	80
6A	Flow Chart for Right Boundary Condition . . . . .	83
7	Flow Chart for Left Boundary Condition - Case 5 . . . . .	85
8	General Flow Chart for the Solution of Governing Equations . . . . .	92
9	Schematic Drawing of Igniter Feed Line and Ignition Chamber . . . . .	96
10	Specified Igniter Mass Flow Rate Flowing into the Granular Bed as a Function of Time . . . . .	98
11	Schematic Drawing of the Multi-Perforated Convergent Nozzle . . . . .	99
12	Predicted Pressure-Time Traces for G2, G3, G4 and G5 . . . . .	102
13	Measured Pressure-Time Traces from a Typical Firing (Traces are Offset Vertically for Clarity) . . . . .	103

<u>Figure Number</u>		<u>Page</u>
14	Comparison of Theoretically Predicted G2 Pressure Trace with the Composite Pressure Traces of Six Experimental Firings . . . . .	105
15	Comparison of Theoretically Predicted G3 Pressure Trace with the Composite Pressure Traces of Six Experimental Firings . . . . .	106
16	Comparison of Theoretically Predicted G4 Pressure Trace with the Composite Pressure Traces of Six Experimental Firings . . . . .	107
17	Comparison of Theoretically Predicted G5 Pressure Trace With the Composite Pressure Traces of Six Experimental Firings . . . . .	108
18	Comparison of Theoretically Predicted Flame Front Position with Experimental Data . . . . .	110
19	Calculated Pressure Distributions at Various Times . . . . .	111
20	Calculated Gas Temperature Distributions at Various Times . . . . .	112
21	Calculated Particle Temperature Distributions at Various Times . . . . .	114
22	Calculated Gas Velocity Distributions at Various Times . . . . .	115
23	Calculated Particle Velocity Distributions at Various Times . . . . .	116
24	Calculated Porosity Distributions at Various Times . . . . .	117
25	Subsurface Temperature Distribution Inside a Solid Propellant Grain . . . . .	133
26	The Dependence of Speed of Sound in the Solid Propellant Aggregate . . . . .	164
27	Dependence of Particulate Stress Tensor upon Porosity of the Mixture . . . . .	164

LIST OF TABLES

<u>Table Number</u>		<u>Page</u>
1	Data Used in the Numerical Computations . . . . .	63
2	Physical, Compositional and Thermo-Chemical Data of WC 870 Propellant . . . . .	95

CHAPTER I  
INTRODUCTION

The motivation and the overall objective for the present investigation is first defined. Having provided the motivation and objective for this, some useful applications are given in regard to this study. We then provide some background information related to pioneering work in the early stage of interior ballistic modeling. Reference is made to some of the related work in this area. This chapter is concluded by a brief discussion of the basic approach taken for different models associated with flame spreading and granular propellant burning. The main purpose of this discussion is to point out the fundamental differences in the method of approach for all models.

1.1 Motivation and Objective

This research is stimulated by the potential of gas-permeable<sup>\*</sup> propellants for achieving high gasification rates and producing high thrusts during extremely short time intervals. The research is also partially motivated by the recent progress in the area of granular propellant studies (1, 2, 3, 4, 5). Besides the encouragement offered by these advancements in this field, the problem of flame spreading in porous propellant charges is obviously important in the design and analysis of propulsion systems.

The overall research motivation and objectives are:

- 1) Anomalous burning behavior has been observed in combustion of granular solid propellants. A better understanding of the

---

<sup>\*</sup>The word "gas-permeable propellant" or "porous propellant" used in this study designates either a packed bed of granular pellets with or without perforation, or a cast monolithic propellant with pores.

transient combustion phenomena is required to reduce hazards and to improve the design of propulsion systems.

- 2) To advance the state-of-the-art in the combustion of granular propellents by formulating a complete theoretical model describing the important physical phenomena involved in both gaseous and solid phases.
- 3) To solve the theoretical model by selecting a stable, fast convergent numerical scheme so that effects of a) igniter strength b) propellant physio-chemical characteristic and c) propellant loading density can be studied.
- 4) To conduct experimental firings in a thick-walled combustor with a fixed boundary, to measure the pressure-time transients at various axial locations and flame propagation rates so that the theoretical model developed in this study can be verified.

The results obtained from this study are directly useful for more accurate predictions of the interior ballistics of artillery systems. The research is also pertinent to the future development of end-burning porous propellant charges to be used in a more predictable and controllable manner for rocket or missile propulsion. In addition, the techniques developed in this investigation can lead toward both a better understanding of porous-propellant combustion and the earlier behavior of the overall deflagration-to-detonation transition (DDT).

The phenomena that occur during the transient event include the following:

- a) the penetration of hot product gases into the granular bed
- b) convective heating of propellant to ignition
- c) compaction of the granular bed

- d) generation of peak pressure within the chamber
- e) propagation of the peak pressure to the shear disc end  
of the granular bed
- f) flame front acceleration
- g) rupture of shear disc which initially seals the combustion
- h) the depressurization processes after the burst of the  
shear disc

### 1.2 Pioneering Work

The theoretical formulation of granular propellant combustion for interior ballistic calculations can be categorized into three separate stages: 1) lumped parameter analysis; 2) theoretical modeling for earlier behavior of the ignition and flame spreading processes by assuming that the granular propellents are fixed in space; and 3) modeling of mobile granular beds so that the overall transient processes in ballistic cycle study can be achieved.

Baer and Frankle (6) were the pioneers to use the lumped parameter method to develop an interior ballistic model. Their model is governed by five simplified equations. Due to the uncertainties of the burning rate law, this model's predictive capability is limited. This is further improved by introducing ballistic fitting into the burning rate. Some other lumped parameter analyses are contained in Corner's (7) text including the classical work of Lagrange, Love, Pidduck and Kent on hydrodynamic theories of interior ballistics.

It was not until recently that Kuo, Vichnevetsky & Summerfield (1, 8) have developed a fixed-bed theoretical model (referred as KVS model in ballistics) to describe flame propagation in a packed bed of granular propellents. The calculated pressure-time-distance transients, wave propagation speed, and mass fraction of propellant burned during flame spreading, all agree well with the experimental data obtained by Squire and Devine (9) in a venting bomb experiment. Soper (10) conducted experimental firings in some artillery systems. He utilized translucent cartridge cases together with flash X-ray and photographic techniques to determine the relative positions of the ignition front to the pressure wave front in the packed bed of NACO propellents. He claims that his

experimental data also agrees well with the theoretical conclusion made by the KVS model (1, 8) i.e., the ignition front lies near the leading edge of the pressure wave. Kuo et al (1, 8) used an implicit finite difference scheme to obtain the numerical solutions and were also checked by Kitchens (11) using the method of characteristics.

The KVS model and its numerical solutions (1, 8) based upon the fixed bed assumption for a packed bed of granular propellants, has stimulated the interest of other investigators in pursuing studies in both theoretical and experimental directions. Governing equations similar to the KVS model equations have been further developed by several investigators, to include the motion of solid propellant grains. The models are developed by Fisher and Graves (2), Gough and Zwarts(3), East and McClure (4), Krier, Van Tassell, Rajan and VerShaw (5), Gough(12), and Kuo and Summerfield (36)(Some discussions on each model are shown in section 2.1).

In the formulation of boundary conditions for a transient combustion study, except KVS model (8) and Gough's work (12), none of the previous investigators have used the compatibility relations for the solution of boundary conditions. The treatment of boundary conditions are usually not satisfactory. Due to the complication of the theoretical modeling and difficulties in experimentation, no investigators have verified their models by performing their own experiments to match with the same conditions for the models.

In the present investigation, experimental firings are done to verify our theoretical model. The governing equations are derived using the principles of gas dynamics. The nature of the system of governing equations are determined to be of hyperbolic type. The compatibility relations are deduced to supplement the physical boundary conditions to solve the boundary

points. A combination of explicit finite difference scheme and the method of characteristics is employed for the numerical solutions. The predictions made by the present model are found to have good agreement with our experimental data.

### 1.3 Basic Approach

Due to the complexity in describing the physical processes for this two-phase combustion problem, several different approaches have been proposed. The theoretical methods can be classified into four categories:

- A. statistical model;
- B. continuum mechanics models;
- C. formal averaging models; and
- D. two-phase fluid dynamic models

The method employed in this study is the two-phase fluid dynamic model which is developed by formulating the governing equations on the basis that mass, momentum and energy fluxes are balanced over control volumes occupied separately by the gas- and particle-phases.

Up to now, statistical methods have not been applied to this particular combustion problem due to their inconvenience in obtaining useful results and also due to the lack of reliable statistical information for describing some of the important terms in the model. Only a few applications of these methods are found with application to the governing equations of chemically non-reacting two-phase flow system. Some statistical methods are included in the text by Beran (13). Among all the investigators, such as Aronow (14), Law and Fung (15), Cox and Brenner (16), the most comprehensive works are those done by Buyevich (17, 18, 19). The main difficulty of this approach lies in the description and definition of the mean properties of a two-phase motion and also in the evaluation of the net effect of microscopic behavior. Because of these difficulties involved, the statistical approach is not followed in the present investigation.

In the continuum mechanics methods, the gas and solid media are considered as separate continua that interact with each other based on the

continuum mechanics principles. The basic theory was laid down by Truesdell and Toupin (20). Most analysis in these methods start with the conservation laws. Since continuum mechanics does not seek to reconcile the properties of matter with the structure of the constituents, therefore, this theory has been applied both for homogeneous fluids and heterogeneous mixtures.

Earlier studies by Green and Naghdi (21, 22), Eringen and Ingram, (23) and others were criticized by Truesdell (24). Müller (25) and Dorcia (26) have investigated the constitutive laws for mixture of two fluids. None of the previous investigators have made an attempt to construct a theory with immediate application to the two-phase reacting flow combustion problem. Recently, Krier et al (5) based on the continuum mechanics concepts, formulated equations for a model that associated with flame spreading and combustion in porous propellant beds. The weakness of the model developed by Krier et al is discussed in section 2.1.

The formal averaging methods assume that the flow behavior of the microscopic aspects is determined and seek for the macroscopic aspects of the flow. The formulations are derived by averaging the flow properties over regions large compared with the size of propellant grains, but small when compared with the macroscopic scale of the experiments. Among those investigators who applied these methods, the better known works are those by Slattery (27, 28), Anderson and Jackson (29), Whitaker (30), and Panton (31). Recently, Gough (12), based on the works by Anderson and Jackson (29), Whitaker (30), and Panton (31) developed a theoretical model to solve the flow of a compressible gas through an aggregate of mobile reacting particles. The differences in derivation of conservation equations between our approach and the formal averaging approaches are analogous to the differences

between the Boltzmann's Molecular derivation (32) and the conventional continuum derivation of conservation equations in fluid mechanics. The difference between these two approaches are discussed in more detail in Chapter II.

Finally, the two-phase fluid dynamic methods are considered by formulating the governing equations on the basis that mass, momentum and energy fluxes are balanced over control volumes occupied separately by the gas- and particle-phases. Among the previous investigators, Murray (33), Kraiko and Sternin (34), Nigmatulin (35), East and McClure (4), Fisher and Graves (2), and Kuo and Summerfield (36) have formulated complete sets of governing equations for the two-phase reacting flow problem. The interface conditions between the gas and the solid are considered by local continuity of fluxes using empirical correlations. The advantage of using this approach is to be able to lump the detailed flow behavior between the two phases into terms which can be evaluated by using empirical correlations such as heat transfer, flow resistance, intergranular stress and burning rate law.

Mathematically, this problem is approached by deriving the mass, momentum and energy equations for the gas phase and the mass and momentum equations for the solid phase in a transient quasi-one-dimensional form.

In summary, statistical methods are rejected because in this investigation we are interested in the mean values and there is not enough information to evaluate the net contribution of the microscopic fluctuation term. The continuum mechanics methods are not considered because the co-existence of solid and gas are assumed without considering the interpenetrating between the two media. The formal averaging methods are not convenient since they are too mathematical and too abstract for

formulation, and some quantities are not directly measurable in the equations. In order to obtain useful solutions, the complicated integrals in the conservation equations have to be simplified by the proper definition of averaged quantities. The final form of this simplified equation should agree with the equations derived from the two-phase fluid dynamics approach.

The gas-dynamic approach is then formed. Such an approach will provide a clear definition for each term in the governing equations in both phases. Some bulk properties of the fluid defined in the formulation and the gross effects of heat transfer and flow resistance can be measured experimentally.

## CHAPTER II

### LITERATURE SURVEY

In this chapter we provide a literature survey on three different topics, namely (i) a brief survey on existing two-phase, reactive flow combustion models; (ii) empirical correlations such as correlations for heat transfer, flow resistance and intergranular stress; (iii) numerical methods to solve this mathematical model.

#### 2.1 Survey on Related Works

The objective is to summarize the past experiences of various investigators working in this field, so that all important physical phenomena and influencing factors are included in the theoretical model.

Before going into several recent investigations of transient burning of granular propellents, some published work (37, 38) on the steady-state burning of similar propellents are reviewed. Steady-state and transient burning studies are almost inseparable, therefore, some discussions of current steady-state results prove to be worthwhile. Kuo et al (1, 39) show that gas-penetrative burning of porous propellents or explosives under strong confinement is inherently self-accelerating. Kuo and Summerfield (37, 38) have shown that under suitable physical conditions, the internal pressure distribution generated by propellant gasification can produce a constant rate of gas penetration through the unburned region, and may eventually give a constant speed of combustion-wave propagation. Several investigators (40, 41, 42, 43) have observed experimentally, some evidence of steady gas-penetrative burning in porous propellents. Recent attempts were made by various investigators to gain a deeper understanding of the physical phenomena in igniting and burning of granular propellents.

In the consideration of the effect of propellant type on the pressure-time-distance variations, Warlick (44) conducted several experiments on various artillery systems using NACO propellants (the cool-burning propellant which reduces barrel erosion), and comparisons were made with the PYRO propellants. The pressure-time traces obtained at the case base showed no significant difference with propellant type. The pressure-time history at the projectile base is later found to be radically different from those recorded at the cartridge case base. The intensity of the traveling pressure front in the combustion chamber was found to be strongly dependent on primer venting, porosity distribution, and the physical-chemical characteristics of the propellant in the bed. Warlick firmly suggests that interior ballistic systems studies must include the consideration of the above effects to minimize the pressure irregularities.

Soper (10) performed experiments on ignition waves in gun chambers loaded with NACO propellants. His experimental results revealed severe wave action during ignition: a distinct pressure wave traveled down and continued oscillating inside the combustion chamber. A strong pressure spike at the base of the projectile was recorded, (the typical intensity is  $2460.0 \text{ kg/cm}^2$ ). Soper's flash X-ray apparatus detected a pronounced acceleration of propellant particles ahead of the gas pressure wave. This suggests consideration of both the motion of propellants and also the intergranular forces transmitted in compaction beds are equally important.

East and McClure(4) set up a transient interior ballistic model by considering the two phase phenomena. Their mathematical model is not quite complete for the following reasons. They assumed that the initial state of the system is already fully ignited. This assumption defeats the major purpose of analyzing the effect of ignition waves and optimizing the primer

design. In their gas momentum equation, the momentum of reacted mass was incorrect. The solid phase normal stress transmission was excluded in their solid phase momentum equation. In their gas energy equation, they neglected the heat loss to the propellant from the gas phase. Most important, the solid phase energy equation was excluded from their formulation, and the surface temperature of the propellants was not treated.

Gough and Zwarts (3) made a good attempt in formulating a mathematical model for ignition of porous propellants by considering the motion of solid particles and stress transmission in the compacted bed. Their model was far more sophisticated than the East and McClure model. However, a few errors of the model are manifested in the following. Ergun's correlation (45) was used to calculate the force between gaseous and solid particles in both fluidized and non-fluidized sections of the granular bed. But Ergun's correlation is only valid for non-fluidized (fixed) bed. In addition to the internal thermal energy, the total energy addition to the gas phase due to burning should include both the chemical energy, and the flow work which drives the reacted gaseous mass into the space occupied by other gases in the control volume. The flow work was not included in the gas-phase energy equation of their model. Their boundary condition on the projectile end after the shot start was not well specified. Gough and Zwarts' numerical solutions indicated severe oscillations on the boundaries. These spurious waves, generated by numerical instabilities, propagated into the interior and inaccuracies resulted. Gough (12, 46) had improved his model by re-examining the conservation equations and this is discussed later in this section.

Fisher et al (2, 47, 48, 49) studied propellant ignition and combustion processes in several different artillery systems; the geometry involved was

quite different from a one-dimensional model. They considered the combustion processes in the ignition cartridge, the flow of hot reacted gases and propellant radially through the vent holes on the wall of the ignition cartridge, and the combustion of the bag propellant. Although the motion of propellants is considered by the conservation equations for the propellants, the models are incomplete and their predictions have not been verified thoroughly by experimental data.

Krier et al (5, 50, 99) approached the two-phase granular propellant burning problem in a different manner. They took the continuous mechanics approach for both gaseous and solid phases. They treated the propellant particles as a fluid. However, the fluid and solid media differ distinctly by the characteristic differences in stress tensor. In a fluid it is proportional to the rate of angular deformation, whereas the stress tensor in a solid medium is proportional to the magnitude of deformation. To analyze the cause of generation of the pressure spike at the base of the projectile and the wave action in the unburned propellant, the stress transmission in the solid material must be treated differently from the stress-to-strain-rate relationship for fluids. In addition, the energy equation for the solid phase was written in terms of global stored energy. This lumped parameter is not adequate for studying the flame propagation and for calculating the heat transfer from the hot gas to the unburned propellants. The conduction process inside the solid propellant is a relatively slow process in comparison with the overall transient characteristic of flame spreading. The temperature profile within the solid particles must have a sharp gradient; it is vague to use a lumped parameter in the solid phase energy equation. The investigators realized the importance of suitable empirical correlations for the fluidized and non-fluidized bed

and they collected a brief survey on existing correlations for heat transfer and flow resistance. The boundary treatment is inadequate since the reflection conditions are used at the boundaries.

Gough (12, 46) in his more recent study, has investigated the interior ballistics of guns by considering the microscopic equations of motion based on integral and explicit averaging approach. His approach is predicated upon a combination of the methods of Anderson and Jackson (29), Whitaker (30) and Paxton (31). A weighting function is adopted for the definition of all the average flow properties. Overall, this proved to be a useful scheme to derive a set of conservation equations directly from the microscopic point of view to give the flow properties in the microscopic sense. But, this approach is too mathematical and too abstract to give tangible physical meanings to each term in the conservation equations. Gough's model still uses the Ergun equation for fluidized and packed beds. It has not been verified by some of the rigorous, one-dimensional experiments. With a continuous improvement in the boundary point treatment and accurate forcing function specification, it is expected that Gough's model should give close predictions to the results of our model.

## 2.2 Survey of Empirical Correlations and Their Limitations

In constructing a complete theoretical model, some information besides the major conservation equations are necessary. These empirical correlations serve to determine heat transfer in the granular bed, drag forces between particles and gases, and stress transmitted through closely packed granular propellents.

An extensive literature survey was conducted to collect available correlations on heat transfer and drag data for non-fluidized and fluidized beds. The chemical engineering industry generated the majority of the available correlations. A large quantity of fluidization studies have been contained in hundreds of reports and papers, and also in textbooks by Zenz and Othmer (51), Leva (52), Kenū and Levenspiel (53), Soo (54), and Davidson and Harrison (55). Unfortunately, empirical correlations that cover a wide range of Reynolds numbers and porosities, particle size and also include the effect of particle gasification, are unavailable. Krier et al (5) encountered the same problem in their recent report. As a result, the empirical correlations for flow over inert spheres in non-fluidized and fluidized beds are employed in various combustion models, and even extrapolation to larger range of Reynolds numbers and porosities to continue with the calculations on a computer.

Since no suitable drag correlation is available for a wide range of Reynolds number and porosity, we performed a large number of cold flow experiments and obtained a useful correlation between the pressure drop, Reynolds number and porosity for non-fluidized beds of WC 870 propellents (76). The Reynolds number has been extended to be six times higher than that in Ergun's equation. For fluidized regions, Andersson's Correlation (56) has been found to be a suitable empirical formula, since it is valid for

porosity from 0.45 to 1.0. However, it must be noted that the Reynolds number varies only from 0.003 to 2000 in his correlation. It must be used with caution.

For convective heat transfer calculations, Denton's (57) formula is found to be adequate for the non-fluidized region. It is valid for  $Re_p$  from 500 to 50,000 and porosity around 0.37. Rowe-Claxton's correlation (58) is found to be the best one for describing the convective heat transfer in fluidized regions. This expression is valid for  $Re_p$  from 10 to  $10^7$ , and porosity from 0.26 to 0.632.

A constitutive law is needed to specify the normal stress transmission through packed granular particles. When particles are dispersed, the intergranular stress,  $\tau_p$  is zero. When the particles are packed,  $\tau_p$  may be large due to the physical contact between the particles under steep pressure gradients.

After a literature survey on intergranular stress correlations, it is found that not much information is available. Soper (10) observed that the force and displacement of a piston acting on a granular bed of NACO propellents, were linearly related within the range of 0 to 35% compression. The speed of sound in granular propellant was deduced from his experimental data. Besides Soper's work, the dependence of particulate stress tensor upon porosity of the mixture was given by Hoist (59) and Gough (12). Further discussion on  $\tau_p$  is given in Appendix 6.

### 2.3 Survey on Numerical Studies

After the theoretical formulation is completed and the nature of the governing equations is studied, a literature survey in selecting a stable and fast convergent numerical scheme has been conducted.

Obviously, the theoretical model is a system of coupled, non-linear, inhomogeneous partial differential equations. Since the eigenvalues are all real, the system is hyperbolic. In order to select a suitable numerical scheme, two important criteria must be noted in making such a decision. They are the stability and convergence of the scheme. Papers, reports as well as textbooks, have numerous types of finite-difference schemes to handle hyperbolic partial differential equations. Moretti (60) makes a good comparison of the differences of some numerical schemes. The stability criteria has been studied for each scheme. In practice, a rigorous stability analysis of the set of coupled non-linear partial differential equations cannot be performed due to the complexity and non-linearity of the equations. For the study of non-linear systems of equations, Hicks (61) suggests disregarding the study of stability criteria and proceeds directly to the heart of the problem, namely, the convergence. This was also discussed by Lax and Richtmyer (62). Basically, the FDE (finite-difference equation) solution must approach the PDE (partial differential equation) solution, and stability criteria then becomes of secondary interest. As a result, several convergence tests were suggested to test the numerical solution's convergence to the unique solutions of the system of partial differential equations.

None of the criteria or analyses are adequate for practical computations. In actual fluid flow problems, the stability restrictions are applied locally. The typical and prudent practice is to use some percentage, usually 80% or 90% of an analytically-indicated maximum time step. When transients

are large, smaller percentages are needed to stabilize the solution. For example, Terrance (63) has done some computations on natural convection by using a smaller  $\Delta t$  to achieve computational stability.

The shortcomings of the above approach are not very apparent. Investigators such as Phillips (64), Richtmyer (65), Hirt (66) and Gourlay and Morris (67) have reported instabilities from nonlinearity or from non-constant coefficients. Lilly (68) has reported the phenomena of time splitting of solutions which is not precisely an instability in the sense of producing unbounded solutions, actually an instability due to interactive convergence. Therefore, it is important to realize that no distinct difference exists between a "time" instability and a poor convergence.

Overall, four methods are studied in detail to evaluate the stability of the numerical scheme, namely, the Courant-Friedricks-Lewy (C.F.L.) (69) conditions, the Energy Method (70), the von Neumann method (71) and the Heuristic Stability Theory of Hirt (66).

In the selection of numerical scheme for the hyperbolic governing equations, several different schemes are considered: the method of Courant, Isaacson and Rees (72), the Lalevier scheme (70), the two step Lax-Wendroff scheme (65), the up Prog scheme (22), the two-step Richtmyer scheme (60), the generalized implicit scheme (70), the method of characteristics (74) and the method of lines (78). From the previous investigators' experience we finally decided upon a modified two-step Richtmyer scheme. This will be discussed in detail in Chapter IV.

## CHAPTER III

### THEORETICAL FORMULATION AND ANALYSIS OF TRANSIENT COMBUSTION PROCESSES IN GRANULAR BEDS

We begin this chapter with the description of the physical processes that occur in an actual firing. Then, after a brief discussion of some basic assumptions in this model, we formulated our mathematical model by describing the physical meaning of each term in the conservation equations of mass, momentum and energy of the gas phase; and the conservation equations of mass and momentum of the particle phase. The energy equation of the particle phase is treated separately. The conservation equations derived in section 3.3 are very general in nature. In order to arrive at a set of equations that can be solved economically on the computer, various simplifications are made in section 3.4.

A set of governing equations in the entrance region are derived to facilitate the calculations at the left boundary. The nature of the governing equations are determined in section 3.6 and detailed mathematical steps are shown in appendix 3 and 4. Initial and boundary conditions are specified in section 3.7, further discussions on the numerical treatment of the boundary conditions are given later.

In order to close this problem, associated empirical correlations and limitations, such as

- A. Constitutive law for the total stress
- B. Drag correlation
- C. Heat transfer correlation
- D. Burning rate law

and the ignition criterion for the solid propellant are separately discussed in the remaining of the chapter.

### 3.1 Description of Physical Processes

In preparation for an experimental firing, spherical granular (WC 870) propellents are loaded into a thick-walled cylindrical steel chamber with 15.24 cm in length and 0.777 cm I.D. (Fig. 1). At the left end of the cylindrical chamber there is a gaseous pyrogen igniter which introduces hot gas into the granular bed by forcing it through a multiple perforated nozzle to achieve a uniform stream. At the right end of the cylindrical chamber, there is a 0.81 mm stainless-steel shear disc "burst diaphragm", (this provides a fixed boundary). As the igniter gas is turned on, the hot igniter gases generated cause a compaction of the granular bed near the entrance region. This also heats up the nearby granular propellents to ignition condition. The burned propellents give off more hot gases, these gaseous products are then pushed forward by the pressure gradient to ignite more propellents. Thus, a steep pressure gradient is created inside the combustion chamber. The rate of pressurization increases further in the downstream direction, resulting in a rapid acceleration of the flame front. The shear disc begins to rupture when the pressure in front of it reaches a critical value. After the shear disc bursts, the combustion chamber pressure decreases abruptly and terminates the event.

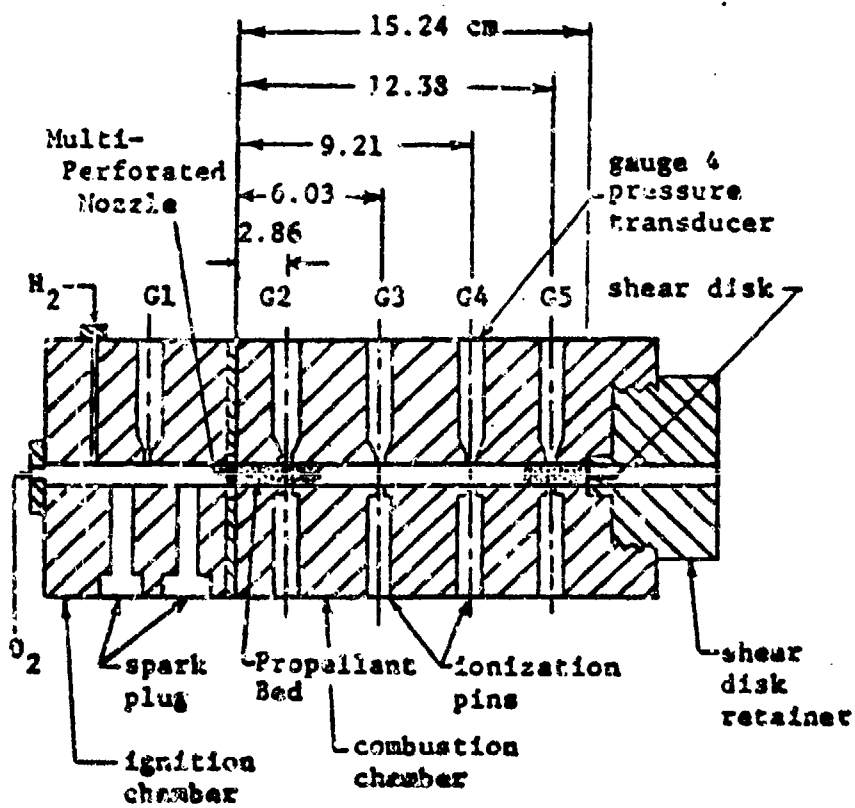


Figure 1 Schematic Drawing of the Ignition and Combustion Chamber

### 3.2 Basic Assumptions

There are 3 basic assumptions pertinent to this present study:

1. The flow in the granular bed is considered to be quasi-one-dimensional. The effect of fluctuations in the flame front for two-dimensional or three-dimensional models may be obtained with further modifications. In this model the changes of flow properties in the transverse direction are considered in the empirical correlations for heat transfer are flow resistances.
2. All chemical reactions occur on the propellant surface, in the combustion zone, a thin region that is very small in comparison with initial particle diameter.
3. The dynamic burning effect is negligible i.e. the rate processes at the propellant surface are quasi-steady in the sense that the characteristic times associated with the gaseous flame and preheated propellant are short compared to that of the pressure transient variations.

### 3.3 Theoretical Model

In order to study the detailed structure of the transient gas dynamic behavior of hot-gas penetration, flame propagation, chamber pressurization and combustion processes in the granular propellant bed, a set of governing equations describing the changes of mass, momentum, and energy for the gas phase and the changes of mass, momentum for the solid phase are derived. This set of governing equations is expressed in a quasi-one-dimensional form. The equations are approached by considering the balance of fluxes over a control volume small enough to give the desired spatial distributions in the complete system, yet large enough to contain many solid particles, so that the averaged particle velocity and fraction porosity are meaningful.

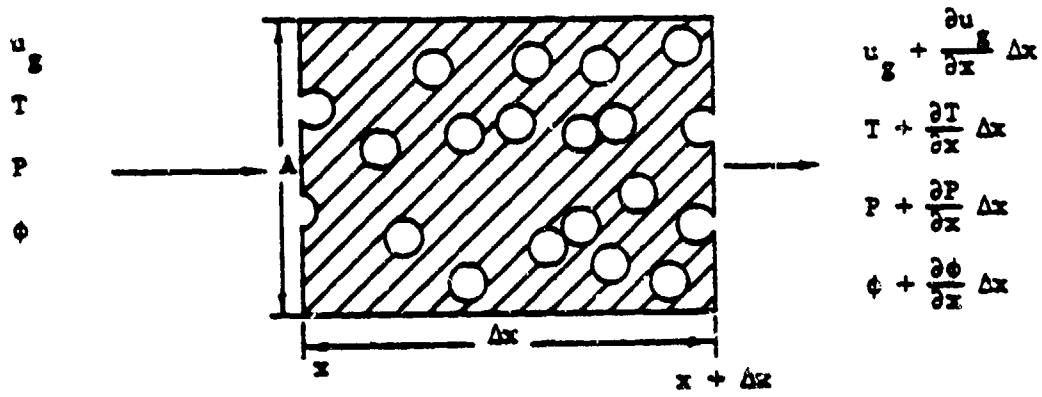
The control volume for the gas-phase is the portion of void volume occupied by the gas phase in a small elementary volume ( $A\Delta x$ ), while the remaining portion occupied by the particles is considered to be the control volume for the particle phase (Fig. 2).

#### A Conservation of Mass Equations

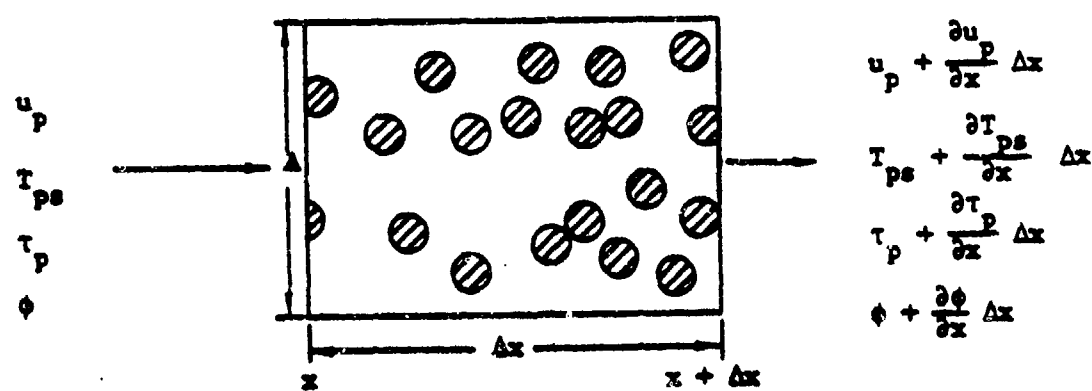
In deriving the gas phase conservation equation  $\phi$ , the fractional porosity is defined as

$$\begin{aligned}\phi &= \frac{\text{void volume}}{\text{total volume}} = 1 - \frac{n(\frac{4}{3}\pi r_p^3)}{A\Delta x} \\ &= 1 - \tilde{n}(\frac{4}{3}\pi r_p^3)\end{aligned}\tag{3.3.1}$$

Where  $n$  is the number of pellets in the cylindrical volume



(a) Gas-Phase Control Volume



(b) Particle-Phase Control Volume

Figure 2 Control Volumes Considered in the Analysis

$A \Delta x$ , and  $r_p$  is the pellet radius in the control volume.  $n$  is the number density of spherical pellets in the granular propellant bed. The specific surface area which represents the total surface area per unit spatial volume is given by

$$A_s = \frac{\pi(4\pi r_p^2)}{A \Delta x} = \frac{3(1-\phi)}{r_p} \quad (3.3.2)$$

The gas-phase mass equation is

$$\frac{\partial(\rho\phi)}{\partial t} + \frac{\partial(\rho u_g \phi)}{\partial x} = A_s \rho_p \Gamma_b \quad (3.3.3)$$

The rate of gaseous mass accumulation in the control volume occupied by gases

The rate of increase of gaseous mass by convection

The rate of gaseous mass addition due to gasification of solid particles

The particle-phase mass equation is

$$\frac{\partial[(1-\phi)\rho_p]}{\partial t} + \frac{\partial[(1-\phi)\rho_p u_p]}{\partial x} = -A_s \rho_p \Gamma_b \quad (3.3.4)$$

The rate of particle mass accumulation in the control volume occupied by particles

The rate of increase of particle mass by convection

The rate of particle mass reduction due to gasification of solid particles

In this analysis, the gas density  $\rho$  is based on the gaseous mass divided by the void volume occupied by the gases. The propellant density,  $\rho_p$  is assumed to be constant.

B The Conservation of Momentum Equations

The gas-phase momentum equation is

$$\frac{\partial(\phi \rho u_g)}{\partial t} + \frac{\partial(\phi \rho u_g^2)}{\partial x} + g \frac{\partial(\phi P)}{\partial x} -$$

The rate of increase of gaseous momentum in the control volume

The rate of momentum flux increase in the control volume by convection

Pressure gradient force acting in the x-direction

$$- g \frac{\partial(\tau_{xx} \phi)}{\partial x} - A_s \Gamma_b \rho_p u_p - g A_s D_i$$

Viscous force due to normal stresses

The rate of increase of linear momentum of gas phase due to the motion of gasifying particles in the momentum direction

The total drag force between the gas and particle phases

$$- g \frac{\tau_{wx} P_{m1}}{A} \quad (3.3.5)$$

Friction force acting on the gas by the chamber wall

The particle-phase momentum equation is

$$\frac{\partial[(1-\phi)P_p u_p]}{\partial t} + \frac{\partial[(1-\phi)P_p u_p^2]}{\partial x} - g \frac{\partial[(1-\phi)\tau_p]}{\partial x}$$

The rate of increase of particle momentum in the control volume

The rate of momentum flux increase in the control volume by convection

Intergranular force acting on particle cross-sectional areas on the boundary of the control volume

$$- A_s \Gamma_b P_p u_p + g A_s D_t - g \frac{\tau_{wp} P_{wp}}{A} \quad (3.3.6)$$

The rate of decrease of particle momentum due to gasification of particles into gas phase

The total drag force between the gas and particle phase

Friction force acting on the particle by the chamber wall

It is important to note that  $D_t$  is the total drag force between the gas and particle phases. It is equal to the sum of the drag due to the presence of relative velocity between the gas and particle phases and the drag due to the porosity gradient, i.e.

$$D_t = D_v + D_p = D_v - \frac{P}{A_s} \frac{\partial \phi}{\partial x} \quad (3.3.7)$$

The expression of  $D_v$  will be discussed in a later part of the theoretical model. The advantage of writing the above two momentum equations in terms of  $D_t$  is to facilitate the solution of the hyperbolic problem which is not always totally hyperbolic. The eigenvalues may not be all

distinct when the granular bed becomes dispersed. The second advantage is to facilitate the transformation of the governing equations into the characteristic form and to clearly indicate the compatibility relations for the flow properties at the boundaries of the granular bed.

### C The Conservation of Energy Equation

The gas-phase energy equation is

$$\frac{\partial(\phi PE)}{\partial t} + \frac{\partial(\phi P u_g E)}{\partial x} + \frac{1}{J} \frac{\partial(P u_g \phi)}{\partial x}$$

The rate of increase of total stored energy in control volume

The rate of energy flux increase by convection

The rate of work done on the gas phase by pressure force

$$- \frac{\partial(q\phi)}{\partial x}$$

The rate of heat conduction through the control surfaces

$$- \frac{A_s u_p D_t}{J}$$

Work done per unit time by the total drag force acting on particles

$$- A_s h_c (T - T_{\infty})$$

Heat loss to particles per unit time

$$+ A_s \rho_p r_b (h_{chem} + \frac{u_p^2}{2gJ})$$

The rate of total energy input due to the combustion of particles

$$+ \frac{1}{J} \frac{\partial(T_{xx} u_g \phi)}{\partial x}$$

The rate of work done by viscous normal stress in the gas phase

$$-\frac{P}{J} \frac{\partial(\phi)}{\partial t} \quad -\dot{Q}_w \quad (3.3.8)$$

The rate of pressure work for the dilatation of the gaseous control volume

The rate of heat loss to the combustor wall per unit volume

The empirical correlation for  $h_c$  will be shown later. The parameter  $J$  is the heat-to-work unit conversion factor. The conservation equations in Eulerian form are shown in Appendix 1. The above set of governing equations are derived in the form of coupled, non-linear, inhomogeneous partial differential equations. Further simplifications are required to solve them economically.

#### D Solid-Phase Heat Conduction Equation

A particle-phase energy equation similar to Eq. (3.3.8) can be derived in terms of the average bulk temperature of a typical solid particle in the particle-phase control volume considered. However, since the transient interval of the physical process is so short, the temperature profile inside the particles has a very steep gradient. Although the average bulk temperature of a solid particle can be obtained, it would not be useful for determining the ignition condition, the speed of flame front propagation, or the rate of heat transfer from the gas to solid phase. Instead of treating the solid phase energy equation like the mass and momentum equations for the particles, the transient heat conduction equation is considered, so that the propellant surface temperature and the temperature gradient can be accurately obtained.

Following the motion of a given particle, the heat equation written in the Lagrangian time derivative and spherical coordinate of the particle is (see Fig. 25)

$$\left(\frac{DT_P}{Dt}\right)_P = \frac{\alpha_P}{r} \frac{\partial^2(rT_P)}{\partial r^2} \quad (3.3.9)$$

The initial condition for equation (3.3.9) is:

$$t = 0 : T_P(0, r) = T_0 \quad (3.3.10)$$

The boundary conditions before the thermal wave has penetrated to the center of the sphere are:

$$r = 0 : \frac{\partial T_P}{\partial r}(t, 0) = 0 \quad (3.3.11)$$

$$r = r_p : \frac{\partial T_P}{\partial r}(t, r_p) = \frac{h_c(t)}{k_P} [T(t) - T_{ps}(t)] \quad (3.3.12)$$

where the total heat transfer coefficient,  $h_c$ , is the sum of the convection and radiation coefficients; i.e.

$$h_c(t) = h_c(t) + \epsilon_p \sigma [T(t) + T_{ps}(t)][T^2(t) + T_{ps}^2(t)] \quad (3.3.13)$$

where the gas emissivity is taken to be unity.

The heat-up equation and its initial and boundary conditions are recasted by the integral method as shown in Appendix 2 to yield a

first order ordinary differential equation describing the increase of propellant surface temperature with respect to time, i.e.

$$\left(\frac{DT_{ps}}{Dt_p}\right) = \frac{\frac{1}{2} \rho_p \left[ T_{ps} - T_0 + \frac{r_p h_c}{k_p} (T - T_{ps}) \right] + \delta \left[ \frac{h_c}{k_p} \left( \frac{DT}{Dt} \right) + \frac{T - T_{ps}}{k_p} \left( \frac{Dh_c}{Dt} \right) \right]}{\left[ \frac{6\Gamma_p - \delta}{\Gamma_p} + \frac{h_c \delta}{k_p} \right]} \quad (3.3.14)$$

where  $\delta$  is the thermal wave penetration depth in a spherical particle, measured from the particle surface;  $\delta$  as a function of time is given by:

$$\delta(t) = \frac{3\Gamma_p [T_{ps}(t) - T_0]}{\left[ T_{ps}(t) - T_0 \right] + \frac{r_p h_c(t)}{k_p} [T(t) - T_{ps}(t)]} \quad (3.3.15)$$

Similarly, an ordinary differential equation describing the changes of  $T_{ps}$  after the thermal wave has penetrated the full radius of a spherical particle is obtained. Since the transient interval of the physical process is only a few milliseconds, the particle surface reaches the ignition condition long before the thermal wave penetrates to the center of the particle; the equation describing the changes of  $T_{ps}$  after the thermal wave penetration is not given here but will be shown in Appendix 2. After  $T_{ps}$  is solved, a simplified ignition temperature criterion is used to determine the burning condition of particles along the propellant bed. The ignition criterion is given in section 3.9.

### 3.4 Simplifications

Before the necessary boundary conditions are considered, the governing equations for the gas and particle phases are simplified further after an order of magnitude analysis. The higher-order terms neglected are: (a) the viscous normal stress in the gas-phase momentum equation, (b) the shear force at the combustor wall for both gases and particles in their momentum equations, (c) the gas-phase heat conduction term, (d) the work done by the viscous normal stress in the gas-phase energy equation, (e) the heat loss  $\dot{Q}_w$  to the chamber wall in the extremely short transient combustion experiments, (f) the rate of pressure work for the dilatation of the gaseous control volume in the gas-phase energy equation, and (g) the rate of change of the total heat transfer coefficient in the calculation of propellant surface temperature, (h) body force, (i) dynamic burning effect on the burning rate calculations, (j) temperature dependence of constant pressure specific heat, (k) heat dissipation, (l) constant cross-sectional area.

After all these assumptions, a simplified set of governing equations will be rewritten in the following.

The gas-phase equation becomes,

$$\frac{\partial(\rho\phi)}{\partial t} + \frac{\partial(\rho u\phi)}{\partial x} = A_s \rho_p \Gamma_b \quad (3.4.1)$$

The particle-phase mass equation becomes,

$$\frac{\partial[(1-\phi)\rho_p]}{\partial t} + \frac{\partial[(1-\phi)\rho_p u_p]}{\partial x} = -A_s \rho_p \Gamma_b \quad (3.4.2)$$

The gas-phase momentum equation becomes,

$$\frac{\partial(\phi P u_g)}{\partial t} + \frac{\partial(\phi P u_g^2)}{\partial x} + g \frac{\partial(\phi P)}{\partial x} = -A_s \Gamma_b P_p u_p - g A_s D_t \quad (3.4.3)$$

The particle-phase momentum equation becomes,

$$\frac{\partial[(1-\phi)P_p u_p]}{\partial t} + \frac{\partial[(1-\phi)P_p u_p^2]}{\partial x} - g \frac{\partial[(1-\phi)\tau_p]}{\partial x} = -A_s \Gamma_b P_p u_p + g A_s D_t \quad (3.4.4)$$

The gas-phase energy equation becomes,

$$\frac{\partial(\phi P E)}{\partial t} + \frac{\partial(\phi P u_g E)}{\partial x} + \frac{1}{J} \frac{\partial(P u_g \psi)}{\partial x} = -\frac{A_s u_p D_t}{J} - A_s h_c (T - T_{ps}) + A_s P_p \Gamma_b (h_{chem} + \frac{u_p^2}{2gJ}) \quad (3.4.5)$$

The particle-phase heat-up equation becomes,

$$\frac{(DT_p)}{Dt_p} = \frac{\frac{12\alpha P}{\delta r_p} [T_{ps} - T_o + \frac{r_{ps} h_c}{k_p} (T - T_{ps})] + \frac{h_c \delta}{k_p} \left( \frac{DT}{Dt_p} \right)}{\left[ \frac{6\Gamma_b \delta}{r_p} + \frac{h_c \delta}{k_p} \right]} \quad (3.4.6)$$

The above equations (3.4.1) - (3.4.6) are the simplified form of the governing equations (3.3.3) - (3.3.6), (3.3.8) and (3.3.14). These equations are coded directly into the computer program.

### 3.5 Governing Equations in the Left Control Volume

The mass equation of the gas phase in the left control volume (Fig. 3) is

$$\frac{d(\phi_c P)}{dt} = \frac{1}{AX_L} [\dot{m}_{ign}(t) - \dot{m}_{in}(t, X_L)] + A s_c \Gamma_c P_c \quad (3.5.1)$$

where  $\dot{m}_{ign}(t)$  is the ignitor mass flow rate into the combustion chamber and  $\dot{m}_{in}(t, X_L)$  is the mass flow rate of gas into the internal boundary of the granular bed, it is represented by

$$\dot{m}_{in}(t, X_L) = \rho(t, X_L) u_g(t, X_L) A \phi(t, X_L) \quad (3.5.2)$$

The mass equation of the particle phase is

$$\frac{d\phi_c}{dt} = A s_c \Gamma_c + \frac{(1-\phi) u_p}{X_L} \Big|_{X_L} \quad (3.5.3)$$

Same as above all the parameters with a subscript c are evaluated in the entrance section.

The momentum equation of the gas phase is

$$\begin{aligned} \frac{d(\rho_c u_g \phi_c)}{dt} = & \frac{1}{AX_L} (\dot{m}_{ign}(t) u_{g_{ign}} - \rho u_g^2 A \phi|_{X_L}) \\ & + A s_c (\Gamma_c P_c u_{p_c} - g D_c) \end{aligned} \quad (3.5.4)$$

where  $u_{g_{ign}}$ , the ignitor gas velocity is given by

$$u_{g_{ign}} = \frac{|\dot{m}_{ign}|}{(A \rho_c P_c)} \quad (3.5.5)$$

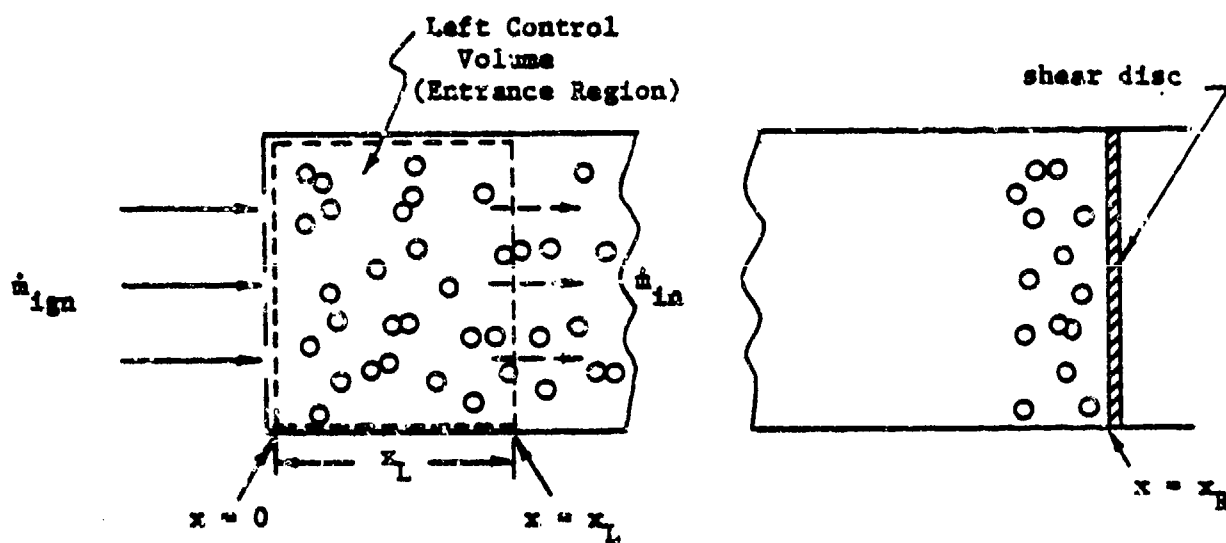


Figure 3 Control Volume Considered in the Left Boundary

Similarly the momentum equation of particle phase is derived in the differential form,

$$\frac{d[(1-\phi_c)P_p U_p]}{dt} = - \left[ \frac{(1-\phi)P_p U_p^2}{X_L} \right]_{x_L} + A_{sc}(gD_c - r_{bc} P_p U_p) \quad (3.5.6)$$

For the control volume considered in Fig. 3, the energy equation of the gas phase in the differential form is

$$\begin{aligned} \frac{d(P_c \phi_c E_c)}{dt} &= \frac{1}{AX_L} \left[ \dot{m}_{ign}(t) \left( h_{ign} + \frac{U_{ign}^2}{2gJ} \right) \right. \\ &\quad \left. - \rho U_g A \phi \left( C_p T + \frac{U_g^2}{2gJ} \right) \right]_{x_L} \\ &\quad + A_{sc} \left[ - \frac{D_c U_p}{J} - h_{tc} (T_c - T_{psc}) \right. \\ &\quad \left. + P_p r_{bc} \left( h_{chem} + \frac{U_p^2}{2gJ} \right) \right] \end{aligned} \quad (3.5.7)$$

where  $E_c$  is the total stored energy, the sum of thermal and kinetic energy which is represented by

$$E_c = C_v T_c + \frac{U_g^2}{2gJ} \quad (3.5.8)$$

$h_{ign}$  is the enthalpy of the igniter gas at the temperature of the hot igniter gas and  $h_{chem}$  is the enthalpy of the propellant gas at flame temperature.

The last equation being considered is the solid-phase heat equation in two forms

(a) Time Period 1

$$\left(\frac{DT_{ps}}{Dt}\right)_p = \frac{\frac{12\alpha_p}{\delta_c \Gamma_p} [(T_{ps} - T_o) + \frac{\Gamma_p h_{c_s}}{k_p} (T_c - T_{ps})] + \frac{h_{c_s} \delta_c}{k_p} \left(\frac{DT_c}{Dt}\right)_p}{\left[\frac{(6\Gamma_p - \delta_c)}{\Gamma_p} + \frac{h_{c_s} \delta_c}{k_p}\right]} \quad (3.5.9)$$

(b) Time Period 2

$$\left(\frac{DT_{ps}}{Dt}\right)_p = \frac{\frac{3\alpha_p h_{c_s}}{2k_p \Gamma_p} (T_c - T_{ps}) + \frac{\Gamma_p h_{c_s}}{8k_p} \left(\frac{DT_c}{Dt}\right)_p}{\left(\frac{1}{2} + \frac{\Gamma_p h_{c_s}}{8k_p}\right)} \quad (3.5.10)$$

In the left control volume, there are a total of six unknowns:

$$\phi_c, \rho_c, u_{g_c}, u_{p_c}, E_c, T_{ps_c}$$

From Eq. (3.5.3),  $\phi_c$  is explicitly defined.

$\rho_c$  is then defined by substituting Eq. (3.5.3) into Eq. (3.5.1)

it becomes

$$\frac{dP_c}{dt} = \frac{1}{\phi_c} \left\{ \frac{(\dot{m}_{ign}(t) - \dot{m}_{in}(t))}{AX_L} + A_{sc} \Gamma_{bc} P_{pc} - P_c \frac{d\phi_c}{dt} \right\} \quad (3.5.11)$$

Similarly from Eq. (3.5.4) we obtain,

$$\begin{aligned} \frac{dU_g}{dt} = \frac{1}{\rho_c \phi_c} \left\{ \frac{(\dot{m}_{ign}(t) U_{sign} - P U_g^2 A \phi_c |_{x_L})}{AX_L} + A_{sc} (\Gamma_{bc} P_{pc} U_{pe} - g D_c) \right. \\ \left. - P_c U_{gc} \frac{d\phi_c}{dt} - \phi_c U_{gc} \frac{d\rho_c}{dt} \right\} \quad (3.5.12) \end{aligned}$$

By the same token, Eq. (3.5.7) becomes

$$\begin{aligned} \frac{dE_c}{dt} = \frac{1}{\rho_c \phi_c} \left\{ \frac{1}{AX_L} \left[ \dot{m}_{ign}(t) \left( h_{ign} + \frac{U_{sign}^2}{2gJ} \right) - P U_g A \phi_c \left( C_p T + \frac{U_g^2}{2gJ} \right) \right] \right. \\ \left. + A_{sc} \left[ - \frac{D_c U_g}{J} - h_{tc} (T_c - T_{sc}) + P_{pc} \Gamma_{bc} \left( h_{chem} + \frac{U_{pe}^2}{2gJ} \right) \right] \right. \\ \left. - \phi_c E_c \frac{d\rho_c}{dt} - E_c P_c \frac{d\phi_c}{dt} \right\} \quad (3.5.13) \end{aligned}$$

Then gas temperature can be evaluated by rearranging Eq. (3.5.13), using

$$T_c = \frac{1}{C_v} \left[ E_c - \frac{U_g^2}{2gJ} \right] \quad (3.5.14)$$

The equation of state from Eq. (3.5.1) after rearranging we get,

$$P_c = \frac{RT_c J}{\left(\frac{1}{\beta_c} - b\right)} \quad (3.5.15)$$

In summary  $\phi_c$ ,  $u_{g_c}$ ,  $u_{p_c}$ ,  $T_c$ ,  $P_c$ ,  $T_{ps_c}$  are found from Eq. (3.5.3), Eq. (3.5.4), Eq. (3.5.6), Eq. (3.5.8), Eq. (3.5.9) or (3.5.10) and Eq. (3.5.15) respectively. All these parameters are used to solve for the left boundary conditions.

Another set of governing equations are derived at the left control volume when there are no particles existing in the entrance region. When there are no particles in the region, that implies that

$$\phi_c = 1 \quad (3.5.16)$$

and

$$u_{p_c} = 0 \quad (3.5.17)$$

The mass equation of gas phase reduces to

$$\frac{dP_c}{dt} = \frac{(\dot{m}_{in} - \dot{m}_n)}{AX_c} \quad (3.5.18)$$

and the momentum equation of the gas phase becomes

$$\frac{du_{g_c}}{dt} = \frac{1}{P_c} \left\{ \frac{(\dot{m}_{in} u_{g_{in}} - P_c u_{g_c}^2 A \phi |_{x_c})}{AX_c} - u_{g_c} \frac{dP_c}{dt} \right\} \quad (3.5.19)$$

As a result, energy equation becomes,

$$\frac{dE_c}{dt} = \frac{1}{\rho_c} \left\{ \left[ \dot{m}_{ign} \left( h_{ign} + \frac{u_{g,ign}^2}{2gJ} \right) - \rho u_g A \phi \left( C_p T - \frac{u_g^2}{2gJ} \right) \right]_{x_L} \right\} / A x_L - E_c \frac{d\rho_c}{dt} \quad (3.5.20)$$

and  $T_{ps}$  calculation is simpler, by the time all the particles are pushed out of the entrance region, the ignition temperature of the particles have already been reached,

$$T_{ps_c} = T_{ign} \quad (3.5.21)$$

The above equations, (3.5.16) - (3.5.21) will be used when the left control volume contains no particles.

### 3.6 Eigenvalue Determination of the System

To study the nature of the governing equations, the eigenvalues of the system must be determined. By substituting the governing equations in the Eulerian form into a matrix form

$$\frac{\partial}{\partial t} \begin{bmatrix} u_g \\ T \\ P \\ u_p \\ \phi \end{bmatrix} - \begin{bmatrix} -u_g & 0 & \frac{-g}{\rho} & 0 & \frac{-gP}{\rho P} \\ \frac{-P}{\rho C_p} & -u_g & 0 & 0 & 0 \\ -\frac{C_p P}{g} & 0 & -u_g & \frac{(1-\phi)P}{\rho \beta T} & 0 \\ 0 & 0 & 0 & -u_p & \frac{c^2}{(1-\phi)} \\ 0 & 0 & 0 & (1-\phi) & -u_p \end{bmatrix} \begin{bmatrix} u_g \\ T \\ P \\ u_p \\ \phi \end{bmatrix} + \begin{bmatrix} I_1 \\ I_2 \\ I_3 \\ I_4 \\ I_5 \end{bmatrix} \quad (3.6.1)$$

where  $I_1, I_2, I_3, I_4, I_5$  are the inhomogeneous terms of the governing equations and are defined as

$$I_1 = \frac{A_2}{\phi \rho} [\rho_p \Gamma_b (u_p - u_g) - g D_2]$$

$$I_2 = \frac{A_2}{\rho C_p} \left\{ (u_g - u_p) \left( \frac{D_2}{g} + \frac{u_p \Gamma_b}{g} \right) + h_r (T - T_{ref}) + \rho_p \Gamma_b \left[ h_{conv} - C_p T + \frac{1}{2g} (u_p^2 - u_g^2) \right] \right\}$$

$$I_3 = \frac{A_2}{\beta T} \left\{ \frac{\rho_p \Gamma_b}{\rho \beta T} - \frac{\beta T}{\rho} + \frac{P}{\rho C_p} \left\{ (u_g - u_p) \left( \frac{D_2}{g} + \frac{u_p \Gamma_b}{g} \right) + h_r (T - T_{ref}) + \rho_p \Gamma_b \left[ h_{conv} - C_p T + \frac{u_p^2 - u_g^2}{2g} \right] \right\} \right\}$$

$$I_4 = \frac{A_2 g D_2}{\rho_p (1-\phi)}$$

$$I_5 = A_2 \Gamma_b$$

(3.6.2)

Now we define the matrix  $\bar{M}$  as:

$$\bar{M} = \begin{bmatrix} -u_g & 0 & \frac{-g}{\rho} & 0 & \frac{-gP}{\rho P} \\ \frac{-P}{\rho P C} & -u_g & 0 & 0 & 0 \\ -\frac{C_g P}{g} & 0 & -u_g & \frac{-1-gP^2}{\rho P R T} & 0 \\ 0 & 0 & 0 & -u_p & \frac{c^2}{(1-\phi)} \\ 0 & 0 & 0 & (1-\phi) & -u_p \end{bmatrix} \quad (3.6.3)$$

by setting  $|\bar{M} - \lambda \bar{I}| = 0$  we can obtain the eigenvalues. Detailed mathematical steps are shown in Appendix 4.

The six roots found are as follows:

$$\begin{aligned} \lambda_1 &= -(u_g + C_g) \\ \lambda_2 &= -(u_g - C_g) \\ \lambda_3 &= -u_g \\ \lambda_4 &= -(u_p + C) \\ \lambda_5 &= -(u_p - C) \\ \lambda_6 &= -u_p \quad \text{(obtained directly by following the} \\ &\quad \text{motion of a given solid particle)} \end{aligned} \quad (3.6.4)$$

Since all these six roots are distinct real numbers for non-fluidized condition, the system of governing equations is totally hyperbolic (97).

The slope of the characteristic lines for the governing equations are determined by the local gas velocity and the speed of sound. The characteristic directions are described by

$$\left(\frac{dx}{dt}\right)_x = \lambda_1 = u_g + C_g \quad (3.6.5)$$

$$\left(\frac{dx}{dt}\right)_x = \lambda_2 = u_g - C_g \quad (3.6.6)$$

$$\left(\frac{dx}{dt}\right)_x = \lambda_3 = u_g \quad (3.6.7)$$

$$\left(\frac{dx}{dt}\right)_x = \lambda_4 = u_p + C \quad (3.6.8)$$

$$\left(\frac{dx}{dt}\right)_x = \lambda_5 = u_p - C \quad (3.6.9)$$

$$\left(\frac{dx}{dt}\right)_x = \lambda_6 = u_p \quad (3.6.10)$$

In the subsonic case, Eq. (3.6.5), Eq. (3.6.6) and Eq. (3.6.7) represent the right-running, left-running and gaseous-path Mach lines, respectively, in the gas phase. Eq. (3.6.8), Eq. (3.6.9) and Eq. (3.6.10) represent the right-running, left-running and particle-path Mach lines in the solid phase.

Transformation of Eq. (3.6.1) into its characteristic form is found by using the eigen-directions of matrix  $\tilde{M}$  as a set of local

variable coordinates in the  $(t, x)$  planes (74, 97), the detailed mathematical steps are given in Appendix 3.

The characteristic equation along the right- and left-running Mach lines in the gas phase are,

$$K_{u_g}^I (du_g)_I + K_p^I (dp)_I + K_{u_p}^I (du_p)_I + K_\phi^I (d\phi)_I = K_{t_m}^I (dt)_I \quad (3.6.11)$$

and

$$K_{u_g}^{II} (du_g)_{II} + K_p^{II} (dp)_{II} + K_{u_p}^{II} (du_p)_{II} + K_\phi^{II} (d\phi)_{II} = K_{t_m}^{II} (dt)_{II} \quad (3.6.12)$$

The characteristic equation along the gaseous-path Mach line in the gas phase is

$$K_T^{II} (dT)_{II} + K_p^{II} (dp)_{II} + K_{u_p}^{II} (du_p)_{II} + K_\phi^{II} (d\phi)_{II} = K_{t_m}^{II} (dt)_{II} \quad (3.6.13)$$

Again, the characteristic equation along the right-running, left-running Mach lines in the solid phase are,

$$K_{u_p}^{II} (du_p)_{II} + K_\phi^{II} (d\phi)_{II} = K_{t_m}^{II} (dt)_{II} \quad (3.6.14)$$

and

$$K_{u_p}^V (du_p)_V + K_\phi^V (d\phi)_V = K_{t_m}^V (dt)_V \quad (3.6.15)$$

The characteristic equation along the particle-path Mach line in the solid phase is either

Time Period 1:

$$K_{T_{P_3}}^x (dT_{P_3})_{II} + K_{T_1}^x (dT)_{II} = K_{t_m}^x (dt)_{II} \quad (3.6.16)$$

or

Time Period 2:

$$K_{T_{P_2}}^x (dT_{P_2})_{II} + K_{T_2}^x (dT)_{II} = K_{t_m}^x (dt)_{II} \quad (3.6.17)$$

The coefficients before each term are denoted by  $K_y^x$ , the superscript  $x$  is the number of the characteristic equation and  $y$  the subscript designates the coefficient. They will be shown in Appendix 3.

The characteristic equations (3.6.11) - (3.6.17) are the additional information which is needed to relate the flow properties on the boundary of interest. They are used together with the governing equations to solve the left boundary. More discussion concerning the usage of these characteristic equations will be given in the numerical solution sections later.

### 3.7 Initial and Boundary Conditions

The system of governing equations, after the above simplifications, becomes a set of six first order, coupled, non-linear, inhomogeneous partial differential equations. It is found in the study that the eigenvalues of the system are six distinct real numbers under non-fluidized conditions, (See Appendix 3). The characteristic directions are described by:

$$\left(\frac{dx}{dt}\right)_I = U_g + C_g, \quad \left(\frac{dx}{dt}\right)_{II} = U_g - C_g, \quad \left(\frac{dx}{dt}\right)_{III} = U_g \quad (3.7.1)$$

$$\left(\frac{dx}{dt}\right)_{IV} = U_p + C, \quad \left(\frac{dx}{dt}\right)_V = U_p - C, \quad \left(\frac{dx}{dt}\right)_{VI} = U_p \quad (3.7.2)$$

The subscripts I, II and III represent the right-running, left-running, and gaseous-path characteristic lines in the gas phase. The subscripts IV, V and VI represent the right-running, left-running and particle-path characteristic lines in the solid phase.

When the granular bed becomes fluidized, the speed of sound is not transmitted through the dispersed particles; therefore,  $c$  is equal to zero. However, the speed of sound in the gas phase is never zero; hence, Eq. (3.7.1) remains the same but Eq. (3.7.2) changes to:

$$\left(\frac{dx}{dt}\right)_{IV} = \left(\frac{dx}{dt}\right)_V = \left(\frac{dx}{dt}\right)_{VI} = U_p \quad (3.7.3)$$

when  $\phi > \phi_c$ . Due to this reduction of six characteristic lines into four characteristic lines when the granular bed changes from non-

fluidized to fluidized conditions, the governing equations are not totally hyperbolic. The solution of these equations become quite complicated. The boundary conditions must be well specified.

The total number of boundary conditions required depends upon the flow conditions at the igniter end of the granular bed. (As far as the current calculation is concerned, the chamber is sealed by the shear disc at the downstream end; the phenomena after the rupture of the shear disc are beyond the scope of this study.) To specify conditions at the igniter end, a separate control volume (Fig. 3) is considered, which is located immediately at the entrance of the granular bed. When this entrance control volume contains both gas and particles, six ordinary differential equations are used together with the necessary compatibility relations to determine the average flow properties in the entrance volume and also the properties at the boundary between the entrance volume and the granular bed. The compatibility relations are derived directly by transforming the governing equations into their characteristic forms (Appendix 3). When the entrance section contains gas only, three ordinary differential equations describing the time rate of change of flow properties of the gas phase are solved together with the appropriate compatibility relations for the boundary parameters needed. The total number of compatibility relations used in the calculation depends upon the flow directions of the gases and particles at the boundary and also the fluidization conditions. The boundary conditions at the shear disc end are relatively simple; before the shear disc is ruptured, the gas and particle velocities are all zero.

The initial conditions required to solve the system of equations are the initial distributions of gas temperature, pressure, velocity, particle velocity, propellant surface temperature and fractional porosity. The initial distributions of the above parameters can be non-uniform.

### 3.8 Empirical Correlations

In addition to the above governing equations, the equations of state for gas- and particle-phases must be specified. The co-volume effect becomes important at high pressures, so the Noble-Abel dense gas law also called the Clausius Equation (15),

$$P\left(\frac{1}{p} - b\right) = RT \quad (3.8.1)$$

is used as the equation of state for the gas phase. The statement of a constant density for the solid-propellant particles serves as the equation of state for the particles.

To complete the theoretical model it is necessary to specify several empirical correlations: the intergranular stress transmitted through the packed granular particles, the flow resistance due to the drag force between particle and gas phases, the convective heat transfer coefficient and the regression rates of the solid propellant particles.

#### A Constitutive Law for the Total Stress

The constitutive law used for the total stress calculations is:

$$\tau_p = \begin{cases} -\frac{P_e c^2}{g(1-\phi)} \frac{\phi}{\phi_c} (\phi_c - \phi) - P \frac{(1-\phi)}{(1-\phi)} & \text{if } \phi \leq \phi_c \\ -P & \text{if } \phi > \phi_c \end{cases} \quad (3.8.2)$$

where  $\phi_c$  is the critical porosity above which there is no direct contact between particles, and  $c$  is the speed of sound transmitted in

granular material.

$\tau_p$  actually consists of two parts (i)  $P$ , the hydrostatic pressure (ii) the normal stress due to the intergranular normal stress. In the solid phase,  $P$  is not defined inside the particles, i.e.  $P = 0$  and if particles were liquid droplets,  $P$  is defined.

The relationships of the speed of sound in the particle phase,  $c$ , and the stress tensor  $\tau_p$  are given in Appendix 6.

### B Drag Correlation

From the fluidization condition of the gas-particle system in the granular bed, the bed can be divided into a non-fluidized (packed) region and a fluidized (dispersed) region.

Due to the importance of the drag force term in the momentum equations, an extensive survey was conducted to select the most suitable drag correlation for the model. Ergun's equation (45) has been widely adopted by some pioneer investigations such as Kuo(1), Krier (5), Gough and Zwarts (3) in their studies. Since Ergun's equation is valid only for  $1 < \frac{Re_p}{(1-\phi)} < 4,000$  and  $0.4 < \phi < 0.65$ , it has very limited application to the combustion of granular propellants under high convective burning situations. A series of cold-flow resistance measurements were made by using a cylindrical chamber of the same inner diameter as the combustion chamber and the same type of propellant, but under non-fluidized, non-combustion conditions. The correlation (76) obtained is

$$D_v = \frac{\mu(u_g - u_p)(1-\phi)}{12 r_p \phi g} \left\{ 276.23 + 5.05 \frac{Re_p^{0.57}}{(1-\phi)^{0.57}} \right\} \quad (3.8.3)$$

which is valid for  $1 < \frac{Re_p}{(1-\phi)} < 24,000$ .

For the fluidized region, the expression for  $D_v$  is deduced from Andersson's expression (56) which is valid for porosities ranging from 0.45 to 1.0 and  $Re_p$  from 0.003 to 2,000. We have

$$D_v = \frac{\rho(u_g - u_p)|u_p - u_g|}{6g} \left[ 36Zt_r \frac{(1-\phi)}{Re_p} + 6C_i t_r \right] \quad (3.8.4)$$

where the tortuosity factor,  $t_r$ , is

$$t_r = \begin{cases} 1.71 \frac{(1-\phi)^{0.45}}{\phi} & \text{for } 0.45 \leq \phi \leq 0.94 \\ \phi^{-2} & \text{for } 0.92 < \phi \leq 1 \end{cases} \quad (3.8.5)$$

The cross-section factor  $Z$  and inertial drag coefficient  $C_i$  are given by

$$Z = \frac{1}{2t_r(1-\phi)\phi^{1.59}} \quad (3.8.6)$$

$$C_i = \frac{2.5}{t_r^3 [Re_p / (t_r \phi^{1.59})]^{1/2}} \left( \frac{1-\phi}{\phi} \right)^{0.45} \quad (3.8.7)$$

Although the Reynolds number range is not wide enough to cover the variation in the overall transient process, it is the best correlation available in the literature. Since the values of  $D_v$  in the fluidized region are substantially smaller than those of the nonfluidized conditions, any inaccuracy introduced by extrapolating the drag correlation for a fluidized bed to a higher Reynolds number will

not significantly influence the calculated results. The drag correlation for the nonfluidized region, however, is very important in the momentum equations.

### C Heat Transfer Correlations

For convective heat transfer calculations, Denton's formula (57) is used for the non-fluidized region, hence

$$h_c = 0.65 \frac{k}{r_p} \left[ \frac{\rho U_g - U_p}{\mu} \phi r_p \right]^{0.7} P_r^{1/3} \quad (3.8.8)$$

It is valid for  $Re_p$  from 500 to 50,000 and porosity around 0.37. Although the porosity range is very narrow for this correlation, it represents the porosity of most of the packed, unburned portion of the granular bed in combustion experiments. For fluidized regions,  $h_c$  is obtained from Rowe-Claxton's correlation (58),

$$h_c = \frac{k}{r_p} \left[ \frac{1}{1 - (\phi)^3} + \frac{0.55}{\phi} P_r^{1/3} Re_p^m \right] \quad (3.8.9)$$

where the exponent of the Reynolds number is expressed as

$$m = \frac{0.6567 + 1.55 Re_p^{-0.25}}{4.65 Re_p^{-0.25} + 1} \quad (3.8.10)$$

The Rowe-Claxton correlation is valid for  $10 < Re_p < 10^7$ .

Besides the convective heat transfer, the radiative heat conduction is represented by

$$h_{rad} = \epsilon_p \sigma [T(t) + T_{ps}(t)][T^2(t) + T_{ps}^2(t)] \quad (3.8.11)$$

where  $\epsilon_p$  is the emissivity factor is taken as unity and  $\sigma$  is the Stefan-Boltzman constant. Therefore, the total heat transfer is given by

$$h_t(t) = h_c(t) + h_{rad}(t) \quad (3.8.12)$$

and is given previously in the long form by equation (3.3.13)

$$h_t(t) = h_c(t) + \epsilon_p \sigma [T(t) + T_{ps}(t)] [T^2(t) + T_{ps}^2(t)] \quad (3.8.13)$$

#### D Burning Rate Law

The last empirical correlation needed to close this problem is the burning rate calculation. Since the relative velocity between gas and solid phase is very high in some regions, the erosive burning effect must be considered. The widely used Lenoir-Robillard (77) semi-empirical burning rate law is adopted here

$$r_b = aP^n + K_e h_c \exp\left(\frac{-\beta r_b P_p}{\rho |u_g - u_p|}\right) \quad (3.8.14)$$

where  $h_c$ , the local zero-blowing convective obtained from either Eq. (3.8.8) or Eq. (3.8.9), depending upon the fluidized situation. The erosive-burning constant,  $K_e$ , and the erosive-burning exponent,  $\beta$ , used in this investigation are listed in Table 1.

TABLE 1

DATA USED IN THE NUMERICAL COMPUTATIONS\*

$\rho_p$	= 1.6 gm/cm <sup>3</sup>
$\alpha_p$	= 0.945 x 10 <sup>-3</sup> cm <sup>2</sup> /sec
$k_p$	= 5.30 x 10 <sup>-4</sup> cal/cm-sec-°K
$k$	= 0.265 x 10 <sup>-3</sup> cal/cm-sec-°K
$\mu$	= 0.44615 x 10 <sup>-3</sup> gm/cm-sec
$b$	= 1.26 cm <sup>3</sup> /gm
$\gamma(500^\circ\text{K})$	= 1.4
$\gamma(3000^\circ\text{K})$	= 1.26
$P_T$	= 0.7
$r_{p_0}$	= 0.41275 x 10 <sup>-1</sup> cm
$\phi_c$	= 0.3995
$A$	= 0.4745 cm <sup>2</sup>
$C_L$	= 15.24 cm
$T_0$	= 293.91°K
$P_0$	= 1033.23 g/cm <sup>2</sup>
$\phi_0$	= 0.3995
$K_e$	= 0.1 cm <sup>3</sup> -°K/cal
$B$	= 105.
$\epsilon_p$	= 1.0
$\theta$	= 0.65

\*Data for propellant properties are obtained from Ballistic Research Laboratories of U.S. Army.

$$\begin{aligned}
T_{abl} &= 560^{\circ}\text{K} \\
T_{ign} &= 630^{\circ}\text{K} \\
T_{hg} &= 2500^{\circ}\text{K} \\
T_f &= 631^{\circ}\text{K} \\
C_d(\tau_{p_0}) &= 0.1969 \\
r_p(\text{undstarred}) &= 0.032945 \text{ cm} \\
a_{00} &= 0.562 \times 10^{-4} \\
&\quad (\text{cm/sec}) / (\text{g/cm}^2)^{.8367} \\
a_{30} &= 0.2814 \times 10^{-4} \\
&\quad (\text{cm/sec}) / (\text{g/cm}^2)^{.802} \\
C_{d_{00}} &= 0. \\
C_{d_{30}} &= 0.30 \\
n_{00} &= 0.8867 \\
n_{30} &= 0.8020
\end{aligned}$$

$a$  and  $n$  are linearly interpolated from  $a_{00}$ ,  $a_{30}$  and  $n_{00}$ ,  $n_{30}$  according to the values of  $C_d$  at the instantaneous surface of the grain.

### 3.9 Ignition Criterion

In the present study, the mathematical formulations governing the flow phenomena in the granular bed have already been a complicated problem. It will be helpful to have a simple ignition criterion in completing the mathematical model.

In this study, two critical temperatures were specified at the spherical pellet surfaces to achieve the ignition criterion. The lower critical value corresponds to the ablation temperature, while the higher one represents the ignition temperature of the propellant. The burning rate starts from zero as soon as particle temperature reaches the ablation temperature and increases rapidly to the burning rate value when full ignition is reached. The convective heat transfer drops to zero in a linear manner as the particle temperature increases from the ablation to the ignition temperature. Theoretically, these two critical temperatures should be dependent on pressure, but this relationship requires further study. Thus, for the purpose of this study (since pressure dependence at high pressure is small), they could be taken as constants in this study.

## CHAPTER IV

### NUMERICAL SOLUTION TECHNIQUES

The previous chapter has provided the physical background, basic assumptions, governing equations and some associated empirical correlations for this two-phase, reacting flow model. In this chapter we address the method to determine the solutions of the governing equations. The complexity of the system of governing equations make it impossible to obtain analytical solutions for the system. As a result, we turn to numerical methods for their solutions.

After some careful considerations, the explicit finite-difference scheme is employed in the interior. Method of characteristics together with some compatibility relations are used to solve the boundary points. To assure the convergence of the numerical solutions, several convergence tests have been made and proved to be very satisfactory. Due to the steep gradients in some flow properties resulting from the rapid transient combustion of the propellants, numerical instability is encountered when the straight forward two-step Richtmyer scheme is adopted. The modified version of the two-step Richtmyer scheme with a small amount of explicit artificial viscosity are introduced into the computations. Several stability criteria, such as the Courant-Friedricks-Lewy (C.F.L.) conditions (69), Energy Method (70), the von Neumann stability criteria (71), and the Heuristic Stability Theory (66) are applied on the finite-difference equations. In closing this chapter the computation procedures and the flexibility of the computer program are discussed.

#### 4.1 Selection of Numerical Methods

In order to solve the set of governing equations given in Chapter III, several different approaches may be taken. They are the method of characteristics (74), the various implicit (70) and explicit finite-difference method (71), analog simulation (79), and some others.

The method of characteristics is supposedly the most suitable method to solve a system of hyperbolic equations. Kitchens (11) has used this method (with some success) to solve the set of governing equations Kuo (1) developed. This approach has been known for its extreme accuracy but involves complicating and lengthy programming logic. An undue number of iterations are required to locate the intersections of the characteristic lines and an enormous amount of interpolations and extrapolations are involved in obtaining the flow properties at desirable locations. All these computations are time consuming and leading to inaccuracies. Due to the above reasons the method of characteristics was adopted at the boundaries only.

Implicit methods have no restriction on the domain of dependence in the time-space field. This method allows large time steps in computation, but, since the flow properties change too drastically between each node, this method was not applicable to our studies. Street (20) used implicit methods in treating some unsteady flow calculations but Abbott (81) found that these methods violated the "law of forbidden signals" inherent to system of hyperbolic equations.

Now we have narrowed down the field of possible techniques to that of an explicit scheme. Its simplicity and applicability for

digital computers renders its use advantageous. However, one inherent disadvantage is its instability. One may overcome this by special treatment of the non-linear and inhomogeneous terms.

In this technique, the partial derivatives of the dependent variables are approximated by difference equations. The system of partial differential equations is thus transformed into a set of algebraic equations. Different investigators use different methods to represent the partial derivatives, thereby arriving at different numerical results. In order to choose which finite-differencing scheme to follow, one has to notice two important criteria, namely, the convergence and the stability of the method.

Besides hundreds of reports and papers, detailed discussion on finite difference methods is contained in textbooks by Forsythe and Wessel (82), Smith (83), Roache (71), Vichnevatsky (74), and Richtmyer & Morton (70). Moretti (80, 84, 85, 86) has also done extensive work on this topic. He makes a clear distinction in the treatment of boundary and interior points and suggests that the method of characteristics be used at the boundary (exclusive of the method employed for the interior). Instability may be generated if the boundary has not been properly treated and will cause problems in the interior too.

Numerous investigators have done similar research to this present study, they are East and McClure(4); Fisher and Graves(2); Gough and Zwarts(3); Gough (12); Krier, Van Tassel, Rajan and Varshni(5); Kitchens (11); and Kuo, Vichnevatsky and Summerfield(8). They all used a slightly different numerical scheme to solve their governing equations.

Based on the valuable experience of researchers in the field of granular propellant combustion we have made our choice of numerical schemes.

The method of characteristics together with some compatibility relations have been adopted in the boundary calculations. An explicit method for the interior has been used, namely the modified two-step Richtmyer scheme incorporated with predictor-corrector calculations. In using the predictor-corrector technique, the non-linear terms are treated in an explicit manner. This combination of the method of characteristics and finite difference equations has been shown to be very efficient in the present system of partial differential equations.

#### 4.2 The Finite-Difference Equations for the Interior Points

For interior points the modified two-step Richtmyer scheme was used with predictor-corrector calculations. By the two-step modified Richtmyer scheme we mean a scheme in which the diffusing scheme (87) and the modified Leap-Frog scheme (22) are used for alternate time cycles in the following manner.

In general, the system of differential equations are represented by

$$\frac{\partial u}{\partial t} + A \frac{\partial u}{\partial x} = \tilde{I} \quad (4.2.1)$$

where  $u$  is a vector whose components,  $m$  in number, are the dependant variables and  $A$  in this case is an  $n$  by  $m$  matrix. To simplify the notation,  $A$  is considered to be a constant matrix. The system is hyperbolic if  $A$  has all real eigenvalues and  $m$  linearly independent eigenvectors. In this study  $A$  was found to consist of all real eigenvalues, so we concluded that our system of equations was of hyperbolic type.  $\tilde{I}$  represents the inhomogeneous terms appearing in the system of equations. The finite difference diffusing scheme using central differences in space and forward differences in time is employed for the first-step calculations. The difference algorithm for the predictor and corrector calculations is given below.

The following notation was used: if  $u(x, t)$  is any function of one space variable and time,  $u_{i,j}^j$  denotes the finite-difference approximation to  $u$  ( $i \Delta x, j \Delta t$ ), where  $\Delta x$  and  $\Delta t$  are the dimensions of the unit mesh in the  $x, t$  plane and  $i$  and  $j$  have integer values.

The first-step diffusing scheme becomes,

Predictor:

$$\left. \begin{aligned} \frac{\partial u}{\partial t} &= \frac{[u_i^{j+1} - 0.5(u_{i+1}^j + u_{i-1}^j)]}{\Delta t} \\ \frac{\partial u}{\partial x} &= \frac{(u_{i+1}^j - u_{i-1}^j)}{2\Delta x} \end{aligned} \right\} \quad (4.2.2)$$

Corrector:

$$\left. \begin{aligned} \frac{\partial u}{\partial t} &= \frac{[u_i^{j+1} - 0.5(u_{i+1}^j + u_{i-1}^j)]}{\Delta t} \\ \frac{\partial u}{\partial x} &= \frac{[(1-\theta)(u_{i+1}^j - u_{i-1}^j) + \theta(u_{i+1}^{j+1} - u_{i-1}^{j+1})]}{2\Delta x} \end{aligned} \right\} \quad (4.2.3)$$

The non-linear coefficients and inhomogeneous terms were treated explicitly in the predictor-corrector technique.

Using Eqs. (4.2.2) and (4.2.3), Eq. (4.2.1) is expressed in another form as follows,

$$\begin{aligned} u_i^{j+1} &= \frac{1}{2}(u_{i+1}^j + u_{i-1}^j) - \frac{\Delta t}{2\Delta x} A(u_{i+1}^j - u_{i-1}^j) \\ &\quad + \Delta t I_i^j \end{aligned} \quad (4.2.4)$$

$$\begin{aligned} u_i^{j+1} &= \frac{1}{2}(u_{i+1}^j + u_{i-1}^j) - \frac{\Delta t}{2\Delta x} A[(1-\theta)(u_{i+1}^j - u_{i-1}^j) \\ &\quad + \theta(u_{i+1}^{j+1} - u_{i-1}^{j+1})] + \Delta t [(1-\theta)I_i^j + \theta I_i^{j+1}] \end{aligned} \quad (4.2.5)$$

Eqs. (4.2.4) and (4.2.5) are explicitly defined, since each equation determines one unknown in terms of old quantities alone.  $u_i^{j+1}$  represents the predicted quantity from the latest iteration of the predictor calculations. When  $\theta = 0$ , Eq. (4.2.4) reduces to the original diffusing scheme (which has second order accuracy). The

modified Leap-Frog scheme using central differences in both space and time is employed for the second-step calculations. The Crank-Nicolson parameter (73)  $\theta$ , which lies between 0 and 1, is used to help stabilize the numerical solution. The difference algorithm for the second-step in the predictor and corrector calculations is given below.

Predictor:

$$\left. \begin{aligned} \frac{\partial u}{\partial t} &= \frac{(u_i^{j+2^a} - u_i^j)}{2\Delta t} \\ \frac{\partial u}{\partial x} &= \frac{(u_{i+1}^{j+1} - u_{i-1}^{j+1})}{2\Delta x} \end{aligned} \right\} \quad (4.2.6)$$

Corrector:

$$\left. \begin{aligned} \frac{\partial u}{\partial t} &= \frac{(u_i^{j+2^a} - u_i^j)}{2\Delta t} \\ \frac{\partial u}{\partial x} &= \frac{[(1-\theta)(u_{i+1}^j - u_{i-1}^j) + \theta(u_{i+1}^{j+2^a} - u_{i-1}^{j+2^a}) + (u_{i+1}^{j+1} - u_{i-1}^{j+1})]}{4\Delta x} \end{aligned} \right\} \quad (4.2.7)$$

Using Eqs. (4.2.5) and (4.2.7), Eq. (4.2.1) can be expressed in the following form,

$$-u_i^{j+2^a} = u_i^j - \frac{\Delta t}{\Delta x} A (u_{i+1}^{j+1} - u_{i-1}^{j+1}) + 2\Delta t I_i^{j+1} \quad (4.2.8)$$

$$\begin{aligned} -u_i^{j+2^a} &= u_i^j - \frac{\Delta t}{2\Delta x} A [(1-\theta)(u_{i+1}^j - u_{i-1}^j) \\ &\quad + \theta(u_{i+1}^{j+2^a} - u_{i-1}^{j+2^a}) + (u_{i+1}^{j+1} - u_{i-1}^{j+1})] \\ &\quad + \Delta t [(1-\theta)I_i^j + \theta I_i^{j+2^a} + I_i^j] \end{aligned} \quad (4.2.9)$$

Again, Eqs. (4.2.8) and (4.2.9) are expressed explicitly. A set of conservation of mass equations in the gas phase are implemented in the finite-difference form using the above mentioned numerical scheme and are shown in Appendix 3.

The above predictor-corrector technique has been used to overcome the nonlinearity of these partial derivatives and the inhomogeneous terms. In the predictor calculations, the previous time quantities are used to evaluate the coefficients of the spatial derivatives and inhomogeneous terms. The solutions determined from these calculations are averaged, according to  $\theta$ , with the previous time quantities. These averaged values are used in calculating the non-linear coefficients and inhomogeneous terms in the corrector calculations.

This conventional predictor-corrector technique, caused numerical instabilities in both the interior nodes and the boundaries. As a result, a small amount of artificial viscosity (88) was introduced in the calculation to filter out the high frequency components. This was done only in the 2 second-step calculations, since the first-step calculations are rather stable.

Following the implementation of this two step numerical scheme with predictor-corrector techniques and an artificial viscosity in the second step, a significant improvement of stability has been achieved; the predictors and correctors are very close numerically.

#### 4.3 Numerical Treatment of the Boundary Conditions

The boundary points are calculated by using physical and compatibility relations to achieve a high degree of numerical stability. The compatibility relations used can also be regarded as the extraneous boundary conditions(1) which are needed when the central difference technique is used for space derivatives in the hyperbolic partial differential equations. In this study, these additional boundary conditions are a set of characteristic equations derived earlier in Chapter III.

The total number of boundary conditions on the left end of the chamber depends on the number of physical boundary conditions plus the extraneous boundary conditions available. The number of compatibility characteristics equations used depends on the flow directions of the gas and particles and the fluidization conditions at the boundary. Eight sets of left boundary conditions have been considered in this study. The right boundary conditions are simple, the gas and particle velocities are zero before the shear disc breaks. It is necessary to determine how the characteristic equations worked on a t-x diagram before showing the difference approximations that apply along the characteristic line.

When both  $u_g(x_L, t)$  and  $u_p(x_L, t)$  are subsonic, and are flowing in the positive direction and the bed is non-fluidized, (LBC<sub>1</sub>) i.e. Left Boundary Condition - Case 1, the Mach lines at the boundaries are shown in Fig. 4. In this case there are two left-running Mach lines, II and V, sent out from  $A_1$  and  $A_2$  passing through point B at the left boundary. The II characteristic equation with a slope  $(\frac{dx}{dt})_{II} = u_g - c_g$  and the V characteristic equation with a slope  $(\frac{dx}{dt})_V = u_p - c_p$ . Similarly there are four characteristic lines passing through point B'



at the right boundary. They are, characteristics lines I, III, IV and VI, which have slopes  $(\frac{dx}{dt})_I = u_g + c_g$ ,  $(\frac{dx}{dt})_{III} = u_g$ ,  $(\frac{dx}{dt})_{IV} = u_p + c$  and  $(\frac{dx}{dt})_{VI} = u_p$  respectively.

The number of unknowns in the entrance region are six, they are  $u_{g_c}$ ,  $u_{p_c}$ ,  $\phi_c$ ,  $T_c$ ,  $P_c$  and  $T_{ps_c}$ . These unknowns are determined easily by the governing equation derived in section 3.5. With the above quantities determined, we combined them with the two compatibility relations, given by Eq. (A-3.46) and (A-3.58) and some other assumptions, the six unknowns at point B',  $u_g$ ,  $u_p$ ,  $\phi$ ,  $T$ ,  $P$  and  $T_{ps}$  are determined.

Since the entrance region is so close to the left boundary points, the following assumptions were made to facilitate the use of the two compatibility relations Eq. (A-3.46) and Eq. (A-3.58), they are

$$u_p(x_L, t) = u_{p_c}(t) \quad (4.3.1)$$

$$T_{ps}(x_L, t) = T_{ps_c}(t) \quad (4.3.2)$$

$$P(x_L, t) = P_c(t) \quad (4.3.3)$$

From characteristic equation V, Eq. (A-3.58), with the assumptions given by Eq. (4.3.1) we obtained the porosity,  $\phi$ , at point B by direct substitution.

The compatibility relation given by characteristic II is integrated along its characteristic direction to yield one additional condition,  $u_g$ . This equation is solved simultaneously with the other two physical boundary conditions Eqs. (4.3.1) and (4.3.3) and the calculated  $\phi$  at B. The first two conditions further involve two more unknowns, the chamber pressure  $P_c(t)$  and the chamber particle velocity,  $u_{p_c}(t)$ . The equations involving  $P_c(t)$  and  $u_{p_c}(t)$  are given by Eqs. (3.5.15) and (3.5.6), together with Eqs. (4.3.1), (4.3.2) and (4.3.3) form a closed system.

The characteristic equation II can be solved simultaneously with the other equations by direct substitutions. Numerical oscillations are observed when the coefficients of the differential terms are evaluated at  $A_2$  (Fig. 4). In order to overcome the numerical oscillations in the boundary calculations, the sophisticated fourth order Runge-Kutta integration method (RK4) was employed (89) to carry out the integration along the left-running characteristics. In order to perform the RK4, characteristic equation II is reconstructed to form an ordinary differential equation in the following manner,

$$(du_g)_x = [-K_p^x(dp)_x - K_{u_p}^x(du_p)_x - K_\phi^x(d\phi)_x + K_{cm}^x \Delta t] / (K_{u_g}^x) \quad (4.3.4)$$

The pressure difference, particle velocity difference, porosity difference, at the right hand side of Eq. (4.3.4) are the properties at B and the linearly interpolated quantities at  $A_2$ . After the fourth-order Runge-Kutta integration is performed, the gas velocity at the left boundary becomes

$$u_{g_{x_L}}^{j+1} = u_{A_2}^j + \frac{1}{5} (T_1 + 2T_2 + 2T_3 + T_4) \quad (4.3.5)$$

where the coefficients  $T_1$ ,  $T_2$ ,  $T_3$ , and  $T_4$  are calculated from

$$T_1 = (-K_p^{\frac{x}{A_2}} (dP)_x - K_{u_p}^{\frac{x}{A_2}} (du_p)_x - K_{\phi}^{\frac{x}{A_2}} (d\phi)_x + K_{c_m}^{\frac{x}{A_2}} \Delta t) / (K_{u_g}^{\frac{x}{A_2}})$$

$$T_2 = (-K_p^{\frac{x}{M_2}} (dP)_x - K_{u_p}^{\frac{x}{M_2}} (du_p)_x - K_{\phi}^{\frac{x}{M_2}} (d\phi)_x + K_{c_m}^{\frac{x}{M_2}} \Delta t) / (K_{u_g}^{\frac{x}{M_2}})$$

$$T_3 = (-K_p^{\frac{x}{M_2}} (dP)_x - K_{u_p}^{\frac{x}{M_2}} (du_p)_x - K_{\phi}^{\frac{x}{M_2}} (d\phi)_x + K_{c_m}^{\frac{x}{M_2}} \Delta t) / (K_{u_g}^{\frac{x}{M_2}}) \quad (4.3.6)$$

for Predictor steps,

$$T_4 = (-K_p^{\frac{x}{A_2}} (dP)_x - K_{u_p}^{\frac{x}{A_2}} (du_p)_x - K_{\phi}^{\frac{x}{A_2}} (d\phi)_x + K_{c_m}^{\frac{x}{A_2}} \Delta t) / (K_{u_g}^{\frac{x}{A_2}})$$

for Corrector steps,

$$T_4 = (-K_p^{\frac{x}{B}} (dP)_x - K_{u_p}^{\frac{x}{B}} (du_p)_x - K_{\phi}^{\frac{x}{B}} (d\phi)_x + K_{c_m}^{\frac{x}{B}} \Delta t) / (K_{u_g}^{\frac{x}{B}})$$

Temperature of the gas,  $T$ , is found by using the gas static temperature at  $x_L$ ,

$$T_{x_L}^{j+1} = T_c^{j+1} + \frac{(u_{g_{x_L}}^{j+1})^2 - u_{g_{x_L}}^{j+1}}{2gJc_p} \quad (4.3.7)$$

Once the boundary values at B have been determined, the new location of  $A_2$  at the next time level is calculated from the slope of the left-running characteristic line at the current time, i.e.

$$X_{A_2}^{j+1} = \frac{\Delta t}{2} (-u_{g_{xL}}^{j+1} + C_{g_{xL}}^{j+1} - u_{g_{A_2}}^j + C_{g_{A_2}}^j) + x_L \quad (4.3.8)$$

Similarly, the location of  $A_3$  is given by,

$$X_{A_3}^{j+1} = \frac{\Delta t}{2} (-u_{p_{xL}}^{j+1} + C_{xL}^{j+1} - u_{p_{A_3}}^j + C_{A_3}^j) + x_L \quad (4.3.9)$$

The positions of  $A_2$  and  $A_3$  vary slightly with respect to time, so the locations of  $A_2$  and  $A_3$  are not involved in the iteration procedures. The above calculations are shown in a flow chart in Fig. 6.

The treatment of the right boundary conditions is simpler, since no right control volume is considered. In general we only have six unknowns to solve, namely  $u_g$ ,  $u_p$ ,  $T$ ,  $\phi$ ,  $P$  and  $T_{ps}$ . Before the stainless-steel diaphragm breaks, the right end of the combustion chamber is closed, the gas velocity  $u_g$  and particle velocity,  $u_p$ , are always equal to zero, these conditions are given by

$$u_g(X_R, t) = 0 \quad (4.3.10)$$

$$u_p(X_R, t) = 0 \quad (4.3.11)$$

The other four unknowns are found by the four characteristics, I, III, IV and V. Since the gas velocity is very small in the neighborhood of the shear disc, the solution is quite stable. To reduce the amount

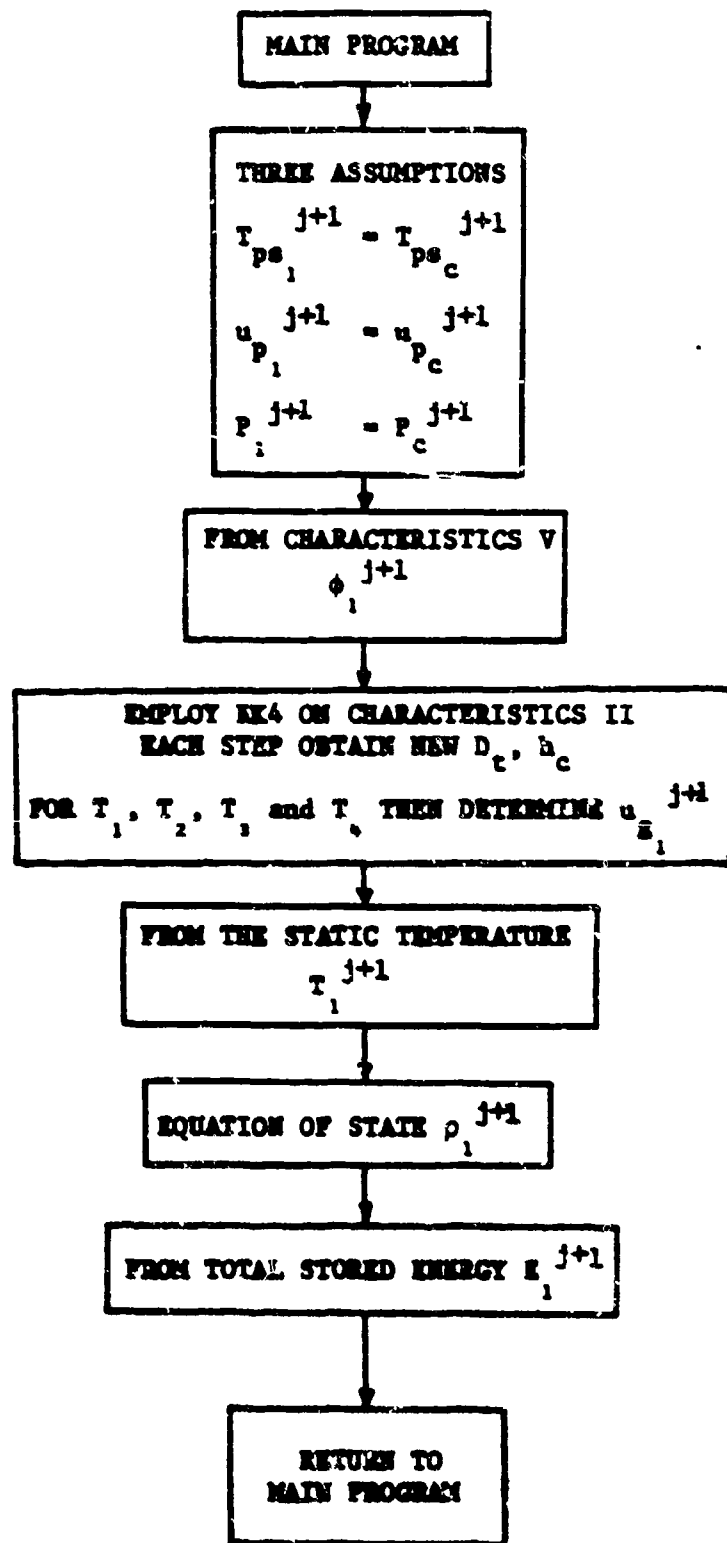


Figure 6: Flow Chart for Left Boundary Condition-Case 1

of computations, RK4 integration method is not employed here. To obtain the porosity,  $\phi$ , at B' we directly substitute the zero particle velocity into characteristic IV, Eq. (A-3.46). Using the zero gas velocity, zero particle velocity and the calculated porosity at B', we substitute into characteristic equation I, Eq. (A-3.40), the gas pressure, P at B' is found immediately. Similarly the gas temperature, T, is obtained by substituting the calculated pressure at B' and other known quantities into characteristic equation III, Eq. (A-3.52). From characteristic equation VI, Eq. (A-3.66) the particle temperature is obtained. The above treatment involves only direct substitutions, so the right boundary values are easily obtained. The characteristic equations I, III, IV and VI are recasted as follows,

Characteristic equation I becomes

$$K_{u_g}^I (du_g)_x - K_p^I (dP)_x - K_{u_p}^I (du_p)_x - K_g^I (d\phi)_x + K_{tm}^I (dt)_x \quad (4.3.12)$$

Characteristic equation III becomes

$$K_T^III (dT)_x - K_p^III (dP)_x - K_{u_p}^III (du_p)_x - K_g^III (d\phi)_x + K_{tm}^III (dt)_x \quad (4.3.13)$$

Characteristic equation IV becomes

$$K_p^IV (dP)_x - K_{u_p}^IV (du_p)_x + K_{tm}^IV (dt)_x \quad (4.3.14)$$

Characteristic equation VI becomes

$$K_{T_p}^VI (dT_p)_x - K_T^VI (dT)_x + K_{tm}^VI (dt)_x \quad (4.3.15)$$

Eqs. (A-3.12) - (A-3.15) are coded directly into the computer program in the above manner. (See Fig. 6A.)

The locations of  $A_1$ ,  $A_3$ ,  $A_4$  and  $A_6$  for the next time level are determined from

$$X_{A_1}^{j+1} = \frac{\Delta t}{2} (u_{gXR}^{j+1} - C_{gXR}^{j+1} + u_{gA_1}^j - C_{gA_1}^j) + x_R \quad (4.3.16)$$

$$X_{A_3}^{j+1} = \frac{\Delta t}{2} (-u_{gXR}^{j+1} - u_{gA_3}^j) + x_R \quad (4.3.17)$$

$$X_{A_4}^{j+1} = \frac{\Delta t}{2} (-u_{pXR}^{j+1} - C_{pXR}^{j+1} - u_{pA_4}^j - C_{pA_4}^j) + x_R \quad (4.3.18)$$

$$X_{A_6}^{j+1} = \frac{\Delta t}{2} (-u_{pXR}^{j+1} - u_{pA_6}^j) + x_R \quad (4.3.19)$$

Since the above locations change very slightly with respect to time, they are calculated in advance from the slopes of the characteristic lines at the previous time.

When the gas velocity changes sign at the left end, the particle velocity still remains positive and the bed is non-fluidized (LBC5)(90). As shown in Fig. 5, there are three characteristic lines, emanating from  $A_2$ ,  $A_3$  and  $A_4$ , passing through the left boundary point B. The characteristic lines at the right are same as those in Fig. 4, calculations at

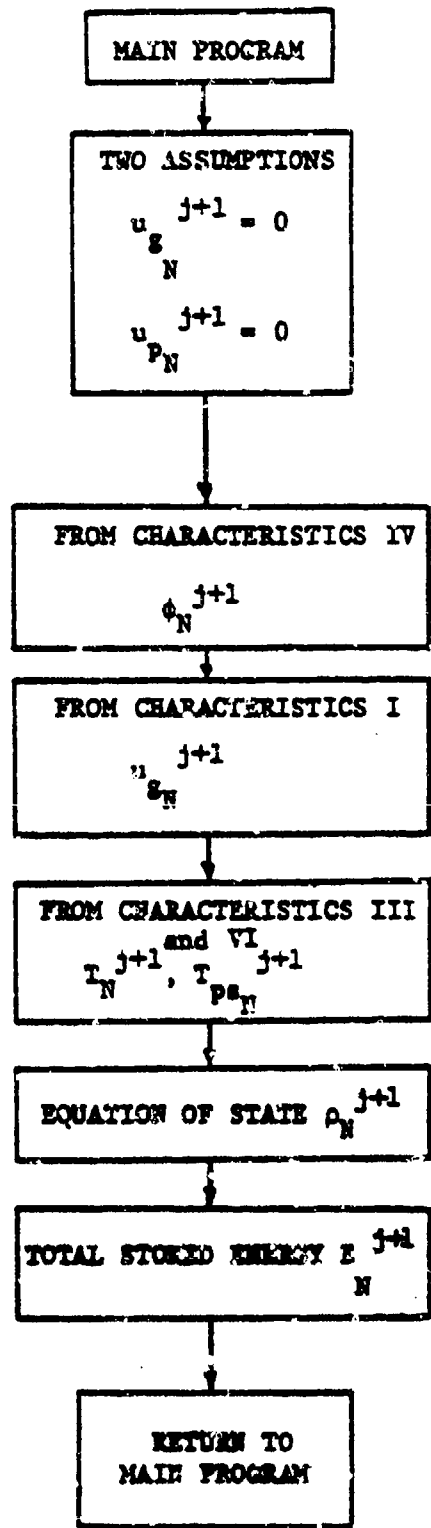


Figure 6A Flow Chart for Right Boundary Condition

B' remain the same.

As in the previous case, all the unknown quantities at the chamber are first calculated from the governing equations. Some assumptions are made to facilitate the use of the three compatibility relations, Eqs. (A-3.46), (A-3.52) and (A-3.62). They are Eqs. (4.3.1) - (4.3.3).

Porosity,  $\phi$ , at boundary point B' is obtained from characteristic V. The fourth order Runge-Kutta integration method is applied to both compatibility conditions along characteristic III and V. Gas temperature, T, is determined from characteristic III and gas velocity,  $u_g$  is from characteristic V. After all the unknowns at boundary point B' have been determined, the above calculations are shown in Fig. 7. The locations of  $A_2$  and  $A_5$  are determined using Eqs. (4.3.8) and (4.3.9) and new location of  $A_3$  is given by

$$X_{A_3}^{j+1} = \frac{\Delta t}{Z} (-u_{g_{x_L}}^{j+1} - u_{g_{A_3}}^j) + x_L \quad (4.3.20)$$

Besides the above mentioned LBC (Left Boundary Conditions), six other left boundary conditions have been considered depending on the sign of  $u_g$ ,  $u_p$  and the fluidization conditions, this is shown in Appendix 7.

The extraneous boundary values calculated in the above manner converge very quickly. Since the boundary conditions have been well treated, the amount of error propagated into the interior grids are small.

The combination of finite-difference and the method of characteristics has been shown to be an appropriate method to handle this type of hyperbolic partial differential equations.

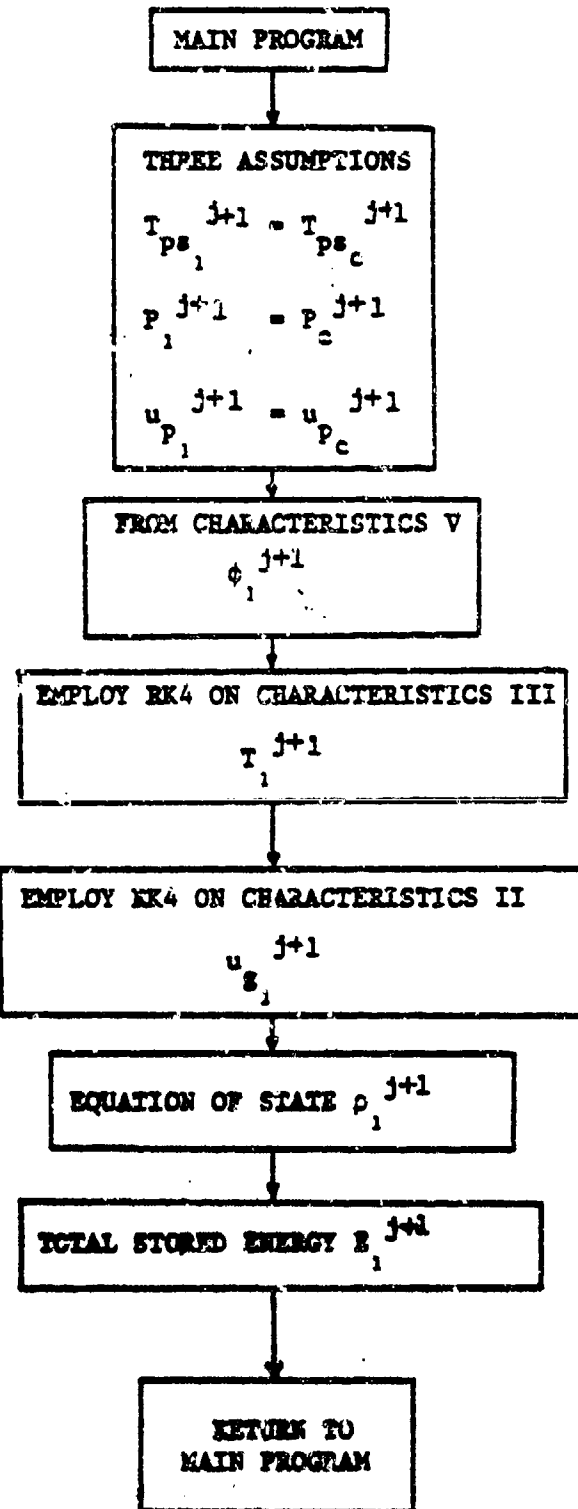


Figure 7. Flow Chart for Left Boundary Condition-Case 5

#### 4.4 Convergence Tests and Error Analysis

It is a formidable task for the formal error estimation and stability analysis on the numerical algorithm selected for our intricate system of coupled, non-linear, inhomogeneous partial differential equations. This task is compounded by the complicated boundary conditions. In order to bypass these nearby insuperable difficulties, various convergence tests are performed to verify the numerical solutions converge to the genuine solutions of the original differential equations.

The convergence tests are performed by varying the mesh sizes in time and space increments. The solutions change slightly when the mesh sizes for time and space are reduced by a factor of four. Within the present scope of this two-phase combustion problem, our numerical solutions are practically unaffected by changing the mesh sizes.

Due to the fact that convergence of the numerical solution depends on how well the problem is posed, various tests are performed on the sensitivity of the solution by changing the initial conditions, boundary conditions and some other important parameters such as the initial propellant particle size, the fractional porosity, the burning rate law, the heat transfer correlation, the drag correlation, the constitutive law of intergranular stress, the ignition criteria, the ignition mass flow rate etc. In all these tests, the numerical solutions are bounded and change only slightly for small perturbations on the parameters. The existence of the neighboring solutions is proved and the convergence of the numerical solutions is therefore assured.

#### 4.5 Stability Criteria

When the partial differential equations are represented by the finite-difference equations, high frequency components will not be treated accurately. This inaccurate treatment of the high frequency components leads to the numerical stability considerations. All finite-difference schemes possess high frequency components. If these components are damped or don't grow rapidly with time, the scheme is stable. On the other hand, if these components grow rapidly and finally dominate the calculation, the scheme is said to be unstable.

In general, the finite-difference systems cannot be assessed for instability of non-linear systems. Sometimes, the stability criteria for the non-linear case is studied as if it is a linear system.

Several different methods of stability analysis are known in this field. We selected the following methods to evaluate the stability of our numerical scheme, they are:

- A. the Courant, Friedrichs and Levy Conditions (C.F.L.) (69),
  - B. the Energy Method (70),
  - C. the von Neumann stability analysis (71),
  - D. Heuristic Stability Theory of Hirt (66).
- A. The stability condition for the two-step modified Richtmyer scheme when  $\tilde{I} = 0$  in Eq. (4.2.1) and the system of partial differential equations is hyperbolic is that the value of  $\frac{\Delta x}{\Delta t}$  should not be greater than the largest eigenvalue of  $\lambda$ . This is shown by

$$\frac{\Delta t}{\Delta x} [\max |u_g \pm c_g|] \leq 1 \quad (4.5.1)$$

where  $c_g$  is given by Eq. (A-4.13).

It should be noted that the selection of  $\Delta t$  is very critical for this stability condition. This criteria is used as a basic requirement when selecting the size of  $\Delta t$  and  $\Delta x$  in the numerical calculations.

#### B. Energy Method

This method is closely related to an energy conservation principle of the differential equation. In many cases the conserved quantity is not necessarily related to physical energy, but generally the square of the independent variable as shown in reference (70).

Two subroutines are built in the program, mainly to check the balancing of the conservation equations in both the gas and particle phase. So the corrector step for the diffusing scheme and the corrector step for the Leap Frog scheme solutions are checked. The results are highly satisfactory, since the balance of all five conservation equations are checked closely.

#### C. the von Neumann Stability Analysis

In this method, a finite Fourier series expansion of the solution to the modal equations is made. The decay or amplification of each mode is considered separately to determine the stability condition. The amplification factor,  $G$ , of the system of equation lies very nearly in the unit circle. The mathematical step for this stability analysis is shown in reference (71).

D. Hirt's Stability Analysis

A detailed study on the numerical scheme used in this two-phase combustion problem has been performed. The finite-difference equations using our present numerical scheme was applied to the conservation equations. Each term of the difference equations is expanded in a Taylor series. The lowest-order terms in the expansion must represent the original conservation equation. All the high-order terms are called truncation errors which account for the computational instabilities of the finite difference method. All the diffusion terms are collected from the truncation error terms. After following all the numerical steps we found that the effective diffusion coefficients are positive for the numerical scheme we used, thus the computational stability is assured. One typical way to obtain the effective diffusion coefficient for the numerical solutions of a partial differential equation can be found in Reference (66).

From the above four stability studies we have concluded our numerical scheme is very stable.

#### 4.6 Artificial Viscosity

The modified two-step Richtmyer scheme is believed to be stable when there is no inhomogeneous and the system of partial differential equations is hyperbolic. When inhomogeneous terms are included, instability is encountered. A similar condition was observed by Gough and Zwarts (3), Krier et al (5). Fortunately, methods are available to overcome this problem. Gough and Zwarts used a damping procedure based on the smoothing theory of Shuman (91) to circumvent this problem. Krier et al used an artificial viscosity parameter (92) which provided damping effect on the high frequency components.

To overcome our problem an artificial viscosity  $\epsilon$ , which provides damping, has been added to our scheme. This parameter is applied only to the Predictor and Corrector for the two-step Leap Frog in the following manner.

$$u_i^{j+2} = (1-2\epsilon)u_i^{j+2} + \epsilon u_{i+1}^{j+2} + \epsilon u_{i-1}^{j+2} \quad (4.6.1)$$

After this artificial viscosity has been added, the numerical solutions have no more stability problem introduced by the inhomogeneous terms. A 3.5% weighting factor ( $\epsilon = 0.035$ ) applied to the neighboring mesh points would eliminate the high frequency components effectively.

#### 4.7 Calculation Procedure and Flexibility of the Program

The theoretical model, described by a set of governing equations together with the additional relationships are shown in Chapter III. The simplified governing equations in section 3.4 are coded in a Fortran language for an IBM 370-168 Digital Computer.

A program consisting of a main routine and fifty-three subroutines, has been developed to solve this two-phase combustion problem. The overall calculation procedure is shown in the flow chart in Fig. 8. The program is basically divided into four sections:

- (a) Predictor for the first-step diffusing scheme
- (b) Corrector for the first-step diffusing scheme
- (c) Predictor for the second-step Leap Frog scheme
- (d) Corrector for the second-step Leap Frog scheme

The sequence is first to calculate the left boundary conditions, second to calculate the right boundary conditions, then to calculate the interior points. This sequence is repeated for the predictor and corrector of the two steps.

This program has been designed to be as general as possible with the following special features:

- (a) Each set of boundary conditions are coded into a separate subroutine to facilitate changes.
- (b) With small modifications, this program could handle moving boundary conditions.
- (c) All empirical correlations are coded separately and could be changed readily.
- (d) Two special subroutines are developed to check the solutions for the corrected level of both diffusing and Leap Frog schemes.

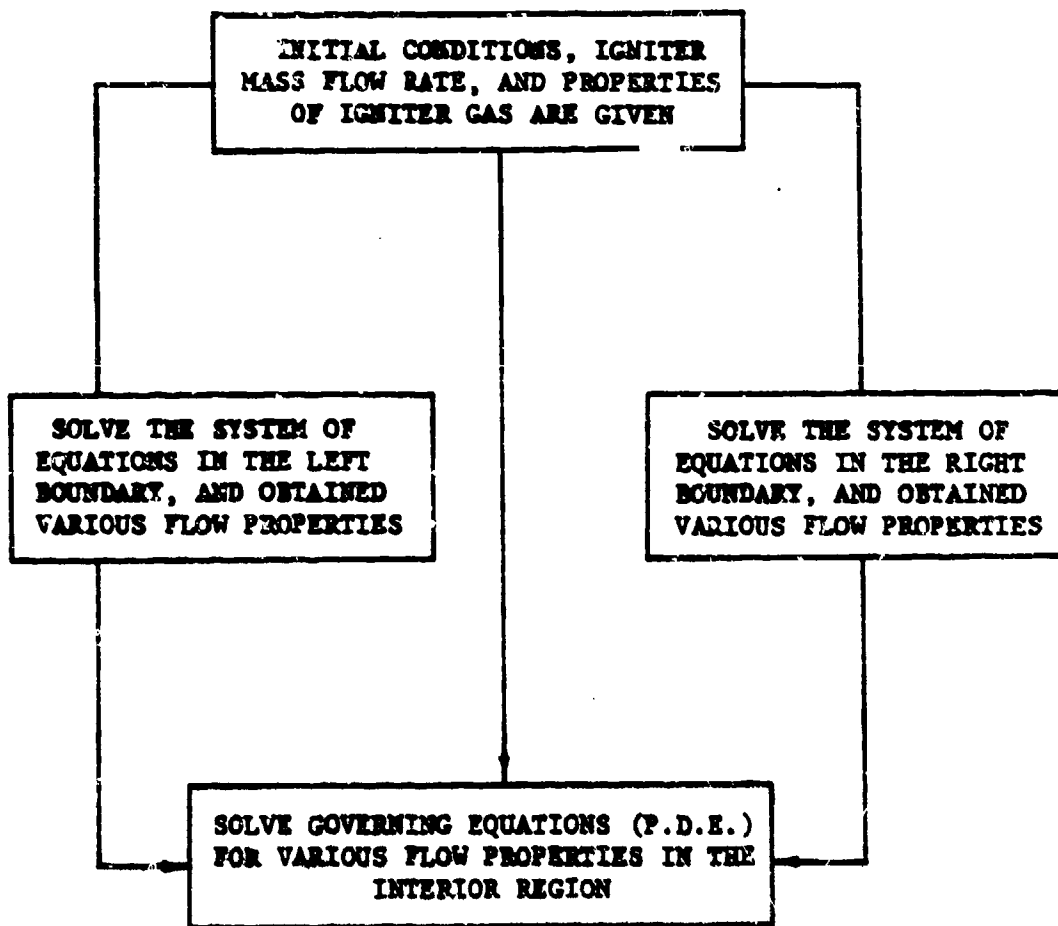


Figure 5 General Flow Chart for the Solution of Governing Equations

Thus demonstrating the convergence of the solutions by the "Energy method " (70).

- (e) To insure accuracy ,all real numbers are given in double precision.
- (f) The mesh sizes of  $\Delta x$  and  $\Delta t$  could be easily changed for obtaining information at desired axial locations and specific times.
- (g) The program is written so that the solution process could be stopped and restarted at any time in the calculation.
- (h) Common blocks are composed of functional groups of program parameters.
- (i) Meaningful nomenclature has been assigned to the variables for easy identification.
- (j) The main program contains only call statements.

## CHAPTER V

### COMPARISON OF THEORETICAL PREDICTIONS WITH EXPERIMENTAL DATA

#### 5.1 Experimental Setup

Experiments to verify the theoretical model are carried out using the cylindrical chamber shown in Fig. 1. The geometric dimensions of the chamber are given in the same figure. The spherical propellant used for the tests is type WC-870, with an average particle diameter of 0.8255 mm. Some physical parameters and chemical data of the spherical propellant is given in Table 2. The particles are packed in a chamber 15.24 cm long with 0.777 cm I.D. to form a propellant bed with an average weight of 6.95 grams. The cylindrical chamber has a wall thickness of 3.937 cm which is much thicker than the downstream stainless-steel shear disc (0.81 mm.). This 0.81 mm. burst diaphragm provides a fixed boundary and also serves as a safety valve for the chamber. Consequently, there is no permanent deformation to the combustion chamber after each test. Due to this fact, the same apparatus is used repeatedly for a series of identical tests when the loading density is kept constant.

To measure pressure and flame front speed, high frequency Minihat pressure transducers (93) and ionization probes (94) (Dynasen CA-1040) are equally spaced along the chamber. (The pressure transducers are statically calibrated by a dead weight tester at Ballistics Research Laboratories of Aberdeen Proving Ground.) They are placed at the prescribed locations marked by G1, G2, G3, G4 and G5 in Fig. 1. In order to maximize chamber strength, the transducers and ionization probes are placed spirally along the chamber.

A gaseous pyrogen ignition system is used to ignite the propellant bed, and is shown schematically in Fig. 9. This type of ignition system

TABLE 2

PHYSICAL, COMPOSITIONAL AND THERMO-CHEMICAL DATA  
OF WC 870 PROPELLANT\*

Granulation

Max Particle Diameter = 0.0965 cm  
Min Particle Diameter = 0.0686 cm

Particle Shape = Spherical

Gravimetric Density = 0.960 gm/cc

% Nitroglycerin = 10.0

% Nominal Nitrogen

Content of Nitrocellulose = 13.15

% Deterrent Coating = 5.20

Heat of Explosion = 870 cal/gm

Flame Temperature = 2831°K

\*This WC870 PROPELLANT WAS MANUFACTURED BY OLIN  
CORPORATION, WINCHESTER GROUP

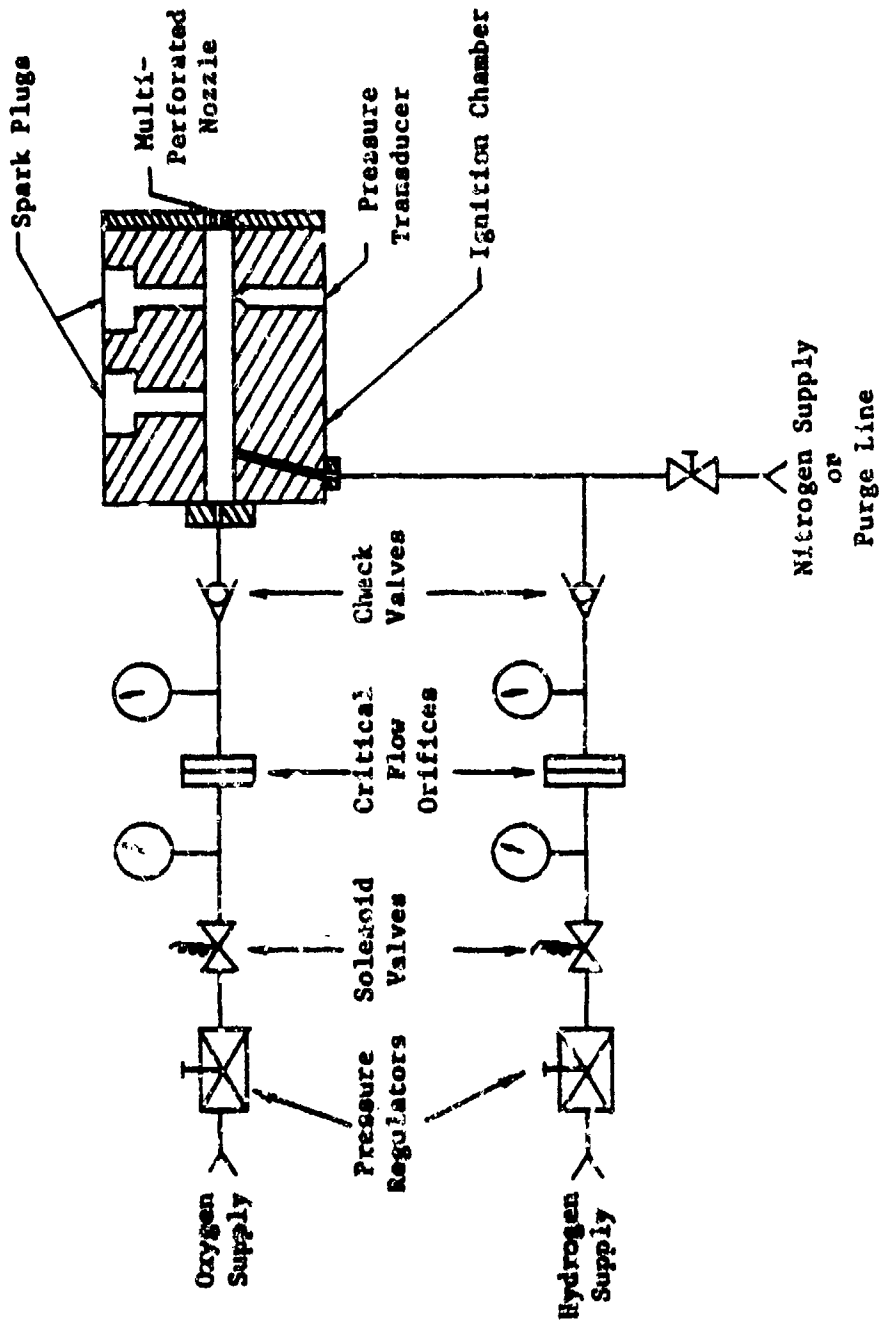


Figure 9 Schematic Drawing of Igniter Fired Line and Ignition Chamber

was chosen over the conventional impact ignition primer because it is capable of achieving both high reproducibility as well as varying igniter strength and duration. These features are not characteristic of pellet igniters (95). The length of the igniter chamber 4.763 cm and the inner diameter of the chamber is 0.777 cm.

Igniter mass flow rate is determined by the choked flow equation using ignition chamber pressure and temperature, and is shown in Fig. 10. The igniter strength and reproducibility are controlled by regulating the gaseous mixture pressure and the fuel-oxidant ratio. The reactant combination of gaseous hydrogen and oxygen was chosen for the igniter because of its wide flammability limits and because it is easily ignited by sparks.

The gaseous reactants are well-mixed in the ignition chamber and the gas feed lines are closed before ignition by spark plugs. Two spark plugs are used to insure a successful ignition in every firing.

The ignition and combustion chambers are separated by a multi-perforated convergent nozzle, which consists of seven holes of 1/16 inch I.D. For greater flow efficiency, the diameter of the holes is expanded to 3/32 inch at the interface between the nozzle and the igniter chamber, forming a parabolic entrance. A detailed description of the nozzle is shown in Fig. 11. The upstream side of the nozzle is covered and tightly sealed by a tape to prevent unburned reactant gases from entering the propellant bed before ignition. The design of the multi-perforated nozzle is intended specifically to provide a radially uniform heating of the granular propellant bed, to achieve a one-dimensional flow condition in the axial direction, and also to provide a one-dimensional composition of the bed.

The transient data obtained from pressure transducers and ionization pins are recorded in the F.M. Mode of a multi-channel tape recorder at a

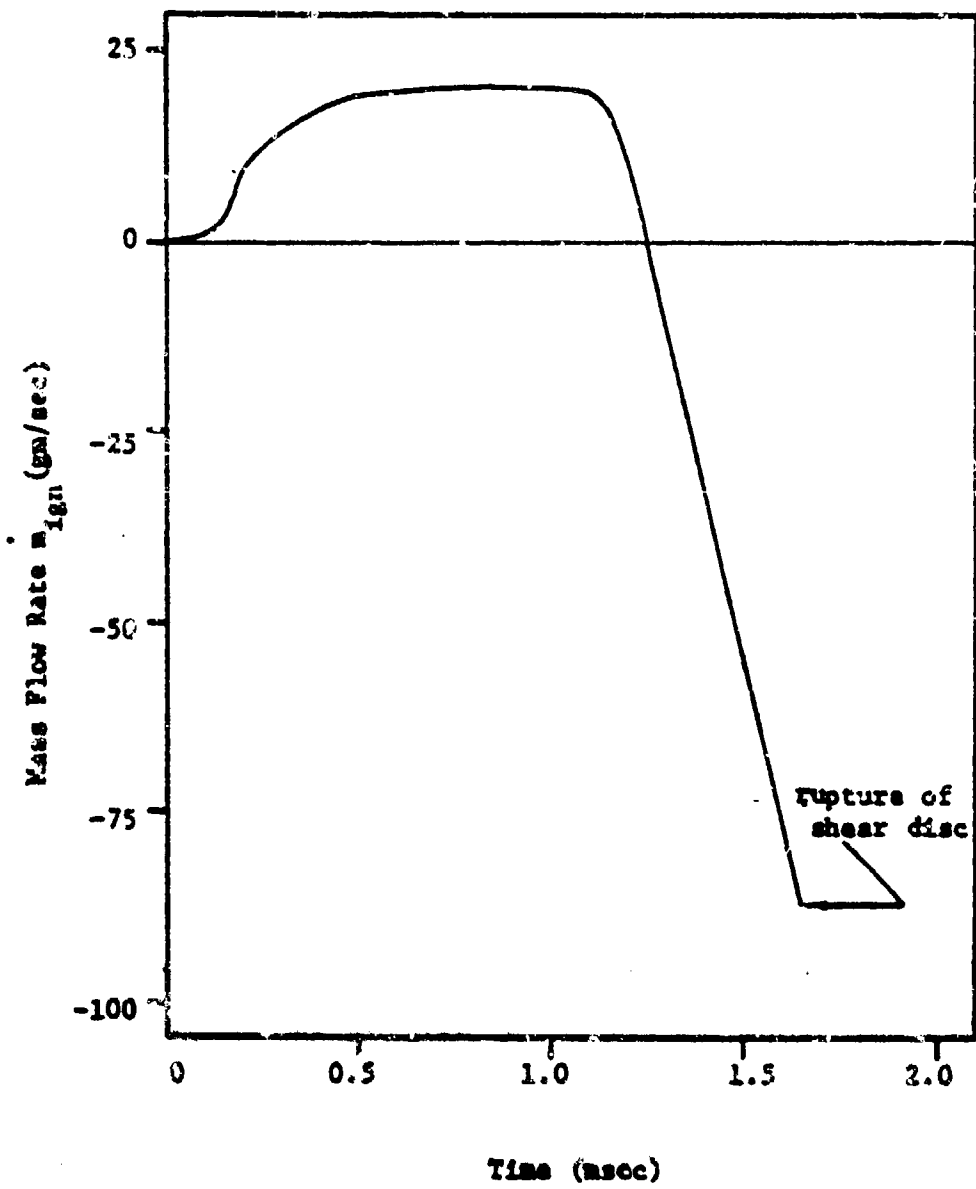
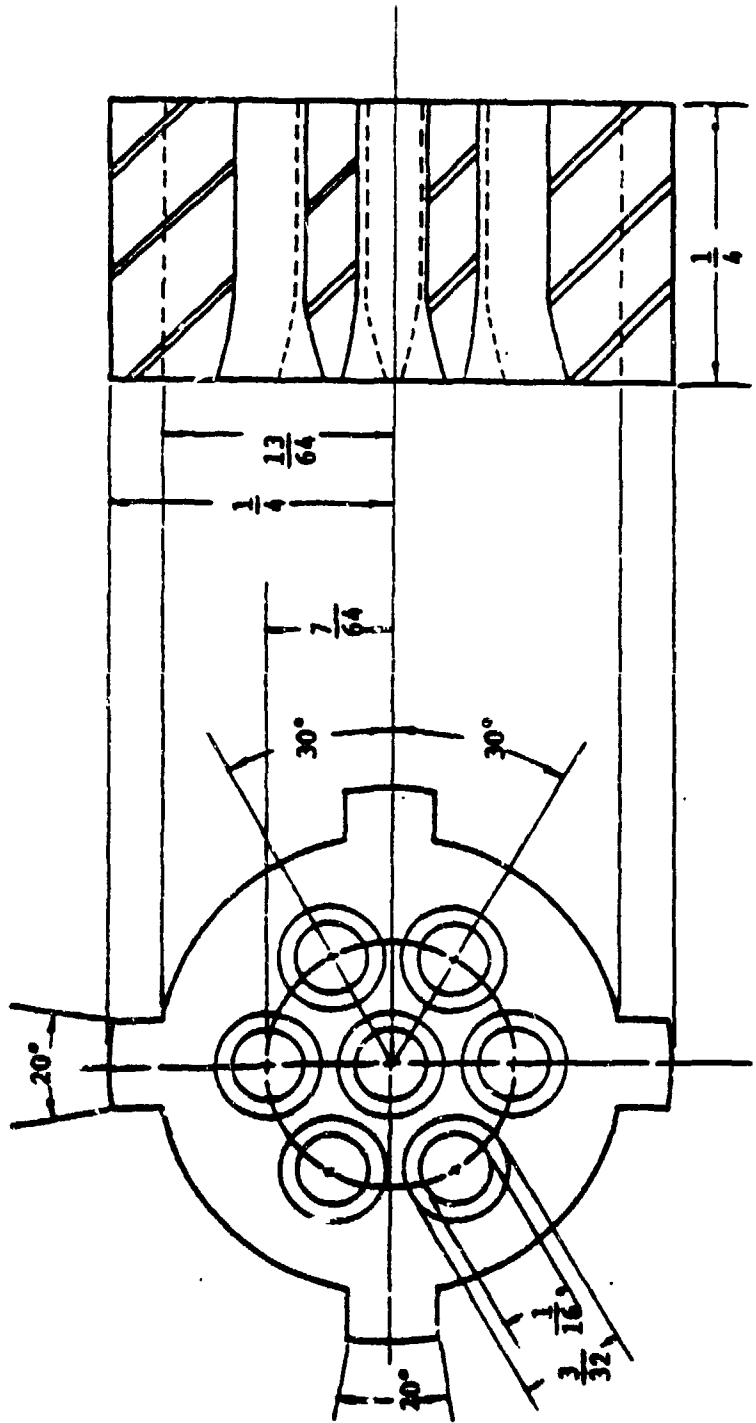


Figure 10 Specified Igniter Mass Flow Rate Flowing into the Granular Bed as a Function of Time



Scale 6": 1"

Figure 11 Schematic Drawing of the Multi-Perforated Convergent Nozzle

speed of 60 ips in order to provide totally time-correlated results. The analog data are then recorded on a transient waveform digitizer (Biomation Waveform Recorder Model 1015) which obtains 100 data points per millisecond of transient data. The data is then expanded by three orders of magnitude in time and plotted on a conventional x-y plotter at a rate of one data point per second.

## 5.2 Discussion of Results

The theoretical results are obtained by using the mathematical model presented in Chapter III. In actual computer coding the simplified equations (see section 3.4) are used. The solution method is shown in Chapter IV.

The predicted values of pressure-time traces at various locations, such as G2, G3, G4 and G5 are shown in Fig. 12. As in a typical set of experimental data given in Fig. 13, the pressurization process at the downstream portion increases faster and eventually overtakes the upstream pressure trace. Further, the data obtained from pressure transducers show that the rate of pressurization invariably increases in the downstream direction. In Fig. 13, the pressure transducer Gauge 1 (G1) was positioned in the igniter chamber, and because of a choked backflow condition at the nozzle, it was found to lag behind the rise in pressure at Gauge 2 location. The four other gauges, G2 to G5, were positioned along the propellant bed with an equal spacing of 3.173 cm (See Fig. 1).

The pressure traces measured in the granular bed indicate that an upstream gauge (such as G2) senses the pressurization much sooner than the gauges at downstream positions. However, the rate of pressurization is significantly higher for the downstream gauges. It is also interesting to note that the pressure peak for G5 is slightly ahead of G2. This is because the depressurization effect due to shear disc rupture, overcomes the pressurization due to propellant gasification at a given station, the pressure-time traces start to decline. The pressure at all stations drops back to one atmosphere, ending a transient interval of about 5 msec.

The predicted pressure-time traces correspond to locations G2, G3, G4 and G5 are individually superimposed on some experimental data for six

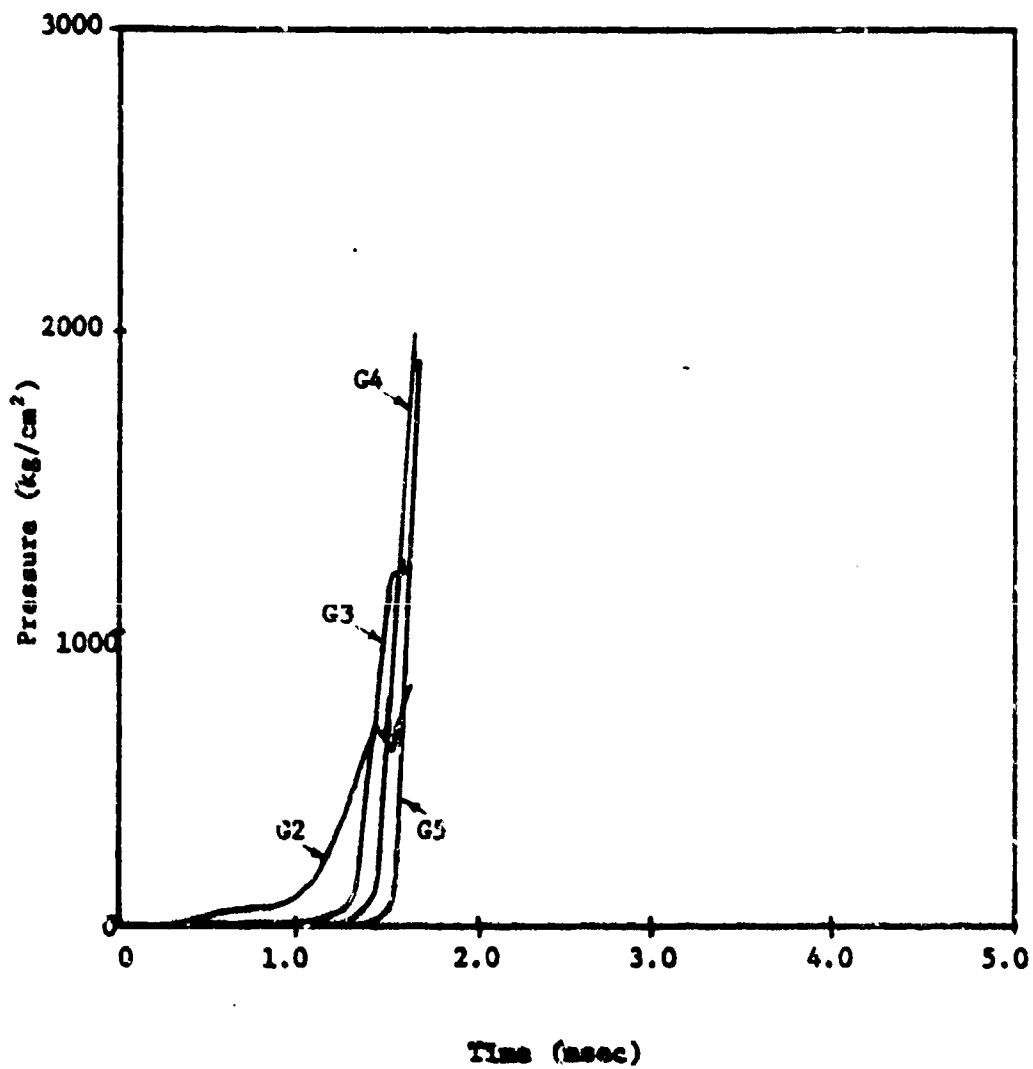


Figure 12 Predicted Pressure-Time Traces for G2, G3, G4 and G5

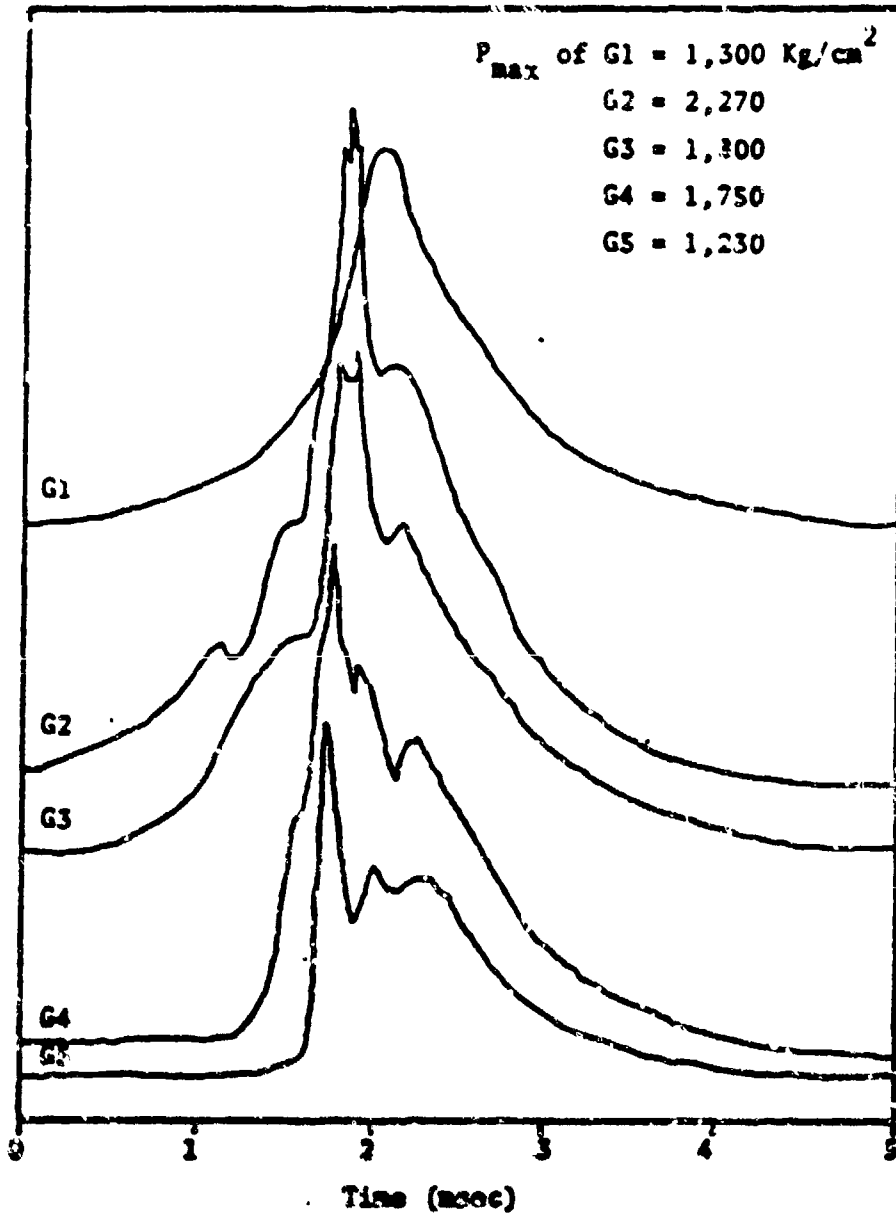


Figure 13 Measured Pressure-Time traces from a Typical Firing  
 (Traces are Offset Vertically for Clarity)

separate firings (tested under the exact conditions) are shown on Figs. 14, 15, 16 and 17 respectively. The shaded region represents the degree of scatter of the experimental data. The solid lines represent the theoretical predictions for the rise in pressure at the corresponding stations. Since the theoretical calculation is limited to the time interval prior to the rupture of the shear disc, no comparison is made for the depressurization processes.

Fig. 14 shows a major portion of the predicted pressure trace at G2 lies in between these firing data, for the early part of the transient interval, the calculated value of pressure is lower than the experimental data. This is probably due to the empirical correlation used for the drag term in the granular bed of inert spheres (Eqs. 3.8.3 or 3.8.4) and may result in higher resistance than the real test condition. In Fig. 15 and 16, the comparison between experimental and theoretical pressure-time traces reveals the same trend. That is, the calculated pressure at G3 and G4 begin to rise at a later time than the experimental data. In Fig. 17, the predicted pressure rises almost at the same time of the experimental results. This gauge, G5 is particularly important; for its location near the shear disc allows us to examine the strength of the pressure spike close to the shear disc.

It is shown clearly from the above comparison that the predicted pressure-time variations at G2, G4, G5 gauge locations not only have the right magnitude but also have reasonable slopes. The pressure rise times are also not far from the experimental measurements. Although the comparison at G3 is less satisfactory than those at G2, G4 and G5, the slope of the pressure-time traces at G3 is not far from that which was measured.

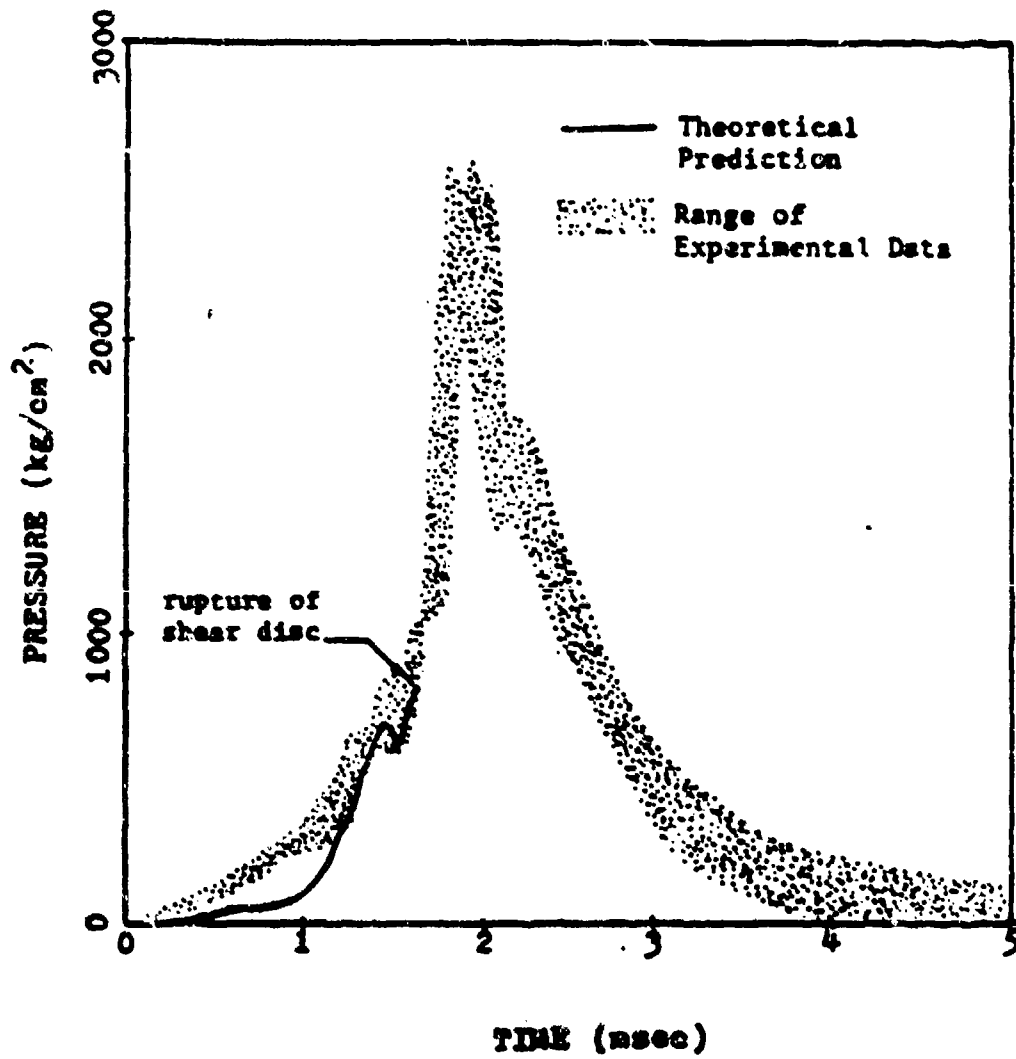


Figure 13 Comparison of Theoretically Predicted G1 Pressure Traces With the Composite Pressure Traces of Six Experimental Firings

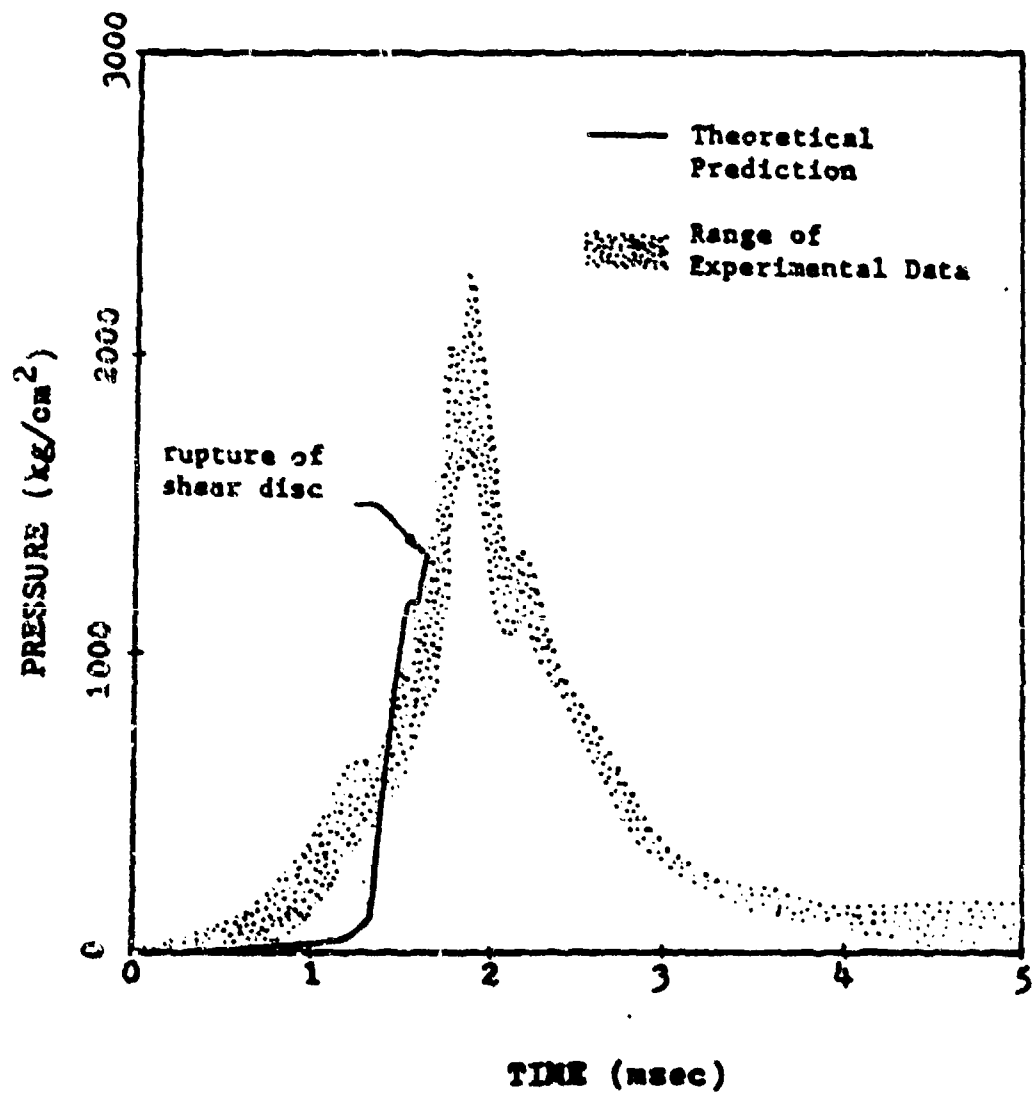


Figure 15 Comparison of Theoretically Predicted G3 Pressure Traces with the Composite Pressure Traces of Six Experimental Firings

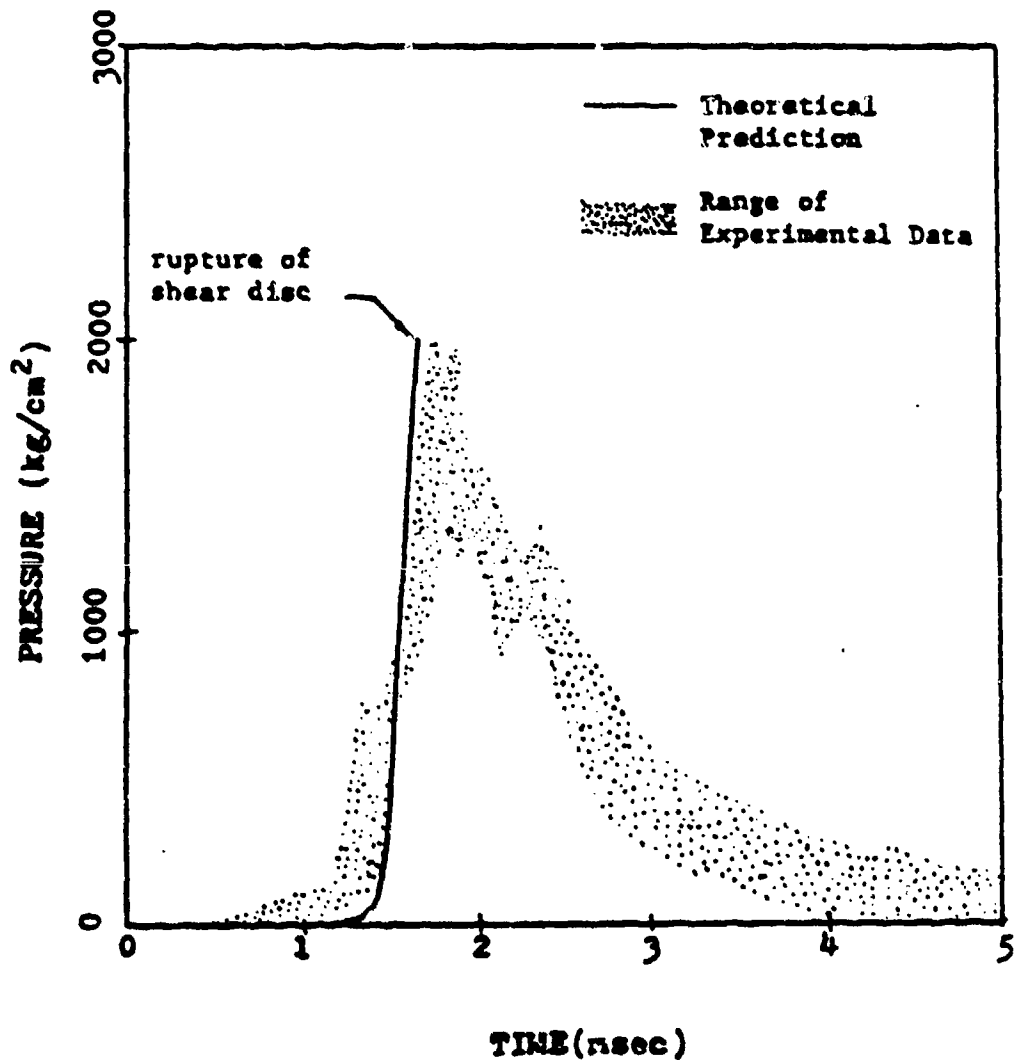


Figure 16 Comparison of Theoretically Predicted G4 Pressure Trace with the Composite Pressure Traces of Six Experimental Firings

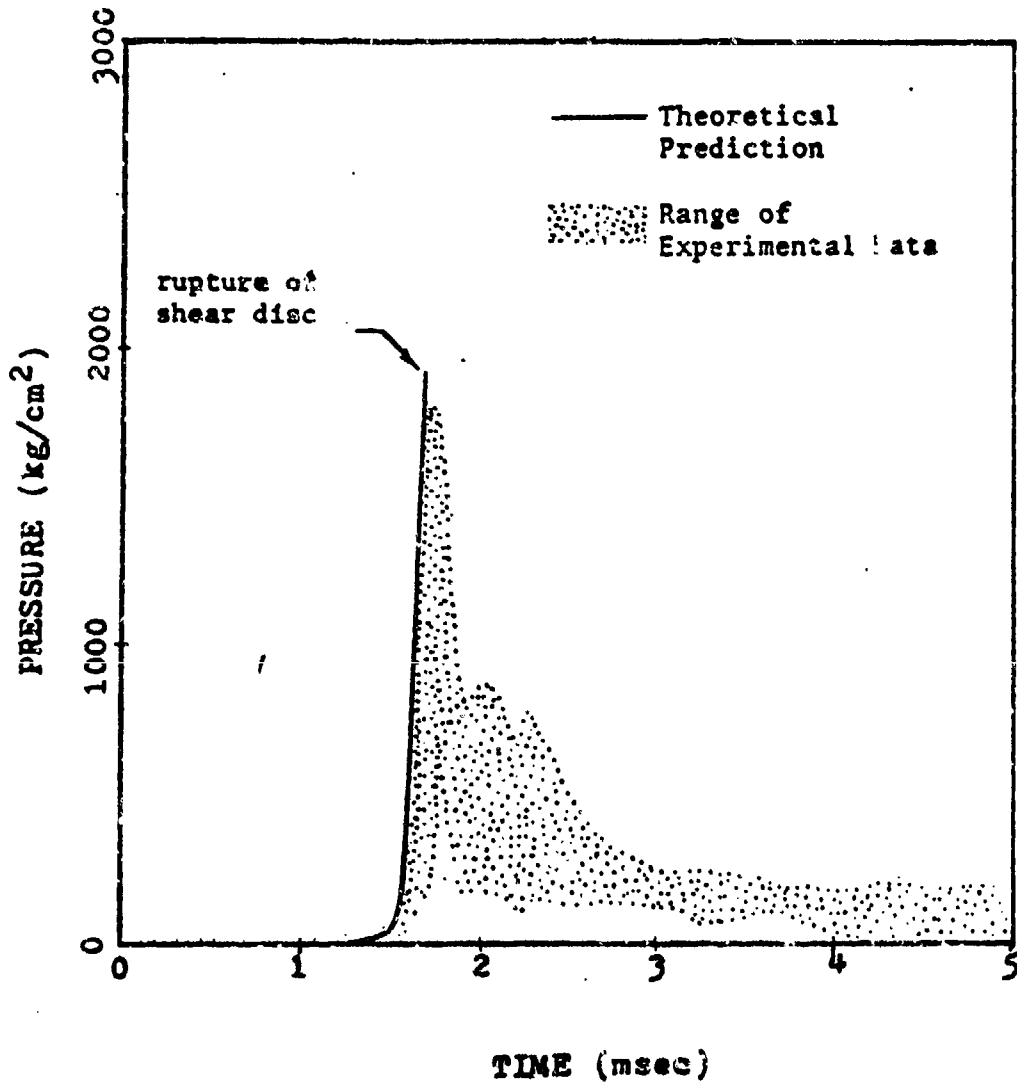


Figure 17 Comparison of Theoretically Predicted G5 Pressure Trace With the Composite Pressure Traces of Six Experimental Firings

In Fig. 18, the calculated flame spreading rate is compared with test data from three separate firings with ionization pin measurements. (Three other firings of the same series consisting of the six runs mentioned above, had no flame front measurements). The calculated results again check quite closely with the experimental data. Both the theoretical results and experimental data indicate a significant increase in flame velocity as the combustion wave propagates in the shear disc direction.

Fig. 19 shows pressure distributions calculated for various times, with the locus of the ignition front (dashed curve) superimposed. Beginning with the trace ( $t = 1.26$  msec), the pressure distribution quickly develops a continental divide and the gradient on its right side becomes steeper with increasing time from the increased gasification rate in the combustion zone. The pressure gradient grows to the left of the peak due to the reverse flow of gases from the granular bed to the igniter chamber. Thus, when the pressure at the head end of the granular bed becomes higher than that in the igniter chamber, the igniter chamber serves as a mass and energy sink to the combustion chamber. The resulting reverse flow of gases also makes the peak more pronounced. Further, the reverse gas flow eventually causes the pressure trace of  $t = 1.54$  to cross that portion of the pressure distribution at  $t = 1.42$  msec (this can also be seen from Fig. 14). Near the end of the chamber the locus of the ignition front curves sharply upward (Fig. 19), due to the extremely rapid pressurization near the shear disc.

Fig. 20 shows the temperature distributions (at times corresponding to Fig. 19), with the locus of the ignition front shown by a dashed curve. The advancement of the combustion wave in the granular bed is readily seen. Early in the transient, the pressure in the system is low, so in

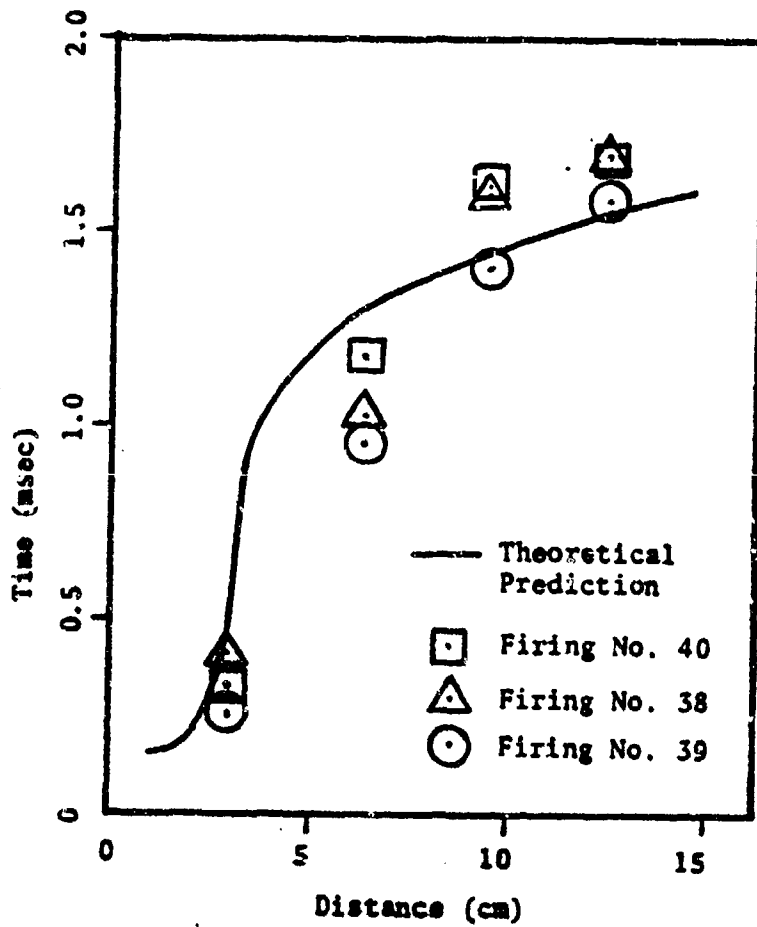


Figure 18. Comparison of Theoretically Predicted Flame Front Position with Experimental Data

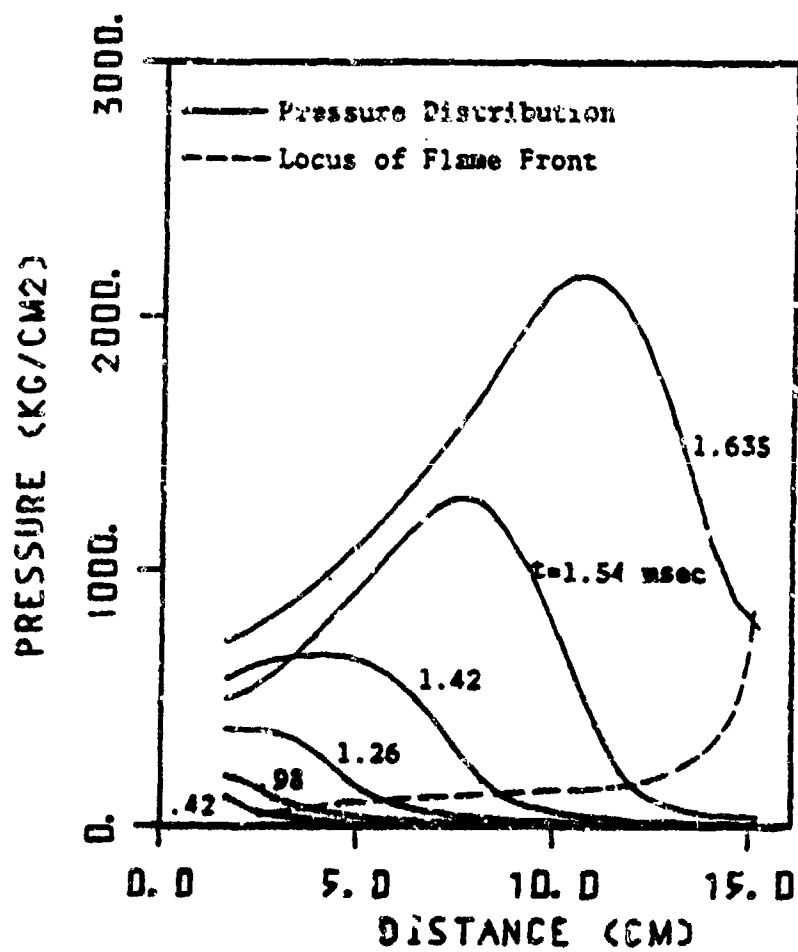


Figure 19 Calculated Pressure Distributions at Various Times

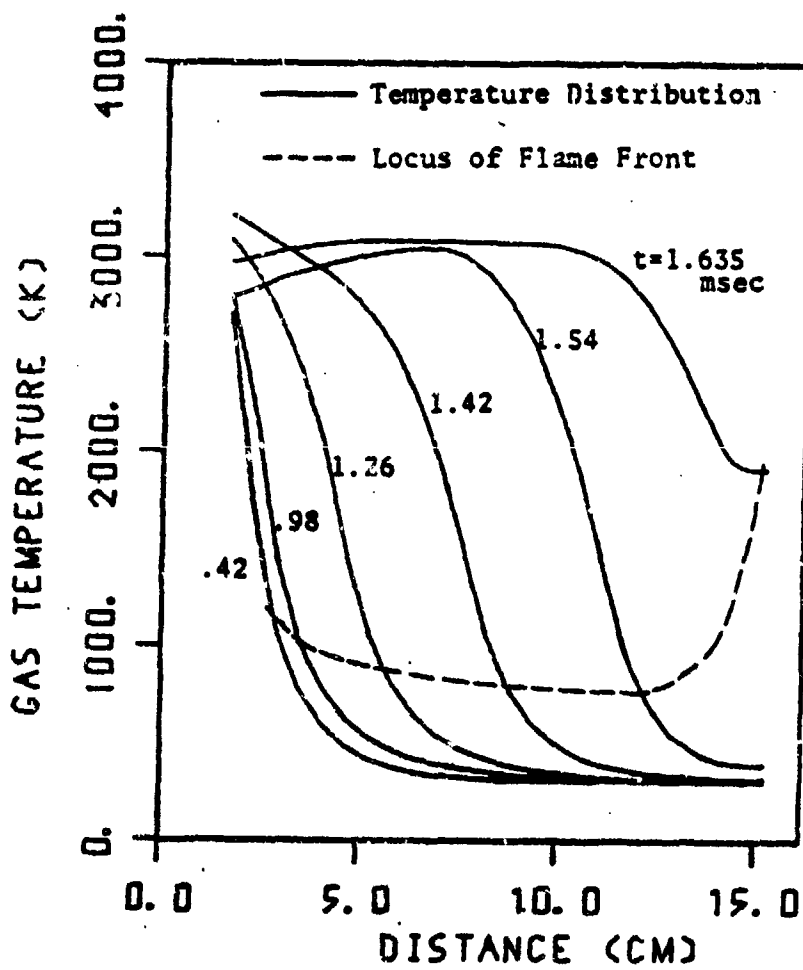


Figure 20 Calculated Gas Temperature Distributions at Various Times

order to heat the granular propellents to ignition condition, the gas temperature at the ignition front must be high. As the pressure rises, the heat transfer from the gas to the unburned propellant becomes more efficient and the ignition front locus descends. Finally, near the end of the granular bed, where the gas velocity is small, the convective heat transfer effect decreases considerably and, therefore, the gas temperature at the ignition front again rises.

Fig. 21 shows the particle temperature distributions. In this figure, the locus of the ignition front is not shown, because it is only a straight line across the temperature scale with  $T_{ps}$  equal to  $T_{abl}$ . The rate of flame front spreading is observed to be more pronounced at the later stage of the transient event.

Fig. 22 shows the corresponding gas velocity distributions. Early in the transient, igniter gas flows into the granular bed and the gas velocity is greatest near the nozzle end. Later, with combustion occurring in the granular bed, a peak develops in the velocity profile driven by the pressure gradient near the ignition front. Still later, the pressure gradient in the granular bed near the nozzle causes reverse flow of hot gases into the igniter chamber; therefore, the gas velocity is negative in the left portion of the combustion chamber.

In Fig. 23 the particle velocity distributions are shown on the same scale to emphasize the fact that particle velocities are in general much lower than the gas velocity. The motion of the particles are generated by the pressure gradients developed in the granular bed. Later in the transient, a fraction of the particles move in the reverse direction near the nozzle end.

The porosity distributions in Fig. 24 show some interesting phenomena.

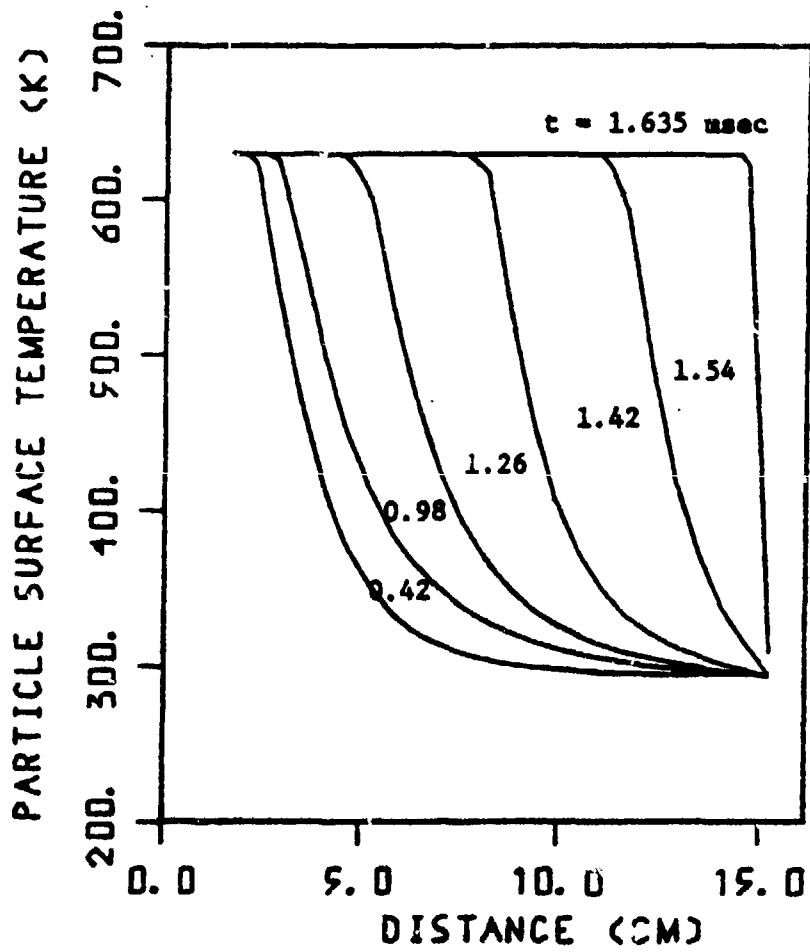


Figure 21 Calculated Particle Temperature Distributions at Various Times

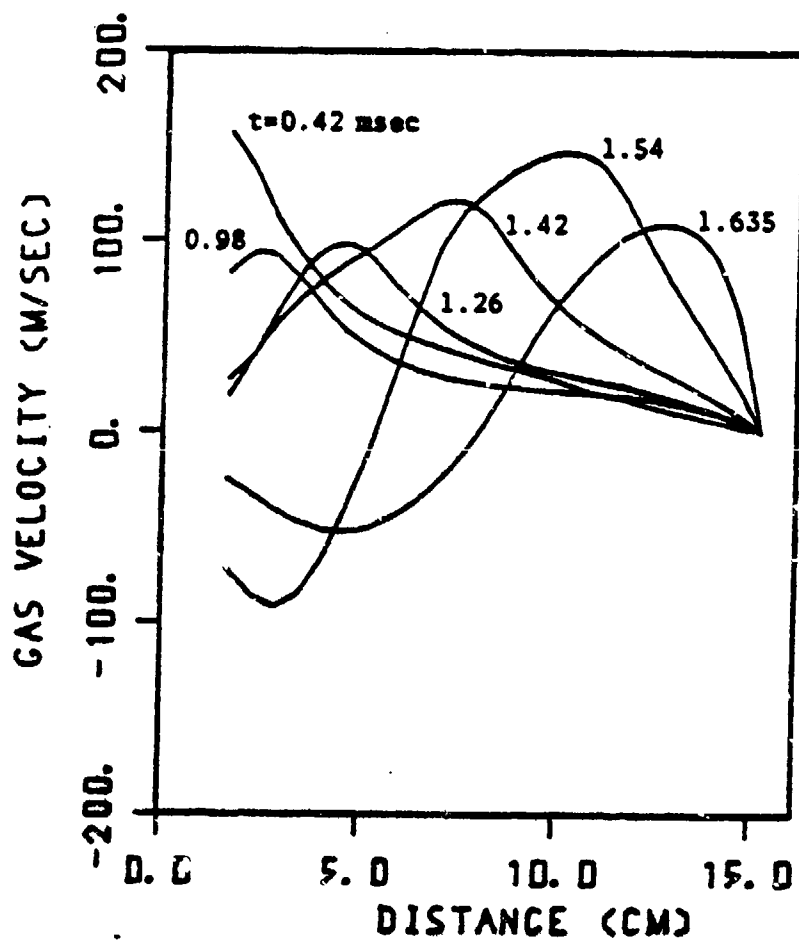


Figure 22 Calculated Gas Velocity Distributions at Various Times

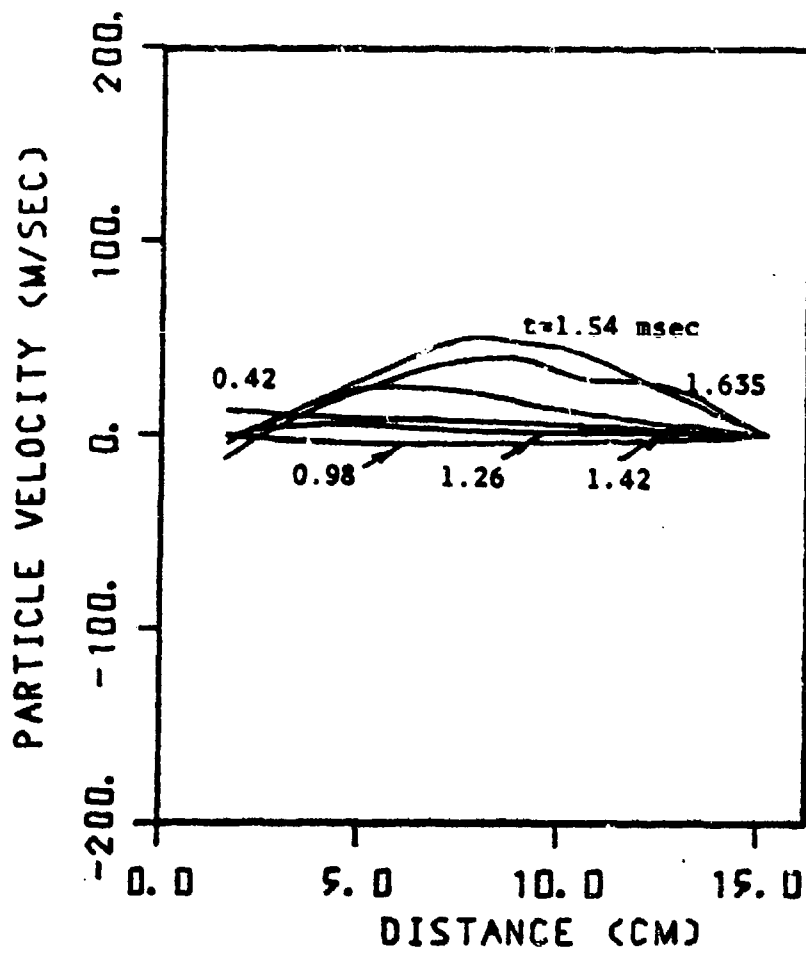


Figure 23. Calculated Particle Velocity Distribution at Various Times

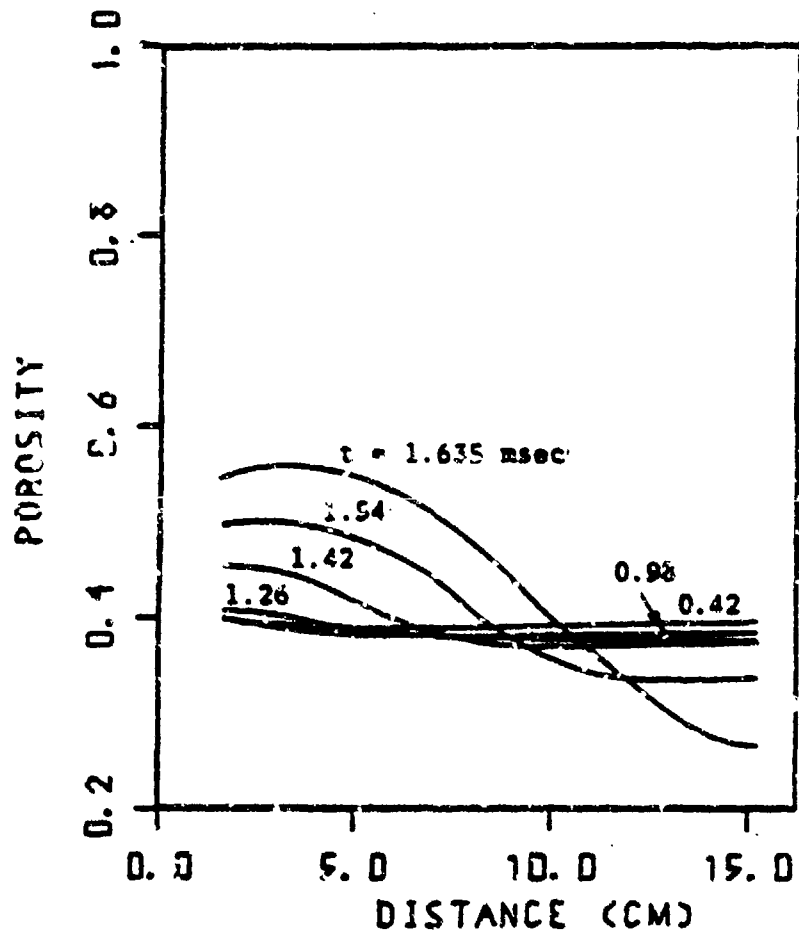


Figure 24 Calculated Porosity Distributions at Various Times

Initially they are quite uniform, but when combustion starts at the nozzle end, grain motion generated by the pressure gradient re-packs the granular bed to reduce the porosity ahead of the ignition front. Behind the front it increases as a result of burning and grain motion in the forward direction.

Quantitatively, the calculated and experimental results are in good agreement. This verifies that the simplified equations in section 3.4 are truly valid.

The shear disc that seals the right end of the chamber is calibrated to withstand a maximum pressure of  $773.4 \text{ Kg/cm}^2$ . The numerical calculation stops when the pressure near the shear disc reaches this critical value. The calculated results show that the diaphragm breaks at 1.638 msec. Similarly, in the experimental process, combustion was terminated immediately after the shear disc ruptured, due to depressurization of the chamber.

## CHAPTER VI

### CONCLUSIONS

An investigation has been conducted for a two-phase, granular propellant combustion problem. Several important conclusions are summarized in the following.

1. A successful theoretical model has been developed to describe the combustion of mobile granular propellants. The calculated pressure-time traces and flame propagation rates agree closely with the experimental results measured by high frequency pressure transducers and ionization probes.
2. A modified two-step Richtmyer explicit scheme is employed in solving the system of hyperbolic partial differential equations. The solution shows that this method is stable and fast convergent when the boundary conditions are solved with the method of characteristics.
3. According to the theoretical calculations and experimental observations, some special features of the combustion process in granular propellants are noted.
  - (a) The rate of pressurization increases in the downstream direction and the pressure peak developed in the granular bed travels downstream.
  - (b) The flame spreading rate increases significantly in the downstream direction.
  - (c) A stronger igniter causes faster flame spreading and also a higher rate of pressurization.
  - (d) Igniter gas flow compacts the bed and causes the propellant grains to move in the shear direction.

- (e) As the pressure peak develops in the chamber, the gas and particle respond to the pressure gradient by moving from center toward both ends of the chamber simultaneously.
- (f) For tightly packed beds, the particle velocity is significantly lower than the gas velocity before the rupture of shear disc.

#### ACKNOWLEDGMENTS

This report represents the experimental results of the research work performed under contract DAAG 29-74-G-0116 at The Pennsylvania State University, under the supervision of the Engineering Sciences Division of the U.S. Army Research Office at Research Triangle Park, North Carolina. The support of Mr. James J. Murray, Director of Engineering Sciences Division, and of Dr. Austin W. Barrows, Jr. of the Ballistic Research Laboratories is greatly appreciated. Thanks are due to Mr. Norman J. Gerri of BRL for his technical advice in this study. Special thanks to Mrs. P. C. Chang and Mr. Glen R. Coates for their assistance in the computer programming. The authors also wish to thank Mrs. Donna Schroyer who typed the manuscript.

#### REFERENCES

1. Kuo, K.K., "Theory of Flame Front Propagation in Porous Propellant Charges Under Confinement", Ph.D. Thesis, Princeton University, AMS Report No. 1000-T, August (1971).
2. Fisher, E.B. and Graves, K.W., "Mathematical Model of Double Base Propellant Ignition and Combustion in the 81 mm Mortar", Calspan Report No. DG-3029-D-1, August (1972).
3. Gough, F.S. and Zwarts, F.J., "Theoretical Model for Ignition of Gun Propellant", Report SRC-R-67, Final Report, Part II, Space Research Corporation, North Troy, Vermont, December (1972).
4. East, J.L. and McClure, D.R., "Projectile Motion Predicted by a Solid/Gas Flow Interior Ballistic Model", Proceedings 10th JANNAF Combustion Meeting, August (1973).
5. Krier, H., Van Tassell, W.F., Rajan, S. and VerShaw, J.T., "Model of Gun Propellant Flame Spreading and Combustion", BRL CR 147 Ballistic Research Laboratories, Aberdeen Proving Ground, Maryland, March (1974). (AD #918842L)
6. Baer, P.G. and Frankle, J.M., "The Simulation of Interior Ballistics Performance of Guns by Digital Computer Program", BRL Report 1183, Ballistic Research Laboratories, Aberdeen Proving Ground, Maryland, December (1962). (AD #299980)
7. Corner, J., Theory of the Interior Ballistics of Guns, New York, John Wiley and Sons, Inc. (1950).
8. Kuo, K.K., Vichnevetsky, R. and Summerfield, M., "Theory of Flame Front Propagation in Porous Propellant Charges Under Confinement", AIAA Journal, Vol. 11, No. 4, pp. 444-451, April (1973).
9. Squire, W.H. and Devine, M.F., "The Interface Between Primer and Propellant", Part I and II, United States Army, Frankford Arsenal, Philadelphia, Pennsylvania (1969).
10. Soper, W.G., "Ignition Waves in Gun Chambers", Combustion and Flame, Vol. 20, No. 2, pp. 157-162 (1973).
11. Kitchens, C.W., Jr., "Flame Spreading in Small Arms Ball Propellant", BRL Report 1604, Ballistic Research Laboratories, Aberdeen Proving Ground, Maryland, August (1972). (AD #750567)
12. Gough, F.S., "The Flow of a Compressible Gas Through an Aggregate of Mobile Reacting Flow", Ph.D. Thesis, McGill University, Montreal, Quebec, December (1974).
13. Beran, M.J., Statistical Continuum Theories, Interscience (1968).
14. Aronow, R.E., "Statistical Approach to Flow Through Porous Media", Phys. Fluids, Vol. 9, No. 9, p. 1721, September (1966).

15. Law, H.S. and Fung, Y.C., "Formulation of a Statistical Equation of Motion of a Viscous Fluid in an Anisotropic Non-Rigid Porous Solid", *Int. J. Solids Structures*, Vol. 6, pp. 1323-1340 (1970).
16. Cox, R.G. and Brenner, H., "The Rheology of a Suspension of Particles in a Newtonian Fluid", *Chem. Eng. Sci.*, Vol. 26, No. 1, pp. 65-93, January (1971).
17. Buyevich, Yu. A., "Statistical Hydromechanics of Disperse Systems", Part 1: Physical Background and General Equations", *J. Fluid Mech.*, Vol. 49, Part 3, pp. 489-507 (1971).
18. Buyevich, Yu. A., "Statistical Hydromechanics of Disperse Systems", Part 2: Solution of the Kinetic Equation for Suspended Particles", *J. Fluid Mech.*, Vol. 52, Part 2, pp. 345-355 (1972).
19. Buyevich, Yu. A., "Statistical Hydromechanics of Disperse Systems", Part 3: Pseudo-Turbulent Structure of Homogeneous Suspensions", *J. Fluid Mech.*, Vol. 56, Part 2, pp. 313-336 (1972).
20. Truesdell, C. and Toupin, R.A., "The Classical Field Theories" in Handbuch der Physik, Vol. III, Part 1, ed. by S. Flügge, Springer Verlag, Berlin (1960).
21. Green, A.E. and Naghdi, P.M., "A Dynamical Theory of Interacting Continua", *Int. J. of Eng. Sci.*, Vol. 3, p. 231 (1965).
22. Green, A.E. and Naghdi, P.M., "A Theory of Mixtures", *Arch. Rat. Mech. Anal.*, Vol. 24, No. 4, p. 243 (1967).
23. Erigen, A.C. and Ingram, J.D., "A Continuum Theory of Chemically Reacting Media", *Int. J. Engineering Science*, Vol. 3, p. 197 (1965).
24. Truesdell, C., Rotational Thermodynamics, Chapter 5, pp. 81-98, McGraw-Hill, New York (1969).
25. Müller, I., "A Thermodynamic Theory of Mixtures of Fluids", *Arch. Rat. Mech. Anal.*, Vol. 28, No. 1, p. 1 (1968).
26. Doria, M.I., "Some General Results for Non-Reacting Binary Mixtures of Fluids", *Arch. Rat. Mech. Anal.*, Vol. 32, No. 5, p. 343 (1969).
27. Slattery, J.C., "Multiphase Viscoelastic Flow Through Porous Media", *AICHE, J.*, p. 50, January (1967).
28. Slattery, J.C., "Flow of Viscoelastic Fluids Through Porous Media", *AICHE, J.*, p. 1066, November (1967).
29. Anderson, T.B. and Jackson, R., "A Fluid Mechanical Description of Fluidized Beds", *I and EC. Fund.*, Vol. 6, No. 4, p. 527 (1967).
30. Whitaker, S., "The Transport Equations for Multi-Phase Systems", *Chem. Eng. Sci.*, Vol. 28, pp. 139-147 (1973).

31. Panton, R., "Flow Properties for the Continuum Viewpoint of a Non-Equilibrium Gas-Particle Mixture", J. Fluid Mech., Vol. 31, Part 2, pp. 273-303 (1968).
32. Williams, F.A., Combustion Theory, Appendix D, Addison-Wesley Publishing Company (1965).
33. Murray, J.D., "On the Mathematics of Fluidization", J. Fluid Mech. Vol. 21, Part 3, pp. 465-493 (1965).
34. Kraiko, A.N. and Sternin, L.E., "Theory of Flows of a Two-Velocity Continuous Medium Containing Solid or Liquid Particles", J. of Applied Math. & Mech., Vol. 29, No. 3, pp. 482-496 (1965).
35. Nigmatulin, R.I., "Methods of Mechanics of a Continuous Medium for the Description of Multi-phase Mixtures", J. of Applied Math. & Mech., Vol. 34, No. 6, pp. 1033-1049 (1970).
36. Kuo, K.K. and Summerfield, M., "High Speed Combustion of Mobile Granular Solid Propellants: Wave Structure and the Equivalent Rankine-Hugoniot Relation", Fifteenth (International) Symposium on Combustion, pp. 515-527 August (1974).
37. Kuo, K.K. and Summerfield, M., "Theory of Steady-State Burning of Porous Propellants by Means of a Gas-Penetrative Mechanism", AIAA 11th Aerospace Science Meeting, Washington DC, January (1973).
38. Kuo, K.K. and Summerfield, M., "Theory of Steady-State Burning of Gas-Permeable Propellants", AIAA Journal, Vol. 12, No. 1, pp. 49-56, January (1974).
39. Kuo, K.K., Vichnevetsky, R. and Summerfield, M., "Generation of Accelerated Flame Front in a Porous Propellant", AIAA Paper No. 71-210, January (1971).
40. Taylor, J.W., "The Burning of Secondary Explosive Powders by a Convective Mechanism", The Faraday Society, Vol. 58 (1962).
41. Bobolev, V.K., Margolis, A.M. and Chuiko, S.V., "Stability of Normal Burning of Porous Systems at Constant Pressure", J. of Combustion, Explosion and Shock Waves, Vol. 2, No. 4 (1966).
42. Andreev K.K., "Thermal Decomposition and Burning of Explosives", Moscow-Leningrad, Gosenergoizdat (1957).
43. Andreev-K.K. and Chuiko, S., "Transition of the Burning of Explosives into an Explosion. I. Burning of Powdered Explosives at Constant High Pressures", Russian Journal of Physical Chemistry, Vol. 37, No. 6, June (1963).
44. Warlick, G.L., "Ignition-Produced, Shock-Loading Phenomena in Naval Guns", CITA Publication 220, 8th JANNAF Combustion Meeting, Vol. 1, September (1971).

45. Ergun, S., "Fluid Flow Through Packed Columns", Chem. Eng. Progr., Vol. 48, pp. 89 (1952).
46. Gough, P.S., "Fundamental Investigation of the Interior Ballistics of Guns", Final Report IHCR 74-1, Naval Ordnance Station, Indian Head, Maryland (1974).
47. Fisher, E.B. and Trippe, A.P., "Development of Basis for Acceptance of Continuously Produced Propellant", Calspan Report No. VQ-5163-D-1, November (1973).
48. Fisher, E.B. and Trippe, A.P., "Mathematical Model of Center Core Ignition in the 175 mm Gun", Calspan Report No. VQ-5163-D-2, March (1974).
49. Fisher, E.B., "Propellant Ignition and Combustion in the 105 mm Howitzer", Calspan Report VQ-5524-D1, January (draft) (1975).
50. Krier, H. and Rajan, S., "Flame Spreading and Combustion in Packed Beds of Propellant Grains", AIAA 13th Aerospace Sciences Meeting, Pasadena, California, Paper No. 75-240 (1975).
51. Zenz, F.A. and Othmer, D.F., Fluidization and Fluid-Particle Systems, Reinhold (1960).
52. Leva, M., Fluidization, McGraw-Hill, New York (1959).
53. Kunii, D and Levenspiel, O., Fluidization Engineering, John Wiley and Sons, Inc., New York (1968).
54. Soo, S.L., Fluid Dynamics of Multi-Phase Systems, Alaisdell (1977).
55. Davidson, J.F. and Harrison, D., Fluidization, Academic Press (1971).
56. Andersson, K.E.B., "Pressure Drop in Ideal Fluidization", Chemical Engineering Science, Vol. 15, pp. 276-297 (1961).
57. Denton, W.H., General Discussion on Heat Transfer, Institution of Mechanical Engineers and American Society of Mechanical Engineers, London, p. 370 (1951).
58. Rowe, P.N. and Claxton, K.T., "Heat and Mass Transfer From a Single Sphere to Fluid Flowing Through an Array", Trans. Inst. Chem. Engrs., Vol. 43, pp. 321-331 (1965).
59. Horst, A.W., Jr., "Solid Propellant Gun Interior Ballistics Modeling: FY-1974 Annual Report," ITR 419, Indian Head, Maryland, January (1975).
60. Moretti, G., "The Choice of a Time Dependent Technique in Gas Dynamics", PIRAL Report No. 69-26, July (1969).
61. Hsiao, D.L., "One-Dimensional Laminar Hydrodynamics and IDLH Hydrocode", SC-RR-69-728, Sandia Laboratories, Albuquerque, New Mexico (1969).

62. Lax, P.D. and Richtmyer, R.D., "Survey of the Stability of Linear Finite Difference Equations", *Communications on Pure and Applied Mathematics*, Vol. 9, pp. 267-293 (1956).
63. Torrance, K.E., "Comparison of Finite-Difference Computations of Natural Convection", *J. of Research of the National Bureau of Standards*, Vol. 72B, No. 4, pp. 281-301, (1968).
64. Phillips, N.A., "An Example of Non-Linear Computational Instability", *Atmosphere and Sea in Motion, Rossby Memorial Volume*, Rockefeller Institute Press, New York (1959).
65. Richtmyer, R.D., "A Survey of Difference Methods for Nonsteady Fluid Dynamics", *NCAR Technical Note 63-2*, Boulder, Colorado (1963).
66. Hirt, C.W., "Heuristic Stability Theory for Finite-Difference Equations", *J. of Computational Physics*, Vol. 2, pp. 339-355 (1968).
67. Gourlay, A.R. and Morris, J.L., "Finite-Difference Methods for Non-Linear Hyperbolic Systems", *Mathematics of Computation*, Vol. 22, No. 101, pp. 28-39, (1968).
68. Lilly, D.K., "On the Computational Solutions of Time-Dependent Non-Linear Geophysical Fluid Dynamics Problems", *U.S. Weather Bureau Monthly Weather Review*, Vol. 93, No. 1, pp. 11-26 (1965).
69. Courant, R., Friedrichs, K. and Lewy, H., "On the Partial Difference Equations of Mathematical Physics", *IBM Journal*, pp. 215-234, March (1967).
70. Richtmyer, R.D. and Morton, K.W., Difference Methods for Initial-Value Problems, 2nd ed., Interscience Published by John Wiley and Sons, New York (1967).
71. Roache, P.J., Computational Fluid Dynamics, Hermosa Publishers, Albuquerque, New Mexico (1972).
72. Courant, R., Isaacson, E. and Rees, M., "On the Solution of Non-Linear Hyperbolic Differential Equations by Finite Differences", *Comm. on Pure and App. Math.*, Vol. V, pp. 243-255 (1952).
73. Fox, L., Numerical Solution of Ordinary and Partial Differential Equations, Addison-Wesley Publishing Co., pp. 205-244 (1962).
74. Vishnevetsky, R., Computer Methods for Partial Differential Equations (Draft Manuscript), February (1971)
75. Strahlow, R.A., Fundamentals of Combustion, International Textbook Company, p. 346 (1968).
76. Kuo, K.K. and Nydagger, C., "Cold Flow Resistance Measurement and Correlation in a Packed Bed of WC 870 Spherical Propellants", to be published (1973).

77. Lenoir, J.M. and Robillard, G., "A Mathematical Method to Predict the Effects of Erosive Burning in Solid-Propellant Rockets", Sixth Symposium (International) on Combustion, p. 663-667, Reinhold (1957).
78. Vichnevetsky, R., "Computer Integration of Hyperbolic Partial Differential Equations by a Method of Lines", Proc. Fourth Australian Computer Conference, Adelaide, South Australia, August (1969).
79. Vichnevetsky, R., "Analog/Hybrid Solution of Partial Differential Equations in the Nuclear Industry", *Simulating*, pp. 269-281, December (1968).
80. Streeter, V.L., "Unsteady Flow Calculations by Numerical Methods", ASME Publication No. 71-WA/FE-13, (1971).
81. Abbett, M.J., "Boundary Condition Computational Procedures for Inviscid Supersonic Flow Field Calculations", Aerotherm Report 71-41, November (1971).
82. Forsythe, G.E. and Wasow, W.R., Finite Difference Methods for Partial Differential Equations, 4th Printing, John Wiley and Sons, Inc., New York, pp. 123-131 (1967).
83. Smith, G.D., Numerical Solution of Partial Differential Equations, Oxford University Press (1965).
84. Moretti, G., "The Importance of Boundary Conditions in the Numerical Treatment of Hyperbolic Equations", PIBAL Report No. 68-34, November (1968).
85. Moretti, G., "A Critical Analysis of Numerical Technique: The Piston-Driven Inviscid Flow", PIBAL Report No. 69-25, July (1969).
86. Moretti, G., "Complicated One Dimensional Flows", PIBAL Report No. 71-25, September (1971).
87. Lax, P., "Weak Solutions of Nonlinear Hyperbolic Equations and Their Numerical Computation", *Comm. Pure Appl. Math.*, Vol. III, pp. 159-193 (1954).
88. Ames, W.F., Numerical Methods for Partial Differential Equations, Barnes and Noble, Inc., pp. 234-238 (1969).
89. Vichnevetsky, R., "Treatment of Boundary Conditions in Difference Methods for One Dimensional Fluid Dynamics Equations", Electronic Associates, Inc., TR 70-21, September (1970).
90. Vichnevetsky, R., "Treatment of the Chamber/Duct Boundary Conditions When the Gas Velocity Changes Signs", Electronic Associates, Inc. TR 71-7, February (1971).
91. Shuman, F.G., "Numerical Methods in Weather Prediction: II Smoothing Filtering", *Monthly Weather Review*, November (1957).

92. Rajan, S., "Evaluation of Numerical Viscosity Effects in Transonic Flow Calculations", Paper No. 73-131, 11th Aerospace Sciences Meeting (1973).
93. Brosseau, T.L., "Development of the Minihat Pressure Transducer for Use in the Extreme Environments of Small Caliber Gun Barrels", BRL MR 2072, Ballistic Research Laboratories, Aberdeen Proving Ground, Maryland (1970). (AD #878325)
94. Bernecker, R.R. and Price, D., "Studies in Transition From Deflagration to Detonation in Granular Explosives - I Experimental Arrangement and Behavior of Explosives Which Fail to Exhibit Detonation", Combustion and Flame, Vol. 22, No. 1, pp. 111-117 (1974).
95. Garri, N.J., Samuel, P.P. and Ortega, .E., "Gas Flow in Porous Beds of Packed Ball Propellant", BRL EMR 159, Ballistic Research Laboratories, Aberdeen Proving Ground, Maryland (1973).
96. Goodman, T.R., "Application of Integral Methods to Transient Non-Linear Heat Transfer," Advances in Heat Transfer, 1, ed. by Irvine, T.F., Jr. and Hartnett, J.P., Academic Press (1964).
97. Courant , R. and Hilbert, D., Methods of Mathematical Physics, Vol. 2, Interscience Publishers, Inc. New York, pp. 407-550, July (1966).
98. Soper, W.G., "Ignition Waves in PYRO Propellant", Combustion and Flame, Vol. 22, pp. 273-276 (1974).
99. Krier, H., "Predictions of Flamespreading and Pressure Wave Propagation in Propellant Beds", Technical Report AAE 75-6, University of Illinois at Urbana-Champaign, July (1975).

--

APPENDIX 1

Conservation Equations in the Eulerian Form

The governing equations for both the gas and particle phases in the Eulerian form can be deduced directly from the governing equations in their divergence form given by Eq. (3.3.3) - (3.3.8), assuming  $A$  is constant.

The mass equation of the gas phase in the Eulerian form is

$$\rho \left( \frac{\partial \phi}{\partial t} + u_g \frac{\partial \phi}{\partial x} \right) + \phi \left( \frac{\partial \rho}{\partial t} + u_g \frac{\partial \rho}{\partial x} \right) + \phi \rho \frac{\partial u_g}{\partial x} = A_s \Gamma_b \rho \quad (A-1.1)$$

The mass equation of the particle phase is

$$\frac{\partial \phi}{\partial t} + u_p \frac{\partial \phi}{\partial x} - (1-\phi) \frac{\partial u_p}{\partial x} = A_s \Gamma_b \quad (A-1.2)$$

The momentum equation of the gas phase is

$$\begin{aligned} & \phi \rho \left( \frac{\partial u_g}{\partial t} + u_g \frac{\partial u_g}{\partial x} \right) + g \left( \phi \frac{\partial \rho}{\partial x} - \frac{\partial (\phi \Gamma_m)}{\partial x} \right) \\ & = A_s \Gamma_b \rho_b (u_p - u_g) - g \left( A_s D_v + \frac{T_{mg} \rho_{mg}}{A} \right) \end{aligned} \quad (A-1.3)$$

The momentum equation of the particle phase is

$$(1-\phi) \rho_b \left( \frac{\partial u_p}{\partial t} + u_p \frac{\partial u_p}{\partial x} \right) - \rho_p c^2 \frac{\partial \phi}{\partial x} - g \left( A_s D_v + \frac{T_{mg} \rho_{mg}}{A} \right) \quad (A-1.4)$$

The energy equation of the particle phase is

$$\begin{aligned} & \phi \rho c_p \left( \frac{\partial T}{\partial t} + u_g \frac{\partial T}{\partial x} \right) + \frac{P}{J} \left( \frac{\partial \phi}{\partial t} + \phi \frac{\partial u_g}{\partial x} \right) - \frac{\partial (\phi \Gamma_m)}{\partial x} + g \frac{T_{mg} \rho_{mg} u_g}{A} + \rho_b \phi \frac{\partial u_g}{\partial x} \\ & - \dot{Q}_w + A_s [(u_g - u_p) \frac{D_v}{J} + \frac{P u_p}{A J} \frac{\partial \phi}{\partial x} - h_c (T - T_m) + \rho_b \Gamma_b [h_{conv} \\ & - C_v T + \frac{(u_g - u_p)^2}{2gJ}]] \end{aligned} \quad (A-1.5)$$

## APPENDIX 2

### Analytical Solution of the Solid-Phase Heat Equation

The heat equation for unburned spherical pellets at a fixed location is given by Eq. (3.3.9), which can be transformed into the Fourier heat equation for the slab case (96) by defining

$$T_p^* = T_p - T_0 \quad (\text{A-2.1})$$

The heat equation becomes

$$\frac{\partial(rT_p^*)}{\partial t} = \alpha_p \frac{\partial(rT_p^*)}{\partial r^2} \quad (\text{A-2.2})$$

The initial condition becomes

$$t=0: T_p^*(0,r) = 0 \quad (\text{A-2.3})$$

The boundary conditions become

$$r=0: \frac{\partial T_p^*}{\partial r}(t,0) = 0 \quad (\text{A-2.4})$$

$$r=r_0: \frac{\partial T_p^*}{\partial r}(t,r_0) = \frac{h_2(t)}{k_p} [T^*(t) - T_p^*(t,r_0)] = Z(t) \quad (\text{A-2.5})$$

We now propose a function for  $T_p^*(t,r)$  as

$$T_p^*(t,r) = \frac{C_0 + C_1 r + C_2 r^2 + C_3 r^3}{r} \quad (\text{A-2.6})$$

Time Period 1 : Before the thermal wave has penetrated to the center of the sphere, i.e.  $\delta < r_p$  (See Fig. 25).

These four constants  $C_0$ ,  $C_1$ ,  $C_2$  and  $C_3$  are to be determined by four conditions. Three of these conditions are,

$$\frac{\partial T_p^*}{\partial r}(t, r_p - \delta) = 0 \quad (\text{A-2.7})$$

$$T_p^*(t, r_p - \delta) = 0 \quad (\text{A-2.8})$$

and

$$\frac{\partial T_p^*}{\partial r}(t, r_p) - \frac{h(t)}{k_p} [T^*(t) - T_p^*(t, r_p)] = Z(t) \quad (\text{A-2.9})$$

plus the smoothing condition:

$$\frac{\partial^2 T_p^*}{\partial r^2}(t, r_p - \delta) = 0 \quad (\text{A-2.10})$$

which tends to make the temperature profile go smoothly into the initial temperature. We define  $r_\delta \equiv r_p - \delta$ , and after some algebraic manipulations and substitution  $C_0$ ,  $C_1$ ,  $C_2$ ,  $C_3$  are as follows:

$$C_0 = \frac{-T^*(t) \delta^2}{2r_p^2 + r_\delta^2 - 3r_p \delta} \quad (\text{A-2.11})$$

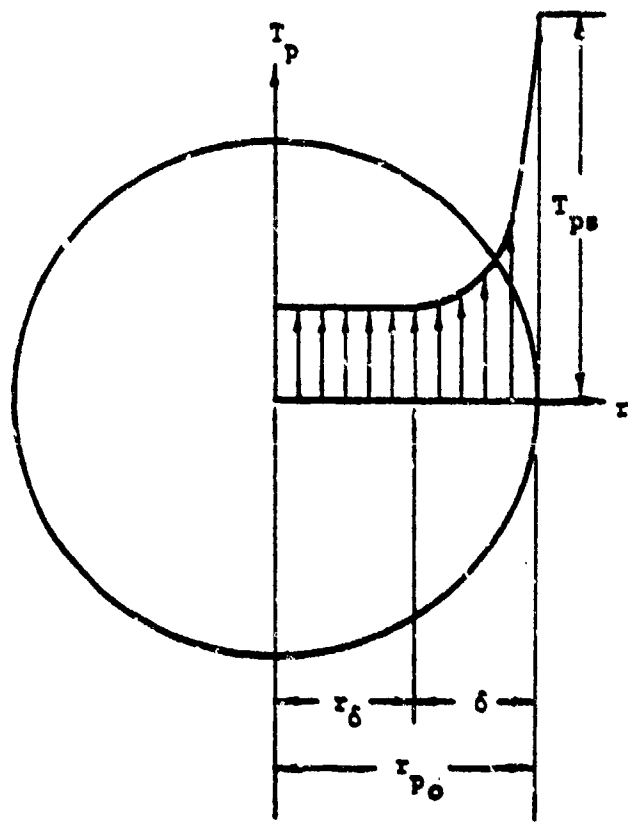


Figure 25 Subsurface Temperature Distribution Inside a Solid Propellant Grain

$$C_1 = \frac{3r_0^2 r_0^2 z}{2r_0^3 + r_0^3 - 3r_0^2 r_0} \quad (\text{A-2.12})$$

$$C_2 = \frac{-3r_0 r_0^2 z}{2r_0^3 + r_0^3 - 3r_0^2 r_0} \quad (\text{A-2.13})$$

$$C_3 = \frac{r_0^2 z}{2r_0^3 + r_0^3 - 3r_0^2 r_0} \quad (\text{A-2.14})$$

Substituting (A-2.11) to (A-2.14) in (A-2.6) we get

$$T_p^*(t, r) = \frac{r_0^2 z}{(2r_0^3 - 3r_0^2 r_0 + r_0^3)} \frac{(r - r_0)^3}{r} \quad (\text{A-2.15})$$

for  $r > r_0$

differentiating Eq. (A-2.15) once we have,

$$\frac{\partial T_p^*}{\partial r} = z \frac{r_0^2}{r^2} \frac{(2r + r_0)(r - r_0)^2}{(2r_0 + r_0)(r_0 - r_0)^2} \quad (\text{A-2.16})$$

differentiating Eq. (A-2.15) twice we have,

$$\frac{\partial^2 T_p^*}{\partial r^2} = \frac{2r_0^2 z}{2r_0^3 - 3r_0^2 r_0 + r_0^3} \left[ \frac{r^3 - r_0^3}{r^3} \right] \quad (\text{A-2.17})$$

When  $r = r_0$ ,  $T_p^*(t, r_0) = T_{ps}^*(t)$  substituting this into (A-2.15)

$$T_{ps}^*(t) = \frac{r_0(r_0 - r_0)}{2r_0 + r_0} \left\{ \frac{h_0(t)}{k_p} [T^*(t) - T_{ps}^*(t)] \right\} \quad (\text{A-2.18})$$

Eq. (A-2.18) expresses a relationship between the pallet surface temperature and the penetration distance. As a result, there is really only one unknown  $f(t)$  [either  $T_{ps}^*(t)$  or  $r_\delta(t)$ ] in Eq. (A-2.15) and this will be obtained from the heat-balance integral.

Integrate Eq. (A-2.2) with respect to  $r$  from  $r_\delta$  to  $r_p$ , we have

$$\int_{r_\delta}^{r_p} r \frac{\partial T_p^*}{\partial t} dr = \alpha_p \int_{r_\delta}^{r_p} \frac{\partial^2 (r T_p^*)}{\partial r^2} dr \quad (A-2.19)$$

The RHS of (A-2.19) can be expressed as

$$\alpha_p \int_{r_\delta}^{r_p} \frac{\partial^2 (r T_p^*)}{\partial r^2} dr = \alpha_p \left[ \frac{\partial (r T_p^*)}{\partial r} \right]_{r_\delta}^{r_p} = \alpha_p [T_{ps}^*(t) + r_p Z(t)] \quad (A-2.20)$$

The LHS of (A-2.19) can be expressed as

$$\int_{r_\delta}^{r_p} r \frac{\partial T_p^*}{\partial t} dr = \frac{r_p^2}{4} \frac{d}{dt} \left[ \frac{(r_p - r_\delta)^2 Z(t)}{(2r_p + r_\delta)} \right] \quad (A-2.21)$$

After substituting Eq. (A-2.20) and Eq. (A-2.21) into Eq. (A-2.19) and some rearranging of terms we come up with an ordinary differential equation by using this integral method,

$$\frac{(3r_p - \delta) \delta^2 \frac{dZ}{dt} + (6r_p Z \delta - \delta^2 Z) \frac{d\delta}{dt}}{(3r_p - \delta)^2} = \frac{4\alpha_p}{r_p} [T_{ps}^*(t) + r_p Z(t)] \quad (A-2.22)$$

re-expressing this equation in terms of  $\frac{dT_{ps}}{dt}$ ,  $r_\delta$  is replaced by  $\delta$  in Eq. (A-2.18) we have

$$T_{ps}^*(t) = \frac{r_{p0} \delta(t)}{3r_{p0} - \delta(t)} Z(t) \quad (A-2.23)$$

Differentiating Eq. (A-2.23) with respect to  $t$  and rearranging we obtain

$$\frac{d\delta}{dt} = \frac{(3r_{p0} - \delta)^2}{3Zr_{p0}^2} \left[ \frac{dT_{ps}^*}{dt} - \frac{r_{p0} \delta}{(3r_{p0} - \delta)} \frac{dZ}{dt} \right] \quad (A-2.24)$$

Substituting Eq. (A-2.24) into Eq. (A-2.22) and using the definition of  $Z(t)$  and the definition of  $T_p^*$  we finally have

$$\left[ \frac{DT_{ps}}{Dt} \right]_p = \frac{\frac{12k_p}{\delta r_{p0}} \left[ (T_{ps} - T_0) + \frac{r_{p0} h_c}{k_p} (T - T_{ps}) \right] + \delta \left[ \frac{h_c}{k_p} \left( \frac{DT}{Dt} \right)_p + \frac{T - T_{ps}}{k_p} \left( \frac{Dh_c}{Dt} \right)_p \right]}{\left[ \frac{(6r_{p0} - \delta)}{r_{p0}} + \frac{h_c \delta}{k_p} \right]} \quad (A-2.25)$$

where  $\delta$  can be obtained from Eq. (A-2.23) with  $\delta$  expressed explicitly,

$$\delta(t) = \frac{3r_{p0} [T_{ps}(t) - T_0]}{[T_{ps}(t) - T_0] + \frac{r_{p0} h_c(t)}{k_p} [T(t) - T_{ps}(t)]} \quad (A-2.26)$$

for  $0 < \delta < r_{p0}$

Eq. (A-2.25) is not well posed, because when  $\delta = 0$ , it will blow up! To bypass this initial singularity, the initial value of  $\delta$  can be based on the initial values of  $T_{ps}$ ,  $T$  and  $h_c$  which are slightly different from undisturbed values.

When  $\delta$  has reached the center of the sphere, the temperature distribution can be obtained from Eq. (A-2.15) by setting  $r_0 = 0$

$$T_p^*(t_p, r) = \frac{h_c(t_p)}{2r_{p0} k_p} r^2 [T(t_p) - T_{ps}(t_p)] \quad (A-2.27)$$

This parabolic profile serves as the initial profile for the temperature distribution at Time Period 2,  $t_p$  represents the time required for the thermal wave to penetrate to the center of the pellet in ignition.

In the similar way the heat equation in the spherical particles for Time Period 2 is derived (after the thermal wave has penetrated to the center of the pellet).

Same equation as Time Period 1 is used,

$$\left[ \frac{DT_p}{Dt} \right]_p = \frac{\alpha_p}{r} \frac{\partial^2 (rT_p)}{\partial r^2} \quad (A-2.28)$$

Initial condition:

$$T_p(t_p, r) = T_0 + \frac{r^2 h_p(t_p)}{2r_p k_p} [T(t_p) - T_{ps}(t_p)] \quad (A-2.29)$$

Boundary condition 1:

$$\frac{\partial T_p}{\partial r}(t, 0) = 0 \quad (A-2.30)$$

Boundary condition 2:

$$\frac{\partial T_p}{\partial r}(t, r_p) = \frac{h_p(t)}{k_p} [T(t) - T(t, r_p)] \quad (A-2.31)$$

Again using the same temperature profile and following the same procedures as Time Period 1 we obtain

$$\left[ \frac{DT_{ps}}{Dt} \right]_p = \frac{\frac{r_p h_p}{2k_p} (T - T_{ps}) + \left[ \left( -\frac{r_p h_p}{8k_p} \right) \left( \frac{DT}{Dt} \right) + \left( \frac{r_p}{8k_p} \right) (T - T_{ps}) \left( \frac{Dh_p}{Dt} \right) \right]}{\left[ \frac{1}{2} + \frac{r_p h_p}{8k_p} \right]} \quad (A-2.32)$$

APPENDIX 3

Characteristic Equations for the System

Five adjoint-eigenvectors,  $W/1$ ,  $W/2$ ,  $W/3$ ,  $W/4$  and  $W/5$  of matrix

M. They are solutions of

$$\left. \begin{aligned} (\tilde{M}^T - \lambda_1 \tilde{I})W/1 &= 0 \\ (\tilde{M}^T - \lambda_2 \tilde{I})W/2 &= 0 \\ (\tilde{M}^T - \lambda_3 \tilde{I})W/3 &= 0 \\ (\tilde{M}^T - \lambda_4 \tilde{I})W/4 &= 0 \\ (\tilde{M}^T - \lambda_5 \tilde{I})W/5 &= 0 \end{aligned} \right\} \quad (A-3.1)$$

$\tilde{M}^T$  is the transpose of the matrix M:

$$\tilde{M}^T = \begin{bmatrix} -u_3 & \frac{-P}{JPC_w} & \frac{-C_g^2 P}{g} & 0 & 0 \\ 0 & -u_6 & 0 & 0 & 0 \\ -\frac{g}{P} & 0 & -u_6 & 0 & 0 \\ 0 & 0 & \frac{-(1-\phi)P^2}{P\phi RTJ} & -u_p & (1-\phi) \\ -\frac{P}{g} & 0 & 0 & \frac{C_g^2}{(1-\phi)} & -u_p \end{bmatrix} \quad (A-3.2)$$

The five eigenvalues  $\lambda_1$ ,  $\lambda_2$ ,  $\lambda_3$ ,  $\lambda_4$  and  $\lambda_5$  are given by Eq. (3.6.5) - (3.6.9)

The first eigenvector from (A-3.1) is

$$(\tilde{M}^T - \lambda, \tilde{I}) W_i = \begin{bmatrix} C_g & -\frac{P}{JPC_v} & -\frac{C_g^2 P}{g} & 0 & 0 \\ 0 & C_g & 0 & 0 & 0 \\ -\frac{g}{P} & 0 & C_g & 0 & 0 \\ 0 & 0 & \frac{-(1-\phi)P^2}{P^2 R T J} & -U_p + U_g + C_g & (1-\phi) \\ -\frac{gP}{\phi P} & 0 & 0 & \frac{C_g^2}{(1-\phi)} & -U_p + U_g + C_g \end{bmatrix} \begin{bmatrix} W_{i1} \\ W_{i2} \\ W_{i3} \\ W_{i4} \\ W_{i5} \end{bmatrix} = \begin{bmatrix} 0 \\ 0 \\ 0 \\ 0 \\ 0 \end{bmatrix}$$

Eq. (A-3.3) implies  $W_{12} = 0$  (A-3.3)

$$C_g W_{11} - \frac{C_g^2 P}{g} W_{13} = 0 \quad (\text{A-3.4})$$

$$-\frac{g}{P} W_{11} + C_g W_{13} = 0 \quad (\text{A-3.5})$$

setting

$$W_{11} = 1 \quad (\text{A-3.6})$$

we have

$$W_{13} = \frac{g}{\phi C_g} \quad (\text{A-3.7})$$

$$(-U_p + U_g + C_g)W_{14} + (1-\phi)W_{15} = \frac{(1-\phi)P^2}{\rho\delta RTJ} W_{13} \quad (\text{A-3.8})$$

and

$$\frac{C^2}{(1-\phi)}W_{14} + (-U_p + U_g + C_g)W_{15} = \frac{\rho P}{\delta P} W_{11} \quad (\text{A-3.9})$$

combining (A-3.6) - (A-3.9), we obtain

$$W_{14} = \frac{(1-\phi)C_g}{\delta\phi(-U_p+U_g+C_g)} - \frac{(1-\phi)P_g}{\phi P [C^2 - (-U_p+U_g+C_g)^2]} \cdot \left\{ \frac{C^2}{(\delta g RTJ)^{1/2} (-U_p+U_g+C_g)} - 1 \right\} \quad (\text{A-3.10})$$

$$W_{15} = \frac{(-U_p+U_g+C_g)P_g}{\rho\phi [C^2 - (-U_p+U_g+C_g)^2]} \cdot \left\{ \frac{C^2}{(\delta g RTJ)^{1/2} (-U_p+U_g+C_g)} - 1 \right\} \quad (\text{A-3.11})$$

By the same token, the other four eigenvectors are determined:

The components of  $W/2$  are:

$$\begin{aligned} W_{21} &= -1 \\ W_{22} &= 0 \\ W_{23} &= \frac{P}{\rho C_g} \\ W_{24} &= \frac{(1-\phi)C_g}{\delta\phi(-U_p+U_g-C_g)} - \frac{(1-\phi)P_g}{\phi P [C^2 - (-U_p+U_g-C_g)^2]} \left\{ \frac{C^2}{(\delta g RTJ)^{1/2} (-U_p+U_g-C_g)} - 1 \right\} \\ W_{25} &= \frac{(-U_p+U_g-C_g)P_g}{\rho\phi [C^2 - (-U_p+U_g-C_g)^2]} \left\{ \frac{C^2}{(\delta g RTJ)^{1/2} (-U_p+U_g-C_g)} - 1 \right\} \end{aligned} \quad (\text{A-3.12})$$

The components of  $W/_{3}$  are

$$\begin{aligned}
 W_{31} &= 0 \\
 W_{32} &= \frac{1}{T} \\
 W_{33} &= -\frac{\sigma-1}{\sigma P} \\
 W_{34} &= \frac{(1-\phi)(-u_p+u_g)(\sigma-1)(JRT+P_b)}{[C^2-(u_p+u_g)^2]\phi\sigma JRT} \\
 W_{35} &= \frac{-C^2(\sigma-1)(JRT+P_b)}{[C^2-(u_p+u_g)^2]\phi\sigma JRT}
 \end{aligned}
 \tag{A-3.13}$$

The components of  $W/_{4}$  are

$$\begin{aligned}
 W_{41} &= W_{42} = W_{43} = 0 \\
 W_{44} &= 1 \\
 W_{45} &= \frac{-C}{1-\phi}
 \end{aligned}
 \tag{A-3.14}$$

The components of  $W/_{5}$  are

$$\begin{aligned}
 W_{51} &= W_{52} = W_{53} = 0 \\
 W_{54} &= -1 \\
 W_{55} &= \frac{C}{(1-\phi)}
 \end{aligned}
 \tag{A-3.15}$$

Since  $W/_{1}$ ,  $W/_{2}$ ,  $W/_{3}$ ,  $W/_{4}$  and  $W/_{5}$  are linearly independent vectors, we may multiply the vector differential equation Eq. (3.6.1) by  $W/_{1}$ ,  $W/_{2}$ ,  $W/_{3}$ ,  $W/_{4}$  and  $W/_{5}$  and obtain five equivalent equations in a new set of dependent variables. For  $i = 1, 2, 3, 4, 5$ .

$$W_i^T \frac{\partial}{\partial t} \begin{bmatrix} u_g \\ T \\ P \\ u_p \\ \emptyset \end{bmatrix} - W_i^T \tilde{M} \frac{\partial}{\partial x} \begin{bmatrix} u_g \\ T \\ P \\ u_g \\ \emptyset \end{bmatrix} + W_i^T \begin{bmatrix} I_1 \\ I_2 \\ I_3 \\ I_4 \\ I_5 \end{bmatrix} \quad (\text{A-3.16})$$

The inhomogeneous terms  $I_1$ ,  $I_2$ ,  $I_3$ ,  $I_4$  and  $I_5$  are defined by Eq. (3.6.2). According to (A-3.1), we have the equality

$$\begin{aligned} W_1^T \tilde{M} &= \lambda_1 W_1^T \\ W_2^T \tilde{M} &= \lambda_2 W_2^T \\ W_3^T \tilde{M} &= \lambda_3 W_3^T \\ W_4^T \tilde{M} &= \lambda_4 W_4^T \\ W_5^T \tilde{M} &= \lambda_5 W_5^T \end{aligned} \quad (\text{A-3.17})$$

Thus (A-3.16) becomes

$$W_i^T \frac{\partial}{\partial t} \begin{bmatrix} u_g \\ T \\ P \\ u_p \\ \emptyset \end{bmatrix} - \lambda_i W_i^T \frac{\partial}{\partial x} \begin{bmatrix} u_g \\ T \\ P \\ u_p \\ \emptyset \end{bmatrix} + W_i^T \begin{bmatrix} I_1 \\ I_2 \\ I_3 \\ I_4 \\ I_5 \end{bmatrix} \quad (\text{A-3.18})$$

for  $i = 1, 2, 3, 4, 5$

Define  $Z_1$ ,  $Z_2$ ,  $Z_3$ ,  $Z_4$  and  $Z_5$  as the scalar functions of  $u_g$ ,  $T$ ,  $P$ ,  $u_p$  and  $\emptyset$  satisfying the following conditions

$$W_1^T = \left( \frac{\partial Z_1}{\partial u_9}, \frac{\partial Z_1}{\partial T}, \frac{\partial Z_1}{\partial P}, \frac{\partial Z_1}{\partial u_p}, \frac{\partial Z_1}{\partial \phi} \right)$$

$$W_2^T = \left( \frac{\partial Z_2}{\partial u_9}, \frac{\partial Z_2}{\partial T}, \frac{\partial Z_2}{\partial P}, \frac{\partial Z_2}{\partial u_p}, \frac{\partial Z_2}{\partial \phi} \right)$$

$$W_3^T = \left( \frac{\partial Z_3}{\partial u_9}, \frac{\partial Z_3}{\partial T}, \frac{\partial Z_3}{\partial P}, \frac{\partial Z_3}{\partial u_p}, \frac{\partial Z_3}{\partial \phi} \right)$$

(A-3.19)

$$W_4^T = \left( \frac{\partial Z_4}{\partial u_9}, \frac{\partial Z_4}{\partial T}, \frac{\partial Z_4}{\partial P}, \frac{\partial Z_4}{\partial u_p}, \frac{\partial Z_4}{\partial \phi} \right)$$

$$W_5^T = \left( \frac{\partial Z_5}{\partial u_9}, \frac{\partial Z_5}{\partial T}, \frac{\partial Z_5}{\partial P}, \frac{\partial Z_5}{\partial u_p}, \frac{\partial Z_5}{\partial \phi} \right)$$

We then have the identities

$$\left( \frac{\partial Z_1}{\partial u_9} \frac{\partial u_9}{\partial t} + \frac{\partial Z_1}{\partial T} \frac{\partial T}{\partial t} + \frac{\partial Z_1}{\partial P} \frac{\partial P}{\partial t} + \frac{\partial Z_1}{\partial u_p} \frac{\partial u_p}{\partial t} + \frac{\partial Z_1}{\partial \phi} \frac{\partial \phi}{\partial t} \right)$$

$$= \lambda_1 \left( \frac{\partial Z_1}{\partial u_9} \frac{\partial u_9}{\partial X} + \frac{\partial Z_1}{\partial T} \frac{\partial T}{\partial X} + \frac{\partial Z_1}{\partial P} \frac{\partial P}{\partial X} + \frac{\partial Z_1}{\partial u_p} \frac{\partial u_p}{\partial X} + \frac{\partial Z_1}{\partial \phi} \frac{\partial \phi}{\partial X} \right) + W_1^T \cdot \dot{I}$$

$$\left( \frac{\partial Z_2}{\partial u_9} \frac{\partial u_9}{\partial t} + \frac{\partial Z_2}{\partial T} \frac{\partial T}{\partial t} + \frac{\partial Z_2}{\partial P} \frac{\partial P}{\partial t} + \frac{\partial Z_2}{\partial u_p} \frac{\partial u_p}{\partial t} + \frac{\partial Z_2}{\partial \phi} \frac{\partial \phi}{\partial t} \right)$$

$$= \lambda_2 \left( \frac{\partial Z_2}{\partial u_9} \frac{\partial u_9}{\partial X} + \frac{\partial Z_2}{\partial T} \frac{\partial T}{\partial X} + \frac{\partial Z_2}{\partial P} \frac{\partial P}{\partial X} + \frac{\partial Z_2}{\partial u_p} \frac{\partial u_p}{\partial X} + \frac{\partial Z_2}{\partial \phi} \frac{\partial \phi}{\partial X} \right) + W_2^T \cdot \dot{I}$$

$$\left( \frac{\partial Z_3}{\partial u_9} \frac{\partial u_9}{\partial t} + \frac{\partial Z_3}{\partial T} \frac{\partial T}{\partial t} + \frac{\partial Z_3}{\partial P} \frac{\partial P}{\partial t} + \frac{\partial Z_3}{\partial u_p} \frac{\partial u_p}{\partial t} + \frac{\partial Z_3}{\partial \phi} \frac{\partial \phi}{\partial t} \right)$$

$$= \lambda_3 \left( \frac{\partial Z_3}{\partial u_9} \frac{\partial u_9}{\partial X} + \frac{\partial Z_3}{\partial T} \frac{\partial T}{\partial X} + \frac{\partial Z_3}{\partial P} \frac{\partial P}{\partial X} + \frac{\partial Z_3}{\partial u_p} \frac{\partial u_p}{\partial X} + \frac{\partial Z_3}{\partial \phi} \frac{\partial \phi}{\partial X} \right) + W_3^T \cdot \dot{I}$$

$$\begin{aligned}
& \left( \frac{\partial z_1}{\partial u_g} \frac{\partial u_g}{\partial t} + \frac{\partial z_1}{\partial T} \frac{\partial T}{\partial t} + \frac{\partial z_1}{\partial P} \frac{\partial P}{\partial t} + \frac{\partial z_1}{\partial u_p} \frac{\partial u_p}{\partial t} + \frac{\partial z_1}{\partial \phi} \frac{\partial \phi}{\partial t} \right) \\
&= \lambda_1 \left( \frac{\partial z_1}{\partial u_g} \frac{\partial u_g}{\partial X} + \frac{\partial z_1}{\partial T} \frac{\partial T}{\partial X} + \frac{\partial z_1}{\partial P} \frac{\partial P}{\partial X} + \frac{\partial z_1}{\partial u_p} \frac{\partial u_p}{\partial X} + \frac{\partial z_1}{\partial \phi} \frac{\partial \phi}{\partial X} \right) + W_4^T \cdot \vec{i} \\
& \left( \frac{\partial z_2}{\partial u_g} \frac{\partial u_g}{\partial t} + \frac{\partial z_2}{\partial T} \frac{\partial T}{\partial t} + \frac{\partial z_2}{\partial P} \frac{\partial P}{\partial t} + \frac{\partial z_2}{\partial u_p} \frac{\partial u_p}{\partial t} + \frac{\partial z_2}{\partial \phi} \frac{\partial \phi}{\partial t} \right) \\
&= \lambda_2 \left( \frac{\partial z_2}{\partial u_g} \frac{\partial u_g}{\partial X} + \frac{\partial z_2}{\partial T} \frac{\partial T}{\partial X} + \frac{\partial z_2}{\partial P} \frac{\partial P}{\partial X} + \frac{\partial z_2}{\partial u_p} \frac{\partial u_p}{\partial X} + \frac{\partial z_2}{\partial \phi} \frac{\partial \phi}{\partial X} \right) + W_5^T \cdot \vec{i}
\end{aligned}$$

(A-3.20)

(A-3.20) can be rewritten as

$$\begin{aligned}
\frac{\partial z_1}{\partial t} &= \lambda_1 \frac{\partial z_1}{\partial X} + W_4^T \cdot \vec{i} \\
\frac{\partial z_2}{\partial t} &= \lambda_2 \frac{\partial z_2}{\partial X} + W_5^T \cdot \vec{i} \\
\frac{\partial z_3}{\partial t} &= \lambda_3 \frac{\partial z_3}{\partial X} + W_6^T \cdot \vec{i} \\
\frac{\partial z_4}{\partial t} &= \lambda_4 \frac{\partial z_4}{\partial X} + W_7^T \cdot \vec{i} \\
\frac{\partial z_5}{\partial t} &= \lambda_5 \frac{\partial z_5}{\partial X} + W_8^T \cdot \vec{i}
\end{aligned}$$

(A-3.21)

Eq. (A-3.21) is the characteristic representation of Eq. (3.6.1).

This has been obtained by changing the dependant variables  $u_g$ ,  $T$ ,  $P$ ,  $u_p$  and  $\phi$  to new variables,  $Z_1$ ,  $Z_2$ ,  $Z_3$ ,  $Z_4$  and  $Z_5$  via the transformation (A-3.16) and (A-3.19). These characteristic equations can be reduced further by virtue of the defined characteristic directions in Eq. (3.7.1) and (3.7.2)

$$\left(\frac{dZ_1}{dt}\right)_s = \frac{\partial Z_1}{\partial t} + \left(\frac{dx}{dt}\right)_s \frac{\partial Z_1}{\partial x} = W_1^T \cdot \bar{i}$$

$$\left(\frac{dZ_2}{dt}\right)_x = \frac{\partial Z_2}{\partial t} + \left(\frac{dx}{dt}\right)_x \frac{\partial Z_2}{\partial x} = W_2^T \cdot \bar{i}$$

$$\left(\frac{dZ_3}{dt}\right)_m = \frac{\partial Z_3}{\partial t} + \left(\frac{dx}{dt}\right)_m \frac{\partial Z_3}{\partial x} = W_3^T \cdot \bar{i}$$

(A-3.22)

$$\left(\frac{dZ_4}{dt}\right)_R = \frac{\partial Z_4}{\partial t} + \left(\frac{dx}{dt}\right)_R \frac{\partial Z_4}{\partial x} = W_4^T \cdot \bar{i}$$

$$\left(\frac{dZ_5}{dt}\right)_V = \frac{\partial Z_5}{\partial t} + \left(\frac{dx}{dt}\right)_V \frac{\partial Z_5}{\partial x} = W_5^T \cdot \bar{i}$$

Since  $Z_1, Z_2, Z_3, Z_4$  and  $Z_5$  are not perfect differentials, the characteristic equation (A-3.22) can be represented by the differentials of  $u_g, T, P, u_p$  and  $\phi$  along the characteristic lines. From the definitions in Eq. (A-3.3) to (A-3.11) and (A-3.19) we have

$$\frac{\partial Z_1}{\partial u_g} = W_{11}$$

$$\frac{\partial Z_1}{\partial T} = W_{12}$$

$$\frac{\partial Z_1}{\partial P} = W_{13}$$

$$\frac{\partial Z_1}{\partial u_p} = W_{14}$$

$$\frac{\partial Z_1}{\partial \phi} = W_{15}$$

(A-3.23)

Since  $Z_1 = Z_1(u_g, T, P, u_p, \phi)$ , by the chain rule we have

$$dZ_1 = \frac{\partial Z_1}{\partial u_g} du_g + \frac{\partial Z_1}{\partial T} dT + \frac{\partial Z_1}{\partial P} dP + \frac{\partial Z_1}{\partial u_p} du_p + \frac{\partial Z_1}{\partial \phi} d\phi$$

(A-3.24)

Similarly, we have

$$dZ_2 = \frac{\partial Z_2}{\partial u_g} du_g + \frac{\partial Z_2}{\partial T} dT + \frac{\partial Z_2}{\partial P} dP + \frac{\partial Z_2}{\partial u_p} du_p + \frac{\partial Z_2}{\partial \phi} d\phi \quad (A-3.25)$$

$$dZ_3 = \frac{\partial Z_3}{\partial u_g} du_g + \frac{\partial Z_3}{\partial T} dT + \frac{\partial Z_3}{\partial P} dP + \frac{\partial Z_3}{\partial u_p} du_p + \frac{\partial Z_3}{\partial \phi} d\phi \quad (A-3.26)$$

$$dZ_4 = \frac{\partial Z_4}{\partial u_g} du_g + \frac{\partial Z_4}{\partial T} dT + \frac{\partial Z_4}{\partial P} dP + \frac{\partial Z_4}{\partial u_p} du_p + \frac{\partial Z_4}{\partial \phi} d\phi \quad (A-3.27)$$

$$dZ_5 = \frac{\partial Z_5}{\partial u_g} du_g + \frac{\partial Z_5}{\partial T} dT + \frac{\partial Z_5}{\partial P} dP + \frac{\partial Z_5}{\partial u_p} du_p + \frac{\partial Z_5}{\partial \phi} d\phi \quad (A-3.28)$$

Substituting Eq. (A-3.24) - (A-3.28) into (A-3.22) we get

$$W_{11}(du_g)_z + W_{12}(dT)_z + W_{13}(dP)_z + W_{14}(du_p)_z + W_{15}(d\phi)_z - [W_1^T \cdot \bar{I}] \Delta t \quad (A-3.29)$$

$$W_{21}(du_g)_z + W_{22}(dT)_z + W_{23}(dP)_z + W_{24}(du_p)_z + W_{25}(d\phi)_z - [W_2^T \cdot \bar{I}] \Delta t \quad (A-3.30)$$

$$W_{31}(du_g)_z + W_{32}(dT)_z + W_{33}(dP)_z + W_{34}(du_p)_z + W_{35}(d\phi)_z - [W_3^T \cdot \bar{I}] \Delta t \quad (A-3.31)$$

$$W_{41}(du_g)_z + W_{42}(dT)_z + W_{43}(dP)_z + W_{44}(du_p)_z + W_{45}(d\phi)_z - [W_4^T \cdot \bar{I}] \Delta t \quad (A-3.32)$$

$$W_{51}(du_g)_z + W_{52}(dT)_z + W_{53}(dP)_z + W_{54}(du_p)_z + W_{55}(d\phi)_z - [W_5^T \cdot \bar{I}] \Delta t \quad (A-3.33)$$

Where the vector products of  $W/1$ ,  $W/2$ ,  $W/3$ ,  $W/4$  and  $W/5$  with  $\bar{I}$  are given as

$$W/1 \cdot \bar{I} = W_{11} I_1 + W_{12} I_2 + W_{13} I_3 + W_{14} I_4 + W_{15} I_5 = K_{cm}^I$$

$$W/2 \cdot \bar{I} = W_{21} I_1 + W_{22} I_2 + W_{23} I_3 + W_{24} I_4 + W_{25} I_5 = K_{cm}^{II}$$

$$W/3 \cdot \bar{I} = W_{31} I_1 + W_{32} I_2 + W_{33} I_3 + W_{34} I_4 + W_{35} I_5 = K_{cm}^{III} \quad (A-3.34)$$

$$W/4 \cdot \bar{I} = W_{41} I_1 + W_{42} I_2 + W_{43} I_3 + W_{44} I_4 + W_{45} I_5 = K_{cm}^{IV}$$

$$W/5 \cdot \bar{I} = W_{51} I_1 + W_{52} I_2 + W_{53} I_3 + W_{54} I_4 + W_{55} I_5 = K_{cm}^V$$

Substituting Eq. (A-3.34) into (A-3.24) - (A-3.33) and using the definitions of  $I_1$ ,  $I_2$ ,  $I_3$ ,  $I_4$  and  $I_5$ , we obtained the characteristic equations (3.6.11) - (3.6.17).

Besides the above five characteristic equations, we still require the consideration of another, yet to be determined, namely the particle-path line in the particle phase.

From the heat equation of the particle phase we obtained Eq. (3.3.9) rewritten as follows,

$$\frac{DT_{ps}}{Dt} = \frac{\frac{h_c k_p}{\delta r_p} [(T_{ps} - T_s) + \frac{r_p h_c}{k_p} (T - T_{ps})] + \delta \left[ \frac{h_c}{k_p} \left[ \frac{DT}{Dt} \right] + \frac{T - T_{ps}}{k_p} \left[ \frac{Dh_c}{Dt} \right] \right]}{\left[ \frac{(6r_p - \delta)}{r_p} + \frac{h_c \delta}{k_p} \right]} \quad (A-3.35)$$

for convenience sake we define the following parameters, the inhomogeneous term in Eq. (A-3.35) is

$$I = \frac{\frac{12\alpha_p}{\delta r_p} [(T_{ps} - T_o) + \frac{r_p h_c}{k_p} (T - T_{ps})]}{\left[ \frac{(6r_p - \delta)}{r_p} + \frac{h_c \delta}{k_p} \right]} \quad (\text{A-3.36})$$

and the non-linear terms are

$$N_1 = \frac{\delta \left( \frac{h_c}{k_p} \right)}{\left[ \frac{(6r_p - \delta)}{r_p} + \frac{h_c \delta}{k_p} \right]} \quad (\text{A-3.37})$$

and

$$N_2 = \frac{\delta \left( \frac{T - T_{ps}}{k_p} \right)}{\left[ \frac{(6r_p - \delta)}{r_p} + \frac{h_c \delta}{k_p} \right]} \quad (\text{A-3.38})$$

After an order of magnitude analysis,  $N_2$  is found to be much smaller than  $N_1$ , so we decided to drop the  $N_2$  term.

We now have a better form of Eq. (A-3.35),

$$\frac{\partial T_{ps}}{\partial t} + u_p \frac{\partial T_{ps}}{\partial x} = I + N_1 \left( \frac{\partial T}{\partial t} + u_p \frac{\partial T}{\partial x} \right) \quad (\text{A-3.39})$$

Again define

$$\left( \frac{\partial T}{\partial t} \right) = U_p \quad (\text{A-3.40})$$

Therefore, we get

$$\left(\frac{dT_{ps}}{dt}\right)_{II} = I + N_1 \left(\frac{dT}{dt}\right)_{II} \quad (A-3.41)$$

The sixth characteristic equation can be expressed as

$$K_{T_{ps_1}}^{II} (dT_{ps})_{II} + K_{T_1}^{II} (dT)_{II} = K_{t_{m_1}}^{II} \Delta t \quad (A-3.42)$$

for Time Period 1.

A similar equation derived for Time Period 2 is,

$$K_{T_{ps_2}}^{II} (dT_{ps})_{II} + K_{T_2}^{II} (dT)_{II} = K_{t_{m_2}}^{II} \Delta t \quad (A-3.43)$$

In summary, the final forms of the characteristic equations derived above are shown in the following.

The right-running characteristic equation in the gas phase

$$K_{u_g}^I (du_g)_I + K_p^I (dp)_I + K_{u_p}^I (du_p) + K_\phi^I (d\phi)_I = K_{t_{cm}}^I \Delta t \quad (A-3.44)$$

The coefficients of the above equation are,

$$K_{u_g}^I = 1 \quad (A-3.45)$$

$$K_p^I = -\frac{g}{\beta C_g} \quad (A-3.46)$$

$$K_{u_p}^I = \left\{ \frac{(1-\phi)C_g}{\beta(u_p + u_g + C_g)\phi} - \frac{(1-\phi)XRTJ + Pb}{\beta[C^2 + (u_p + u_g + C_g)]} \left[ \frac{C^2}{2XRTJ(u_p + u_g + C_g)} - 1 \right] \right\} \quad (A-3.47)$$

$$K_{\phi}^i = \left\{ \frac{(-U_p + U_g + C_g)(RTJ + PD)g}{[C^2 - (-U_p + U_g + C_g)^2]} \phi \left[ \frac{C^2}{\delta g RTJ (-U_p + U_g + C_g)} - 1 \right] \right\} \quad (\text{A-3.48})$$

$$K_{im}^i = \frac{A_p}{\delta P} [P_p \Gamma_b (U_p - U_g) \delta D] + \frac{g A_p P}{\delta^2 C_g \delta T} \left\{ \frac{P P_p}{RT} \left( \frac{P_p}{P} - 1 \right) + \frac{1}{C_v} \left[ (U_g - U_p) \cdot \right. \right.$$

$$\left. \frac{1}{J} \left( D_c + \frac{U_g P_p \Gamma_b}{g} \right) - h_T (T - T_{ps}) + P_p \Gamma_b \left[ h_{chem} - C_v T + \frac{(U_p - U_g)^2}{2gJ} \right] \right\}$$

$$+ \frac{A_p g D_c}{P_p} \left\{ \frac{C_g}{\delta (-U_p + U_g + C_g) \phi} - \frac{g P}{\delta [C^2 - (-U_p + U_g + C_g)^2]} \phi \right.$$

$$\left. \left[ \frac{C^2}{\delta g RTJ (-U_p + U_g + C_g)} - 1 \right] \right\} + \left\{ \frac{A_p \Gamma_b (-U_p + U_g + C_g) g P}{\delta [C^2 - (-U_p + U_g + C_g)^2]} \phi \right.$$

$$\left. \left[ \frac{C^2}{\delta g RTJ (-U_p + U_g + C_g)} - 1 \right] \right\} \quad (\text{A-3.49})$$

The left-running characteristic equation in the gas phase,

$$K_{u_g}^{\Sigma} (du_g)_{\Sigma} + K_P^{\Sigma} (dP)_{\Sigma} + K_{u_p}^{\Sigma} (du_p)_{\Sigma} + K_{\phi}^{\Sigma} (d\phi)_{\Sigma} = K_{im}^{\Sigma} \Delta t \quad (\text{A-3.50})$$

The coefficients of the above equation are,

$$K_{u_g}^{\text{II}} = -1 \quad (\text{A-3.51})$$

$$K_P^{\text{II}} = \frac{g}{P C_g} \quad (\text{A-3.52})$$

$$K_{u_p}^{\text{II}} = \left\{ \frac{(1-\phi)C_g}{\delta(-u_p+u_g-C_g)\phi} - \frac{(1-\phi)(RTJ+P_b)g}{[C^2-(-u_p+u_g-C_g)^2]\phi} \right. \\ \left. \left[ \frac{C^2}{\sqrt{89RTJ}(-u_p+u_g-C_g)} + 1 \right] \right\} \quad (\text{A-3.53})$$

$$K_{\phi}^{\text{II}} = \left\{ \frac{(-u_p+u_g-C_g)(RTJ+P_b)g}{[C^2-(-u_p+u_g-C_g)^2]\phi} \left[ \frac{C^2}{\sqrt{89RTJ}(-u_p+u_g-C_g)} + 1 \right] \right\} \quad (\text{A-3.54})$$

$$K_{c_m}^{\text{II}} = -\frac{A_s}{\delta P} [P_b \Gamma_b (u_p - u_g) - 3D_g] + \frac{g P A_s}{\delta^2 \sqrt{C_g} T} \left[ \frac{P_b}{RT} \left( \frac{P_b}{P} - 1 \right) \right. \\ \left. + \frac{1}{C_v} \left\{ \frac{1}{J} (u_g - u_p) (D_g + \frac{u_g P_b \Gamma_b}{g}) - h_c (T - T_{pe}) + P_b \Gamma_b [h_{chem} \right. \right. \\ \left. \left. - C_v T + \frac{(u_p^2 - u_g^2)}{2gT} \right] \right\} + \frac{A_s 3D_g}{P_p} \left\{ \frac{C_g}{\delta(-u_p+u_g-C_g)\phi} - \frac{gP}{P[C^2-(-u_p+u_g-C_g)^2]\phi} \right. \\ \left. \left[ \frac{C^2}{\sqrt{89RTJ}(-u_p+u_g-C_g)} + 1 \right] \right\} + \left\{ \frac{A_s \Gamma_b g P (-u_p+u_g-C_g)}{P \phi [C^2-(-u_p+u_g-C_g)^2]} \right. \\ \left. \left[ \frac{C^2}{\sqrt{89RTJ}(-u_p+u_g-C_g)} + 1 \right] \right\} \quad (\text{A-3.55})$$

The gaseous-path characteristic equation is the gas phase

$$K_T^{\Xi} (dT)_{\Xi} + K_P^{\Xi} (dP)_{\Xi} + K_{u_p}^{\Xi} (du_p)_{\Xi} + K_{\phi}^{\Xi} (d\phi)_{\Xi} = K_{cm}^{\Xi} \Delta T \quad (\text{A-3.56})$$

The coefficients of the above equation are,

$$K_T^{\Xi} = \frac{1}{T} \quad (\text{A-3.57})$$

$$K_P^{\Xi} = -\left[\frac{(\delta-1)}{\delta P}\right] \quad (\text{A-3.58})$$

$$K_{u_p}^{\Xi} = \frac{(1-\phi)(-u_p + u_g)(\delta-1)(JRT + P_b)}{[c^2 - (-u_p + u_g)^2] \phi \delta JRT} \quad (\text{A-3.59})$$

$$K_{\phi}^{\Xi} = \frac{-c^2(\delta-1)(JRT + P_b)}{[c^2 - (-u_p + u_g)^2] \phi \delta JRT} \quad (\text{A-3.60})$$

$$K_{cm}^{\Xi} = \frac{A_s}{\phi P T c} \left\{ (u_g - u_p) \left( \frac{P_b}{J} + \frac{u_g P_b}{g} \right) - h_T (T - T_{ps}) + P_b \Gamma_b [h_{chem} - c_v T + \frac{(u_p^2 - u_g^2)}{2gT}] \right\} - \frac{(\delta-1) A_s}{\delta \phi T P} \left\{ \frac{P \Gamma_b}{R J} \left( \frac{P_b}{P} - 1 \right) - \frac{1}{c_v} \left[ (u_g - u_p) \cdot \frac{1}{J} \left( D_c + \frac{u_g P_b \Gamma_b}{g} \right) - h_T (T - T_{ps}) + P_b \Gamma_b [h_{chem} - c_v T + \frac{(u_p^2 - u_g^2)}{2gT}] \right] \right\} + \frac{A_s \phi D_c (\delta-1) C_g (u_g - u_p)}{[c^2 - (-u_p + u_g)^2] P_b \delta P \delta JRT} - \left\{ \frac{A_s \Gamma_b C_g (\delta-1) c^2}{J \delta JRT \phi \delta [c^2 - (-u_p + u_g)^2]} \right\}$$

(A-3.61)

The right-running characteristic equation in the particle phase is

$$K_{u_p}^{\text{II}}(du_p)_{\text{II}} + K_{\phi}^{\text{II}}(d\phi)_{\text{II}} = K_{t_m}^{\text{II}} \Delta t \quad (\text{A-3.62})$$

The coefficients of the above equations are,

$$K_{u_p}^{\text{II}} = 1 \quad (\text{A-3.63})$$

$$K_{\phi}^{\text{II}} = -\left(\frac{c}{1-\phi}\right) \quad (\text{A-3.64})$$

$$K_t^{\text{II}} = \frac{A_2 g D_c}{\rho_p (1-\phi)} - \frac{A_2 \Gamma_b c}{(1-\phi)} \quad (\text{A-3.65})$$

The left-running characteristic equation in the particle phase is

$$K_{u_p}^{\text{V}}(du_p)_{\text{V}} + K_{\phi}^{\text{V}}(d\phi)_{\text{V}} = K_{t_m}^{\text{V}} \Delta t \quad (\text{A-3.66})$$

The coefficients of the above equation are,

$$K_{u_p}^{\text{V}} = 1 \quad (\text{A-3.67})$$

$$K_{\phi}^{\text{V}} = \left(\frac{c}{1-\phi}\right) \quad (\text{A-3.68})$$

$$K_t^{\text{V}} = \frac{A_2 g D_c}{\rho_p (1-\phi)} + \frac{A_2 \Gamma_b c}{(1-\phi)} \quad (\text{A-3.69})$$

The particle-path characteristic equation in the particle phase in either (Time Period 1),

$$K_{T_{ps},1}^{\text{II}} (dT_{ps})_{\text{II}} + K_{T_1}^{\text{II}} (dT)_{\text{II}} = K_{c_{m,1}}^{\text{II}} \Delta t \quad (\text{A-3.70})$$

or (Time Period 2),

$$K_{T_{ps},2}^{\text{II}} (dT_{ps})_{\text{II}} + K_{T_2}^{\text{II}} (dT)_{\text{II}} = K_{c_{m,2}}^{\text{II}} \Delta t \quad (\text{A-3.71})$$

The coefficients of the above equations are,

For Time Period 1:

$$K_{T_{ps},1}^{\text{II}} = 1 \quad (\text{A-3.72})$$

$$K_{T_1}^{\text{II}} = - \left[ \frac{\delta h_T \Gamma_p}{k_p (6\Gamma_p - \delta) + h_T \delta \Gamma_p} \right] \quad (\text{A-3.73})$$

$$K_{c_{m,1}}^{\text{II}} = \left\{ \frac{12\alpha_p [k_p (T_p - T_a) + \Gamma_p h_T (T - T_{ps})]}{\delta [k_p (6\Gamma_p - \delta) + \Gamma_p h_T \delta]} \right\} \quad (\text{A-3.74})$$

For Time Period 2:

$$K_{T_{ps},2}^{\text{II}} = 1 \quad (\text{A-3.75})$$

$$K_{T_2}^{\text{II}} = - \left( \frac{\Gamma_p h_T}{4k_p + \Gamma_p h_T} \right) \quad (\text{A-3.76})$$

$$K_{c_{m,2}}^{\text{II}} = \left[ \frac{12\alpha_p h_T (T - T_{ps})}{(4\Gamma_p k_p + \Gamma_p^2 h_T)} \right] \quad (\text{A-3.77})$$

APPENDIX 4

Determination of Eigenvalues for the Governing Equations

The purpose of this appendix is to indicate the algebraic steps to obtain the eigenvalues given by Eqs. (3.6.4). The governing equations are transformed into a matrix form given by Eq. (3.6.1).

In order to find the eigenvalues of the system we have to set  $|\tilde{M} - \lambda \tilde{I}_m| = 0$ , where  $\tilde{M}$  is given by Eq. (3.6.3) and  $\tilde{I}_m$  is the identity matrix.

Now we have the following matrix,

$$\begin{bmatrix} -(u_3 + \lambda) & 0 & \frac{-S}{\beta} & 0 & \frac{-gP}{\beta} \\ -\frac{P}{\beta} & -(u_3 + \lambda) & 0 & 0 & 0 \\ -\frac{S^2 P}{\beta} & 0 & -(u_3 + \lambda) & \frac{-(1-\beta)P^2}{\beta \beta T} & 0 \\ 0 & 0 & 0 & -(u_4 + \lambda) & \frac{C^2}{(1-\beta)} \\ 0 & 0 & 0 & (1-\beta) & -(u_4 + \lambda) \end{bmatrix} \quad (A-4.1)$$

We then perform the following elementary row and column operation to arrive to a better form to operate.

Interchange Column 1 with 2 and expand we get

$$\begin{array}{c}
 \\
 \\
 -(u_g + \lambda) \\
 \\
 \\
 \end{array}
 \left[ \begin{array}{cccc}
 -(u_g + \lambda) & \frac{-g}{p} & 0 & -\frac{gP}{\phi p} \\
 \frac{-C_g^i P}{g} & -(u_g + \lambda) & -\frac{(1-\phi)P^2}{\rho \phi RT} & 0 \\
 0 & 0 & -(u_p + \lambda) & \frac{c^2}{(1-\phi)} \\
 0 & 0 & (1-\phi) & -(u_p + \lambda)
 \end{array} \right]
 \quad (A-4.2)$$

Expand Column 1 we have

$$\begin{array}{c}
 \\
 (u_g + \lambda)^2 \\
 \\
 \\
 \\
 \end{array}
 \left[ \begin{array}{ccc}
 -(u_g + \lambda) & -\frac{(1-\phi)P^2}{\rho \phi RT} & 0 \\
 0 & -(u_p + \lambda) & \frac{c^2}{(1-\phi)} \\
 0 & 1-\phi & -(u_p + \lambda)
 \end{array} \right]
 \quad (A-4.3.1)$$

$$\begin{array}{c}
 \\
 \\
 -(u_g + \lambda) \frac{C_g^i P}{g} \\
 \\
 \\
 \end{array}
 \left[ \begin{array}{ccc}
 \frac{-g}{p} & 0 & -\frac{gP}{\phi p} \\
 0 & -(u_p + \lambda) & \frac{c^2}{(1-\phi)} \\
 0 & (1-\phi) & -(u_p + \lambda)
 \end{array} \right]
 \quad (A-4.3.2)$$

from (A-4.3.1) we have

$$-(u_g + \lambda)^2 \begin{bmatrix} -(u_p + \lambda) & \frac{c^2}{(1-\beta)} \\ (1-\beta) & -(u_p + \lambda) \end{bmatrix} \quad (\text{A-4.4.1})$$

from (A-4.3.2) we have

$$+(u_g + \lambda)c_g^2 \begin{bmatrix} -(u_p + \lambda) & \frac{c^2}{(1-\beta)} \\ (1-\beta) & -(u_p + \lambda) \end{bmatrix} \quad (\text{A-4.4.2})$$

Expand Eq. (A-4.4.1) and (A-4.4.2) we get

$$-(u_g + \lambda)^2 [(u_p + \lambda)^2 - c^2] + (u_g + \lambda) c_g^2 [(u_p + \lambda)^2 - c^2] = 0 \quad (\text{A-4.5})$$

$$[-(u_g + \lambda)^2 + (u_g + \lambda) c_g^2] [(u_p + \lambda)^2 - c^2] = 0 \quad (\text{A-4.6})$$

The roots of Eq. (A-4.6) are

$$\lambda_1 = -(u_g + c_g) \quad (\text{A-4.7})$$

$$\lambda_2 = -(u_g - c_g) \quad (\text{A-4.8})$$

$$\lambda_3 = -u_g \quad (\text{A-4.9})$$

$$\lambda_4 = -(u_p + c) \quad (\text{A-4.10})$$

$$\lambda_5 = -(u_p - c) \quad (\text{A-4.11})$$

from the particle heat equation we obtain

$$\lambda_6 = -u_p \quad (\text{A-4.12})$$

where

$$C_g = \left\{ \frac{g[PpC_v(JRT + P_b) + P^2R]}{P^2RTJc_v} \right\}^{1/2} \quad (A-4.13)$$

c, speed of sound in particle phase, are given by Eqs. (A-6.1) or (A-6.2).

## APPENDIX 5

### Finite-Difference Equations for the Gas Mass Equation

This appendix is intended to show a typical way of expressing the governing equation into its finite-difference form. The gas mass equation was chosen here for simplicity. First the divergence form of the governing equations were obtained from Eq. (3.4.1). For clarity we rewrite it in the following

$$\frac{\partial(\rho\phi)}{\partial t} + \frac{\partial(\rho\phi u_g)}{\partial x} = A_s \rho_p \Gamma_b \quad (\text{A-5.1})$$

Expressing the above equation according to Eqs. (4.2.4) and (4.2.5), we have for the first step predictor and corrector as follows,

Predictor:

$$\begin{aligned} (\rho\phi)_i^{j+1^A} = & \frac{1}{2} [(\rho\phi)_{i+1}^j + (\rho\phi)_{i-1}^j] - \frac{\Delta t}{2\Delta x} [(\rho\phi u_g)_{i+1}^j - (\rho\phi u_g)_{i-1}^j] \\ & + \Delta t (A_s \rho_p \Gamma_b)_i \end{aligned} \quad (\text{A-5.2})$$

and Corrector:

$$\begin{aligned} (\rho\phi)_i^{j+1} = & \frac{1}{2} [(\rho\phi)_{i+1}^j + (\rho\phi)_{i-1}^j] - \frac{\Delta t}{2\Delta x} \{ (1-\theta) [(\rho\phi u_g)_{i+1}^j - (\rho\phi u_g)_{i-1}^j] \\ & + \theta [(\rho\phi u_g)_{i+1}^{j+1^A} - (\rho\phi u_g)_{i-1}^{j+1^A}] \} + \Delta t [(1-\theta)(A_s \rho_p \Gamma_b)_i \\ & + \theta (A_s \rho_p \Gamma_b)_i^{j+1^A}] \end{aligned} \quad (\text{A-5.3})$$

In the corrector calculation, the spatial derivatives and the inhomogeneous terms are averaged between the  $j^{\text{th}}$  and  $j+1$  level terms using a weight factor,  $\theta$ , where  $0 \leq \theta \leq 1$ . The superscript  $\Delta$ , indicates a predicted quantity.

Similarly the second step predictor and corrector are expressed according to Eqs. (4.2.8) and (4.2.9), resulting in two analogous equations.

Predictor:

$$(\rho\phi)_i^{j+2^*} = (\rho\phi)_i^j - \frac{\Delta t}{\Delta x} [(\rho\phi u_g)_{i+1}^{j+1} - (\rho\phi u_g)_{i-1}^{j+1}] + 2\Delta t (A_s \rho_p \Gamma_b)_i^{j+1} \quad (A-5.4)$$

Corrector:

$$(\rho\phi)_i^{j+2} = (\rho\phi)_i^j - \frac{\Delta t}{2\Delta x} \left\{ (1-\theta) [(\rho\phi u_g)_{i+1}^j - (\rho\phi u_g)_{i-1}^j] + \theta [(\rho\phi u_g)_{i+1}^{j+2^*} - (\rho\phi u_g)_{i-1}^{j+2^*}] + [(\rho\phi u_g)_{i+1}^{j+1} - (\rho\phi u_g)_{i-1}^{j+1}] \right\} + \Delta t [(1-\theta)(A_s \rho_p \Gamma_b)_i^j + \theta (A_s \rho_p \Gamma_b)_i^{j+2^*} + (A_s \rho_p \Gamma_b)_i^j] \quad (A-5.5)$$

In the corrector calculation three levels,  $j^{\text{th}}$ ,  $j+1$  and  $j+2$  are used together to average the spatial derivatives and inhomogeneous terms in Eq. (A-5.1)

Eqs. (A-5.2) - (A-5.5) are the typical sequence for expressing the conservation equations using our numerical scheme. Other conservation equations are coded in a similar manner.

APPENDIX 6

The Relationships of Intergranular Stress and the  
Speed of Sound in Granular Beds

This appendix is mainly to derive a  $\tau_p$  (the intragranular stress),  
expression in terms of  $c$  (the speed of sound).

We proposed the speed of sound in the solid propellant as a  
function of  $\phi$ , porosity and is described by, (Fig. 26)

$$c = \begin{cases} c_{ref} \frac{\phi_c}{\phi} & \text{if } \phi \leq \phi_c & \text{(A-6.1)} \\ c_{ref} e^{-\kappa(\phi - \phi_c)} & \text{if } \phi > \phi_c & \text{(A-6.2)} \end{cases}$$

$c_{ref}$  is obtained from Super's (10,98) work and  $\kappa$  is a dimensionless  
exponent for the decay of  $c$  after  $\phi_c$  is reached.

The velocity of propagation is given in Reference (59) as,

$$c^2 = \frac{g}{\rho_p} \frac{d}{d\phi} [(1-\phi)\tau_p] \quad \text{(A-6.3)}$$

Now integrate Eq. (A-6.3) for the packed bed region,

$$g \int_{\phi}^{\phi_c} [(1-\phi)(\tau_p)] d\phi = \rho_p c_{ref}^2 \int_{\phi}^{\phi_c} \left(\frac{\phi_c}{\phi}\right)^2 d\phi \quad \text{(A-6.4)}$$

for  $\phi \leq \phi_c$ .

After integration and rearranging of term we get

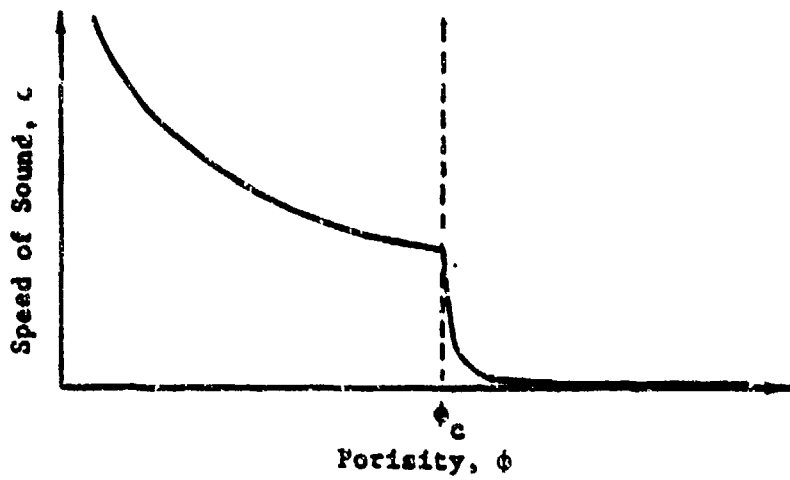


Figure 26 The Dependence of Speed of Sound in the Solid Propellant Aggregate

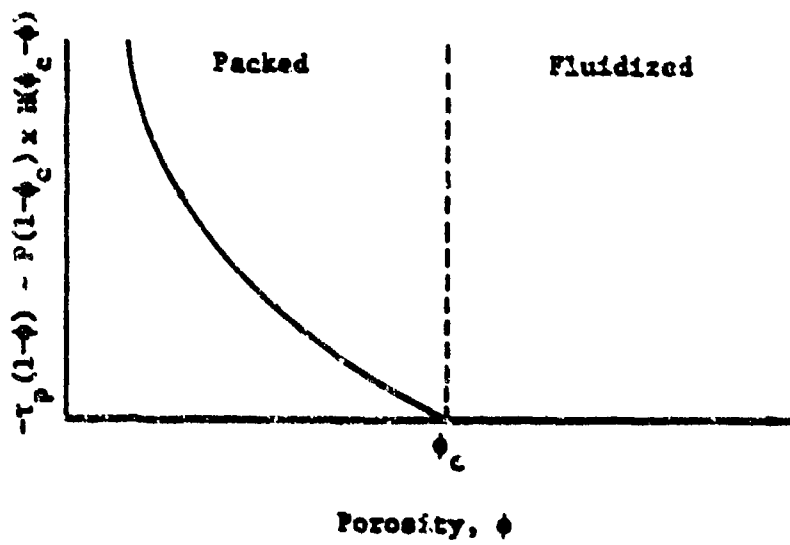


Figure 27 Dependence of Particulate Stress Tensor upon Porosity of the Mixture

$$-g[(1-\phi_c)(P) + (1-\phi)\tau_p] = \rho_p c^2 \phi^2 \left( \frac{\phi_c - \phi}{\phi \phi_c} \right) \quad (\text{A-6.5})$$

For packed beds  $\tau_p$  is expressed as follows,

$$-\tau_p = \frac{\rho_p c^2}{(1-\phi)g} \frac{\phi}{\phi_c} (\phi_c - \phi) - \frac{\phi}{1-\phi} P \quad (\text{A-6.6})$$

for  $\phi \leq \phi_c$ .

In the case of dispersed particles, we again integrate Eq. (A-6.3) from  $\phi$  to 1 we have,

$$g[(1-\phi)(\tau_p)]_{\phi}^{\phi=1} = \rho_p c^2 \int_{\phi}^1 e^{-2K(\phi^* - \phi_c)} d\phi^* \quad (\text{A-6.7})$$

Now define  $\tau = \phi^* - \phi_c$  and substitute in Eq. (A-6.7)

$$g(1-\phi)\tau_p = \rho_p c^2 \left( \frac{1}{2K} \right) [e^{-2K\tau}]_{\phi-\phi_c}^{1-\phi_c} \quad (\text{A-6.8})$$

After some algebraic manipulations we get the  $\tau_p$  expression for a fluidized bed,

$$\tau_p = \frac{-\rho_p c^2}{2(1-\phi)Kg} [1 - e^{-2K(1-\phi)}] \quad (\text{A-6.9})$$

If  $\phi$  is approaching 1, the bracketed term of Eq. (A-6.9) is approaching zero, as a result we have

$$\tau_p = 0 \quad (\text{A-6.10})$$

When  $\phi$  is larger than  $\phi_c$  by a small amount,  $c^2$  goes to zero very rapidly since it's an exponential decay function. Therefore,  $\tau_p$  is almost zero.

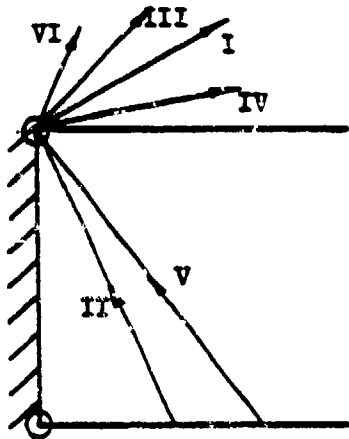
As a result it is a good assumption to have the following equation,

$$(1-\phi)\tau_p = 0 \quad \text{for } \phi > \phi_c \quad (\text{A-6.11})$$

Where Fig. 27 shows the relationships between the intergranular stress and porosity, in granular beds, and H is the Heaviside function.

APPENDIX 7

Characteristics Considered for Various Cases at the Left Boundary.



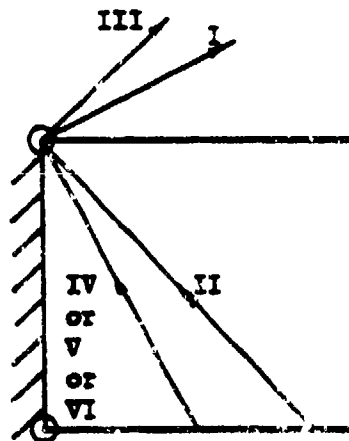
LBC1 :

$u_g(x_L, t)$  is positive (+);

$u_p(x_L, t)$  is positive (+);

Non-fluidized and no burning at left boundary;

Characteristics considered : II, V



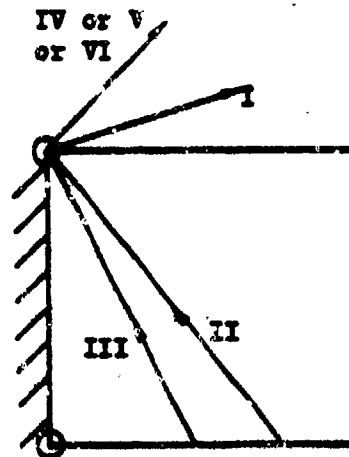
LBC2 :

$u_g(x_L, t)$  is positive (+);

$u_p(x_L, t)$  is negative (-);

Fluidized at left boundary;

Characteristics considered : II, IV or V or VI



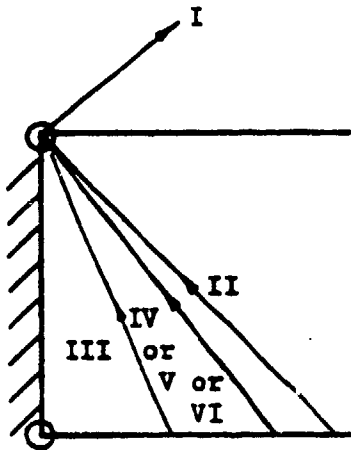
LBC3 :

$u_g(x_L, t)$  is negative (-);

$u_p(x_L, t)$  is positive (+);

Fluidized at left boundary;

Characteristics considered : II, I



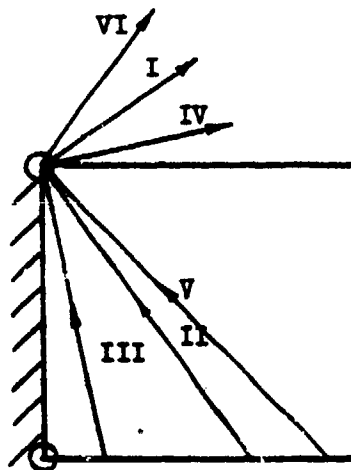
LBC4 :

$u_g(x_L, t)$  is negative (-);

$u_p(x_L, t)$  is negative (-);

Fluidized at left boundary;

Characteristics considered :  
II, III, VI or V or VI



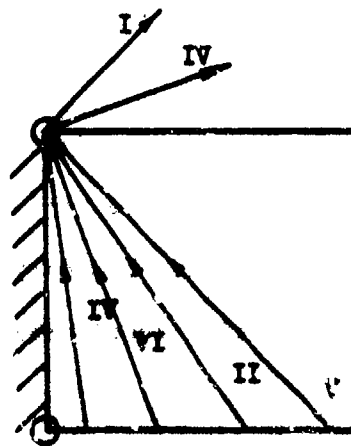
LBC5 :

$u_g(x_L, t)$  is negative (-);

$u_p(x_L, t)$  is positive (+);

Non-fluidized at left boundary;

Characteristics considered :  
II, III, V



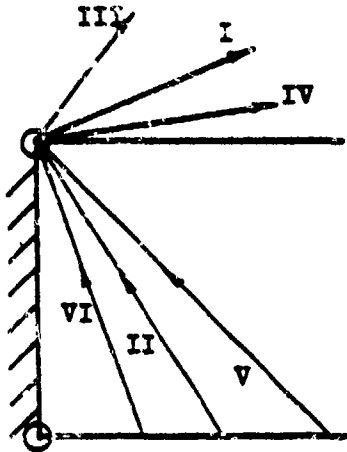
LBC6 :

$u_g(x_L, t)$  is negative (-);

$u_p(x_L, t)$  is negative (-);

Non-fluidized at left boundary;

Characteristics considered :  
II, III, V, VI



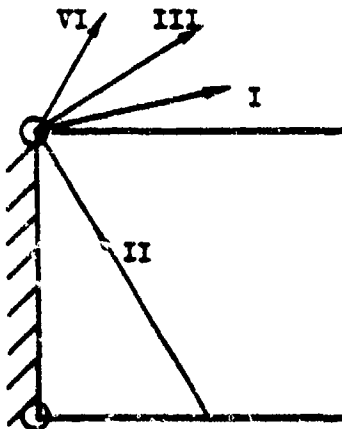
LBC7 :

$u_g(x_L, t)$  is positive (+);

$u_p(x_L, t)$  is negative (-);

Non-fluidized at left boundary;

Characteristics considered : II, V, VI



LBC5 :

$u_g(x_L, t)$  is positive (+);

$u_p(x_L, t)$  is positive (+);

Fluidized at left boundary;

Characteristics considered : II

This appendix is to show the various cases we considered for the left boundary conditions by varying the flow directions of  $u_g(x_L, t)$  and  $u_p(x_L, t)$  and the fluidization conditions at the left boundary. These eight sets of left boundary conditions have been implemented in the computer program individually.

NOMENCLATURE

<u>Letter Symbols</u>	<u>Description</u>
a	Pre-exponential factor for burning rate law
A	Cross-sectional area of the cylindrical combustion chamber
$A_g$	Specific surface area of the granular pro-pellants, the surface exposed to fluid per unit volume
A <sub>1,2,3,4,5,6</sub>	The intersections of the I, II, III, IV, V, VI characteristics with the x-axis near the left boundary of the granular bed
A' <sub>1,2,3,4,5,6</sub>	The intersections of the I, II, III, IV, V, VI characteristics with the x-axis near the right boundary of the granular bed
b	Co-volume of the Clausius equation of state
B	Boundary point at the left end of the granular bed
B'	Boundary point at the right end of the granular bed
c	Speed of sound in particle phase
$C_d$	Detarant concentration
$C_L$	Combustion chamber length
$C_v$	Specific heat at constant volume
$C_p$	Specific heat at constant pressure
$\frac{dx}{dt}$	Slope of the characteristic equations
$D_c$	The total drag force between the gas and particle phases in the entrance region
$D_p$	Drag force due to porosity gradient
$D_t$	The total drag force between the gas and particle phases. $D_t = D_v + D_p$
$D_v$	Drag force acting on gases by the particles per unit wetted area of particles
$\left(\frac{D}{Dt}\right)_p$	Lagrangian time derivative when observer follows the motion of a particle. $\frac{\partial}{\partial t} + u_p \frac{\partial}{\partial x}$

Letter SymbolsDescription

$E$	Total stored energy (internal plus kinetic energy) per unit mass
$g$	Gravitational constant
$h_c$	The average convection heat-transfer coefficient over pellets
$h_{chem}$	Enthalpy of the propellant gas at flame temperature
$h_{ign}$	Enthalpy of the igniter gas
$h_{rad}$	The average radiation heat transfer coefficient over pellets
$h_t$	The total heat transfer coefficient, the unit-surface conductance
$\dot{h}_t$	The rate of change of unit-surface conductance in following a given particle
$H$	Heaviside function
$\vec{I}$	Inhomogeneous vector for the governing equations
$\vec{I}_m$	Identity matrix
$I_{1,2,3,4,5,6}$	Components of the inhomogeneous vector $\vec{I}$
$J$	Heat to work conversion factor
$k$	Thermal conductivity of gases
$k_p$	Thermal conductivity of particles
$K$	Coefficient of characteristic equations
$K_e$	erosive burning constant
$\dot{m}_{ign}$	Mass flow rate of igniter
$\dot{m}_{in}$	Mass flow rate of gas into the granular bed
$\vec{M}$	Variable matrix defined in Eq. (3.6.3)
$n$	Pressure exponent for the burning rate law
$n$	Number density of spherical pellets in the granular bed

Letter SymbolsDescription

P	Pressure
Pr	Prandtl number
$\phi_{wg}$	Wetted perimeter between the chamber wall and gas phase
$\phi_{wp}$	Wetted perimeter between the chamber wall and particle phase
q	Rate of conduction heat transfer per unit area
$\dot{Q}_v$	Rate of heat loss to the chamber wall per unit spatial volume of gas-particle system
r	Radial distance from the center of a spherical particle
$r_b$	Burning rate of the solid propellant
$r_p$	Radius of pellets
R	Gas constant
$Re_p$	Reynolds number, $\frac{2r_p \rho \phi  u_k - u_p }{\mu}$
t	Time
T	Temperature
$T_{abl}$	Ablation temperature of the solid propellant
$T_f$	Adiabatic flame temperature of pellets
$T_{hg}$	Temperature of the hot igniter gas
$T_{ign}$	Ignition temperature of the solid propellant
$T_{ps}$	Particle surface temperature
$T_0$	Initial temperature of pellets
$T_{1,2,3,4}$	Coefficients in the fourth-order Runge-Kutta calculations
u	Velocity with respect to laboratory coordinates
$u_{ign}$	Igniter gas velocity

Letter SymbolsDescription

$W/$ 1,2,3,4,5	Adjoint eigenvectors of M
$W_{ij}$	$j^{\text{th}}$ component of $W/i$ vector
$x$	Distance from the beginning of the granular propellant bed
$x_L$	Left boundary point
$x_R$	Right boundary point

Greek Symbols

$\alpha_p$	Thermal diffusivity of pellets
$\beta$	Erosive burning exponent in the Lenoir-Robillard burning-rate law
$\gamma$	Specific heat ratio
$\delta$	Thermal wave penetration depth in a spherical particle, measured from the particle surface
$\Delta$	Difference
$\epsilon_p$	Emissivity of particle
$\mu$	Dynamic viscosity of the gas phase
$\rho$	Gas density
$\rho_p$	Density of pellets
$\lambda$ 1,2,3,4,5,6	Eigenvalues of the governing equations
$\tau_p$	Normal stress transmitted in solid propellants
$\tau_{wg}$	Shear stress between the chamber wall and gas phase
$\tau_{wp}$	Shear stress between the chamber wall and particle phase
$\tau_{xx}$	Viscous normal stress in gas phase
$\phi$	Fractional porosity
$\phi_c$	Critical porosity

Greek SymbolsDescription

$\theta$  Crank-Nicolson parameter

$\sigma$  Stefan-Boltzmann constant

Subscripts

$A_{1,2,3,4,5,6}$

Quantities evaluated at intersections  $A_1$ ,  $A_2$ ,  $A_3$ ,  $A_4$ ,  $A_5$  and  $A_6$  respectively

$A'_{1,3,4,6}$

Quantities evaluated at intersections  $A'_1$ ,  $A'_3$ ,  $A'_4$  and  $A'_6$  respectively

B Quantities evaluated at point B at the left boundary

c Quantities evaluated at the entrance region

g Gas phase

i Index for discrete points in the spatial direction,  $x_i = i \Delta x$

ign Igniter

$M_{2,3,5}$

Quantities evaluated at the mid-point of  $j^{\text{th}}$  and  $j + 1^{\text{th}}$  level for characteristics II, III and V

p Particle phase

P Quantities related to P (Pressure)

tm Quantities related to tm (Time)

T Quantities related to T (gas temperature)

$T_{ps}$  Quantities related to  $T_{ps}$  (particle surface temp.)

$u_g$  Quantities related to  $u_g$  (gas velocity)

$u_p$  Quantities related to  $u_p$  (particle velocity)

$\phi$  Quantities related to  $\phi$  (porosity)

$x_L$  Quantities evaluated at the left boundary

$x_R$  Quantities evaluated at the right boundary

I Along right-running characteristic line in the gas phase

SubscriptsDescription

II	Along left-running characteristic line in the gas phase
III	Along gaseous-path characteristic line in the gas phase
IV	Along right-running characteristic line in the particle phase
V	Along left-running characteristic line in the particle phase
VI	Along particle-path characteristic line in the particle phase
0	Initial state
00	0% deterrent concentration
30	30% deterrent concentration

Superscripts

j	Index for discrete time increments, $t^j = j \Delta t$
T	Transpose of a matrix or vector
$\Delta$	Predicted value in numerical scheme
'	Rate of change of certain quantities
'	Right boundary parameters
I	Quantities related to characteristic I
II	Quantities related to characteristic II
III	Quantities related to characteristic III
IV	Quantities related to characteristic IV
V	Quantities related to characteristic V
VI	Quantities related to characteristic VI

DISTRIBUTION LIST

<u>No. of</u> <u>Copies</u>	<u>Organization</u>	<u>No. of</u> <u>Copies</u>	<u>Organization</u>
12	Commander Defense Documentation Center ATTN: DCC-TCA Cameron Station Alexandria, VA 22314	1	Commander US Army Missile Research and Development Command ATTN: DEDMI-R Redstone Arsenal, AL 35809
1	Director Defense Advanced Research Projects Agency ATTN: C. R. Lehner 1400 Wilson Boulevard Arlington, VA 22209	1	Commander US Army Tank Automotive Development Command ATTN: DEDTA-TWL Warren, MI 48090
2	Director Institute for Defense Analyses ATTN: Dr. H. Wolfhard Mr. R. T. Oliver 400 Army-Navy Drive Arlington, VA 22202	2	Commander US Army Mobility Equipment Research & Development Command ATTN: Tech Doc Ctr, Bldg 315 DRSME-RZT Ft. Belvoir, VA 22060
1	Commander US Army Material Development and Readiness Command ATTN: DRCDMA-ST 5001 Eisenhower Avenue Alexandria, VA 22333	1	Commander US Army Armament Material Readiness Command Rock Island, IL 61202
1	Commander US Army Aviation Systems Command ATTN: DREAV-E 12th and Spruce Streets St. Louis, MO 63166	8	Commander US Army Armament Research and Development Command ATTN: DEDAR-LC, Dr. H. Fair DEDAR-LCE, Mr. C. Lenchitz DEDAR-LCE, Dr. R. P. Walker DEDAR-LCE, Dr. J. Horakewitz F. Fitzsimmons P. A. Sarao J. Deann J. C. Pearson Dover, NJ 07801
1	Director US Army Air Mobility Research and Development Laboratory Ames Research Center Moffett Field, CA 94035	1	Commander US Army White Sands Missile Range ATTN: SIEWS-VT WVHM, NM 88002
1	Commander US Army Electronics Command ATTN: DREEL-ND Ft. Monmouth, NJ 07703		

DISTRIBUTION LIST

<u>No. of Copies</u>	<u>Organization</u>	<u>No. of Copies</u>	<u>Organization</u>
1	Commander US Army Watervliet Arsenal ATTN: R. Thierry/Code SAKNV-MD Watervliet, NY 12189	2	Commander US Naval Surface Weapons Ctr ATTN: S. J. Jacobs/Code 240 Code 730 Silver Spring, MD 20910
1	Commander US Army Harry Diamond Labs ATTN: DEXDO-TI 2800 Powder Mill Road Adelphi, MD 20783	1	Commander US Naval Surface Weapons Ctr ATTN: Tech Lib Dahlgren, VA 22338
1	Commander US Army Materials and Mechanics Research Center ATTN: DEXMR-ATL Watertown, MA 02172	1	Commander US Naval Underwater Systems Ctr Energy Conversion Department ATTN: R. S. Lazar/Code 5B331 Newport, RI 02840
1	Commander US Army Matick Research and Development Command ATTN: DEXRE, Dr. D. Sieling Matick, MA 01762	2	Commander US Naval Weapons Center ATTN: Dr. R. Darr Mr. C. Thelen China Lake, CA 93555
1	Director US Army TRADOC Systems Analysis Activity ATTN: ATAA-SA WARR, NH 88002	1	Commander US Naval Research Laboratory ATTN: Code 6180 Washington, DC 20375
1	Commander US Army Research Office ATTN: Tech Lib P.O. Box 12211 Research Triangle Park, NC 27706	3	Superintendent US Naval Postgraduate School ATTN: Tech Lib Dr. David Metzger Dr. Allen Fuhs Monterey, CA 93940
1	Chief of Naval Research ATTN: Code 473 800 N. Quincy Street Arlington, VA 22217	2	Commander US Naval Ordnance Station ATTN: Dr. A. Roberts Tech Lib Indian Head, MD 20640
1	Commander US Naval Sea Systems Command ATTN: J. W. Murrin (NAVSEA-0331) National Center, Bldg 2, Rm 6E06 Washington, DC 20360	2	AFOSR ATTN: J. R. Masi Dr. B. T. Wolfson Bolling AFB, DC 20332

DISTRIBUTION LIST

<u>No. of Copies</u>	<u>Organization</u>	<u>No. of Copies</u>	<u>Organization</u>
2	AFRPL (DYSC) ATTN: Dr. D. George Mr. J.H. Levine Edwards AFB, CA 93523	1	EMKI Corporation ATTN: M. I. Madison 9015 Fulbright Avenue Chatsworth, CA 91311
1	Lockheed Palo Alto Rech Labs ATTN: Tech Info Ctr 3521 Hanover Street Palo Alto, CA 94304	1	Foster Miller Assoc., Inc. ATTN: A. J. Erickson 135 Second Avenue Waltham, MA 02154
1	National Science Foundation ATTN: Dr. Morris Ojalvo Washington, DC 20550	1	General Electric Company Armament Department ATTN: M. J. Bulman Lakeside Avenue Burlington, VT 05402
1	Aerojet Solid Propulsion Co. ATTN: Dr. P. Micheli Sacramento, CA 95813	1	General Electric Company Flight Propulsion Division ATTN: Tech Lib Cincinnati, OH 45215
1	ARO Incorporated ATTN: Mr. N. Dougherty Arnold AFB, TX 37389	2	Hercules Incorporated Allegheny Ballistic Lab ATTN: Dr. R. Miller Tech Lib Cumberland, MD 21501
1	Atlantic Research Corporation ATTN: Dr. M.K. King 5390 Cherokee Avenue Alexandria, VA 22314	2	Hercules Incorporated Bacchus Works ATTN: Dr. M. Beckstead Dr. R. Simmons Magna, UT 84044
1	AVCO Corporation AVCO Everett Research Lab Div ATTN: D. Stikler 2385 Revere Beach Parkway Everett, MA 02149	2	IITRI ATTN: Dr. M. J. Klein H. Nepodensky 10 West 35th Street Chicago, IL 60615
1	Energy Incorporated ATTN: Dr. E. D. Hughes Idaho Falls, ID 83401	1	Olin Corporation Badger Army Ammunition Plant ATTN: J. Ramarace Baraboo, WI 53913

DISTRIBUTION LIST

<u>No. of Copies</u>	<u>Organization</u>	<u>No. of Copies</u>	<u>Organization</u>
2	Olin Corporation New Haven Plant ATTN: R. L. Cook D. W. Riefler 275 Winchester Avenue New Haven, CT 06504	1	Thiokol Corporation Elkton Division ATTN: E. Sutton Elkton, MD 21921
1	Paul Gough Associates, Inc. ATTN: Dr. P. S. Gough P.O. Box 1614 Portsmouth, NH 03801	3	Thiokol Corporation Huntsville Division ATTN: Dr. D. Flanigan Dr. R. Glick Tech Lib Huntsville, AL 35807
1	Pulsepower Systems, Inc. ATTN: L. C. Elmore 815 American Street San Carlos, CA 94070	2	Thiokol Corporation Wasatch Division ATTN: Dr. John Peterson Tech Lib P.O. Box 524 Brigham City, UT 84302
1	Science Applications, Inc. ATTN: Dr. R. B. Edelman 23146 Cumorah Crest Woodland Hills, CA 91364	1	TRW Systems Group ATTN: Dr. H. Korman One Space Park Redondo Beach, CA 90278
2	Rockwell International Corp. Rockaldyne Division ATTN: Dr. C. Obart Dr. J. E. Flanagan 6633 Canoga Avenue Canoga Park, CA 91304	2	United Technology Center ATTN: Dr. R. Brown Tech Lib P.O. Box 358 Sunnyvale, CA 94088
2	Rockwell International Corp. Rocketdyne Division ATTN: Mr. W. Haynes Tech Lib McGregor, TX 76657	1	Universal Propulsion Co. ATTN: H. J. McSpadden P.O. Box 546 Riverside, CA 92502
1	Shock Hydrodynamics, Inc. ATTN: Dr. W. E. Anderson 4710-16 Vinaland Avenue North Hollywood, CA 91602	1	Battelle Memorial Institute ATTN: Tech Lib 505 King Avenue Columbus, OH 43201
		1	Brigham Young University Dept of Chemical Engineering ATTN: Prof. R. Coates Provo, UT 84601

DISTRIBUTION LIST

<u>No. of Copies</u>	<u>Organization</u>	<u>No. of Copies</u>	<u>Organization</u>
1	California Institute of Tech. Jet Propulsion Laboratory ATTN: Prof. F. E. C. Culick Pasadena, CA 91103	1	Pennsylvania State University Dept of Mechanical Engrg ATTN: Prof. K. Kuo University Park, PA 16801
1	California State University ATTN: F. H. Reardon Sacramento, CA 95813	3	Forrestal Campus Library Princeton University ATTN: Prof. M. Summerfield Dr. L. Caveny Tech Lib P.O. Box 710 Princeton, NJ 08540
1	Case Western Reserve Univ. Division of Aerospace Sciences ATTN: Prof. J. Tien Cleveland, OH 44135	2	Purdue University School of Mechanical Engrg ATTN: Prof. J. Osborn Prof. S. N. B. Murthy TSPC Chaffee Hall West Lafayette, IN 47906
3	Georgia Institute of Technology School of Aerospace Engineering ATTN: Prof. B. T. Zimm Prof. E. Price Prof. W. C. Strahle Atlanta, GA 30332	1	Rutgers State University Dept of Mechanical and Aero- space Engineering ATTN: Prof. S. Temkin University Heights Campus New Brunswick, NJ 08903
1	Institute of Gas Technology ATTN: Dr. D. Gidaspo 3424 S. State Street Chicago, IL 60616	1	Southwest Research Institute Fire Research Section ATTN: W. H. McLain P.O. Drawer 28510 San Antonio, TX 78228
1	Johns Hopkins University Applied Physics Laboratory Chemical Propulsion Infor- mation Agency ATTN: Mr. T. Christian Johns Hopkins Road Laurel, MD 20810	1	Stanford Research Institute Propulsion Sciences Division ATTN: Tech Lib 333 Ravenswood Avenue Menlo Park, CA 94024
1	Massachusetts Institute of Technology Dept of Mechanical Engineering ATTN: Prof. T. Teoag Cambridge, MA 02139	1	Stevens Institute of Technology Davidson Laboratory ATTN: Prof. R. McAlevy, III Boboken, NJ 07030
1	Pennsylvania State University Applied Research Lab ATTN: Dr. G. M. Faeth P.O. Box 30 State College, PA 16801		

DISTRIBUTION LIST

<u>No. of</u> <u>Copies</u>	<u>Organization</u>	<u>No. of</u> <u>Copies</u>	<u>Organization</u>
1	University of California, San Diego AMES Department ATTN: Prof. F. Williams P.O. Box 109 La Jolla, CA 92037		<u>Aberdeen Proving Ground</u>  Marine Corps LnO Dir, USAMSAA
1	University of Denver Denver Research Institute ATTN: Tech Lib P.O. Box 10127 Denver, CO 80210		
1	University of Illinois Dept of Aeronautical Engrg ATTN: Prof. H. Krier Transportation Bldg, Rm 105 Urbana, IL 61801		
1	University of Minnesota Dept of Mechanical Engrg ATTN: Prof. E. Fletcher Minneapolis, MN 55455		
2	University of Utah Dept of Chemical Engrg ATTN: Prof. A. Baer Prof A. Flandro Salt Lake City, UT 84112		
1	Washington State University Dept of Mechanical Engrg ATTN: Prof. C. T. Crowe Pullman, WA 99163		